# Growth and characterization of *M*-plane GaN and (In,Ga)N/GaN multiple quantum wells

## DISSERTATION

zur Erlangung des akademischen Grades
doctor rerum naturalium
(Dr. rer. nat.)
im Fach Physik

eingereicht an der
Mathematisch-Naturwissenschaftlichen Fakultät I
Humboldt-Universität zu Berlin

von
Herrn M.Eng. Yue-Jun Sun
geboren am 27.07.1973 in LeShan, VR. China

Präsident der Humboldt-Universität zu Berlin:
Prof. Dr. Jürgen Mlynek

Dekan der Mathematisch-Naturwissenschaftlichen Fakultät I:
Prof. Dr. Michael Linscheid

Gutachter:

1. Prof. Dr. Klaus H. Ploog
2. Prof. Dr. W. Ted Masselink
3. Prof. Dr. Roberto Fornari

eingereicht am: 18. Dezember 2003
Tag der mündlichen Prüfung: 24. Mai 2004

# Abstract

In this thesis, we investigate the synthesis of wurtzite *M*-plane (In,Ga)N($1\bar{1}00$) heterostructures on $\gamma$-LiAlO$_2$(100) by plasma-assisted molecular beam epitaxy (MBE). We examine the impact of growth conditions on the structural, morphological, and optical doping properties of *M*-plane GaN. Furthermore, we fabricate *M*-plane (In,Ga)N/GaN multiple quantum wells and investigate their structural and optical properties. Finally, the incorporation of Mg in *M*-plane GaN is studied to achieve p-type conductivity.

We start by giving an introduction concerning strain and electrostatic polarization fields. The motivation of growth along the [$1\bar{1}00$] direction, instead of along the conventional [0001] direction is presented. The GaN($1\bar{1}00$) plane is nonpolar since it is composed of equal numbers of three-fold coordinated Ga and N atoms. Furthermore, GaN is not piezoelectrically active along the [$1\bar{1}00$] direction. The resulting absence of electrostatic fields in this direction constitutes a distinct advantage for fabricating high-efficiency light-emitting diodes(LEDs). Corresponding [0001]-oriented structures grown on conventional substrates such as Al$_2$O$_3$(0001) and SiC(0001), suffer from a degradation of luminescence efficiency by the presence of both spontaneous and piezoelectric polarization along the growth direction.

The properties of the LiAlO$_2$ substrate with respect to MBE growth are discussed next. The thermal stability of LiAlO$_2$ is demonstrated to be suitable for MBE-growth of heterostructures. The polarity of LiAlO$_2$ is found to have a crucial influence on the phase-purity of the GaN films. The synthesis of pure *M*-plane GaN is preferentially achieved on one face of the substrate.

The impact of nucleation conditions on the structural and morphological properties of *M*-plane GaN films is systematically investigated. Furthermore, a comprehensive study of Ga adsorption and desorption on the *M*-plane is presented. Optimum growth conditions are established, and high quality *M*-plane GaN can be obtained reproducibly. Concerning the microstructure of our *M*-plane GaN layers, stacking faults are found by transmission electron microscopy (TEM) to be the dominant defects, while perfect threading dislocations, which are the dominant defects ($10^8-10^{10}$ cm$^{-2}$) in *C*-plane GaN, are not observed by TEM. The correlation between the stacking faults and the optical properties of the films is explored. A strong transition from excitons bound to stacking faults is observed by low temperature photoluminescence measurements.

The successful synthesis of *M*-plane (In,Ga)N/GaN multiple quantum wells (MQWs) is demonstrated. The composition profiles of these structures are investigated by both x-ray diffractometry and secondary ion-mass spectrometry. The results reveal significant In surface segregation, resulting in a reduced In content and much wider wells than intended. The resulting In content of $\sim$7% is lower than that obtained ($\sim$15%) for corresponding *C*-plane structures grown under identical conditions, suggesting a lower In incorporation efficiency on the ($1\bar{1}00$) plane compared to the (0001) plane. The dependence of the transition energies on the well thickness of these *M*-plane quantum wells evidences the absence of internal electrostatic fields along this growth direction. The recombination dynamics in these MQWs is investigated in detail, and is found to be strongly influenced by localized states. Furthermore, in contrast to *C*-plane (0001) structures, a strong in-plane anisotropy of the spontaneous emission with an energy-dependent polarization degree of up to 96% is observed in the *M*-plane (In,Ga)N/GaN MQWs.

Finally, the impact of the growth temperature and stoichiometry on the Mg incorporation in GaN($1\bar{1}00$) is investigated. Mg doping levels up to $8\times10^{20}$ cm$^{-3}$ can be obtained in *M*-plane GaN, with no observed degradation in crystal quality. Both Mg diffusion and surface segregation in *M*-plane GaN are observed. In addition, a pronounced dependence of the O incorporation on the Mg doping is observed, and attributed to the high reactivity of Mg with O. Both optical and electrical measurements indicate that Mg acts as an acceptor in the Mg-doped *M*-plane layers.

# Zusammenfassung

Thema dieser Arbeit ist die Synthese von Wurtzit *M*-plane (In,Ga)N$(1\bar{1}00)$-Heterostrukturen auf $\gamma$-LiAlO$_2$(100) mittels plasmaunterstützter Molekularstrahlepitaxie (MBE). Der Einfluß der Wachstumsbedingungen auf die strukturellen, morphologischen, und optischen Eigenschaften von *M*-plane GaN-Filmen werden untersucht. Ferner werden M-plane (In,Ga)N/GaN Multiquantenwells (MQWs) hergestellt und deren strukturelle und optische Eigenschaften untersucht. Schließlich wird der Einbau von Mg in *M*-plane GaN untersucht, um p-Typ-Leitfähigkeit zu erreichen.

Die Arbeit beginnt mit einer Einführung bezüglich der Verspannung und der elektrostatischen Polarisation in Nitriden. Die Motivation für das Wachstum in $[1\bar{1}00]$-Richtung anstatt in der konventionellen [0001]-Richtung ist, dass die GaN$(1\bar{1}00)$-Fläche nichtpolar ist, da sie aus einer gleichen Anzahl dreifach koordinierter Ga- und N-Atome aufgebaut ist. GaN ist überdies nicht piezoelektrisch in der $[1\bar{1}00]$-Richtung. Das daraus folgende Fehlen elektrostatischer Felder in dieser Richtung stellt einen klaren Vorteil für die Leistung von GaN-basierenden hocheffizienten Leuchtdioden (LEDs) dar. Entsprechende [0001]-orientierte Strukturen, die auf konventionellen Substraten wie Al$_2$O$_3$ und SiC abgeschieden werden, leiden unter einer verringerten Effizienz durch die Präsenz der spontanen und piezoelektrischen Polarisation in dieser Wachstumsrichtung.

Die Eigenschaften des Substrats LiAlO$_2$ in Bezug auf das MBE-Wachstum werden anschliessend diskutiert. Es wird gezeigt, daß die thermische Stabilität von LiAlO$_2$ für das MBE-Wachstum von Heterostrukturen geeignet ist. Die Polarität von LiAlO$_2$ hat einen entscheidenden Einfluß auf die Phasenreinheit der GaN-Filme, und die Wahl der richtigen Polarität ist Voraussetzung für die Herstellung von einphasigen *M*-plane GaN-Schichten.

In Kapitel 4 wird der Einfluß der Nukleationsbedingungen auf die strukturellen und morphologischen Eigenschaften von *M*-plane GaN-Filmen systematisch untersucht. Ferner wird die Ga-Adsorption und -Desorption ausführlich untersucht. Optimale Wachstumsbedingungen werden etabliert, die es ermöglichen, *M*-plane-GaN-Schichten hoher Qualität reproduzierbar zu erhalten. Die Mikrostruktur der *M*-plane-GaN-Schichten, untersucht mittels Transmissionselektronenmikroskopie, ist durch eine hohe Dichte an Stapelfehlern als dominierenden Defekt gekennzeichnet. Vollständige Fadenversetzungen, die die dominanten Defekte in *C*-plane GaN sind, werden dagegen nicht beobachtet. Die Korrelation zwischen den Stapelfehlern und den optischen Eigenschaften der Films wird untersucht. Eine intensive Emissionslinie wird in Tieftemperatur-Photolumineszenzspektren beobachtet, die an Stapelfehlern gebundenen Exzitonen zugeordnet wird.

In Kapitel 6 wird die erfolgreiche Synthese von *M*-plane-(In,Ga)N/GaN-MQWs beschrieben. Das Zusammensetzungsprofil dieser Strukturen wird mittels Röntgendiffraktometrie und Sekundärionenmassenspektrometrie untersucht. Die Ergebnisse belegen eine beträchtliche Oberflächensegregation von In, die zu einem erniedrigten In-Gehalt sowie stark verbreiterten Quantenwells führt. Der erhaltene In-Gehalt von 7% is niedriger als derjenige (15%), der in entsprechenden *C*-plane-Strukturen gefunden wird, die unter identischen Bedingungen hergesellt wurden. Dieses Resultat deutet auf eine niedrigere Einbaueffizienz von In auf $(1\bar{1}00)$ verglichen mit (0001) hin. Die Abhängigkeit der Übergangsenergien von der Quantenwellbreite dieser *M*-plane-MQWs belegt die Abwesenheit interner elektrostatischer Felder entlang der Wachstumsrichtung. Die Rekombinationsdynamik in diesen MQWs wird im Detail untersucht. Sie ist stark von lokalisierten Zuständen beeinflußt. Im Gegensatz zu *C*-plane-Strukturen, wird in diesen *M*-plane MQWs eine starke Polarisation der spontanen Emission in der Filmebene mit einem energieabhängigen Polarisationsgrad von bis zu 96% beobachtet.

In Kapitel 7 wird der Einfluß der Wachstumstemperatur und der Stöchiometrie auf den Mg-Einbau in GaN$(1\bar{1}00)$ zur p-Dotierung untersucht. Eine Mg-Konzentration bis zu $8\times10^{20}$ cm$^{-3}$ kann in *M*-plane-GaN-Schichten ohne beobachtbare Degradation der Kristallqualität erreicht werden. Es wird sowohl eine Diffusion als auch eine Segregation von Mg in *M*-plane GaN beobachtet. Zusätzlich wird eine ausgeprägte Abhängigkeit des O-Einbaus von der Mg-Dotierung beobachtet, was auf die hohe Reaktivität von Mg mit O zurückgeführt wird. Sowohl optische als auch elektrische Messungen weisen darauf hin, daß Mg in diesen *M*-plane GaN-Schichten als Akzeptor eingebaut wird.

Parts of this work have already been published or submitted:

Y. J. Sun, O. Brandt, U. Jahn, T. Y. Liu, A. Trampert, S. Cronenberg, S. Dhar, and K. H. Ploog, *Impact of nucleation conditions on the structural and optical properties of M-plane GaN ($1\bar{1}00$) grown on LiAlO$_2$,* J. Appl. Phys. **9**2, 5714 (2002)

Y. J. Sun, O. Brandt, S. Cronenberg, S. Dhar, H. T. Grahn, K. H. Ploog, P. Waltereit, and J. S. Speck, *Nonpolar In$_x$Ga$_{1-x}$N/GaN($1\bar{1}00$) multiple quantum wells grown on $\gamma$-LiAlO$_2$(100) by plasma-assisted molecular-beam epitaxy,* Phys. Rev. B **6**7, 041306(R) (2003)

Y. J. Sun, O. Brandt, M. Ramsteiner, H. T. Grahn, and K. H. Ploog, *Polarization anisotropy of photoluminescence of M-plane (In,Ga)N/GaN multiple quantum wells,* Appl. Phys. Lett. **8**2, 3850 (2003)

Y. J. Sun, O. Brandt, and K. H. Ploog, *Growth of M-plane GaN films on $\gamma$-LiAlO$_2$(100) with high phase purity,* J. Vac. Sci. Technol. B **2**1, 1350 (2003)

Y. J. Sun, O. Brandt, S. Cronenberg, H. T. Grahn, and K. H. Ploog, *Impact of exciton localization on the optical properties of non-polar M-plane In$_{0.1}$Ga$_{0.9}$N/GaN multiple quantum wells,* 5th International Conference on Nitride Semiconductors, Nara (Japan) 2003, Phys. Stat. Sol. B **2**40, 360 (2003)

Y. J. Sun, O. Brandt, B. Jenichen, and K. H. Ploog, *In surface segregation in M-plane (In,Ga)N/GaN multiple quantum well structures,* Appl. Phys. Lett. **8**3, 5178 (2003)

O. Brandt, Y. J. Sun, and K. H. Ploog, *Growth of M-plane III-N structures on $\gamma$-LiAlO$_2$(100),* 5th International Workshop on Epitaxial Semiconductors on Patterned Substrates and Novel Index Surfaces, Stuttgart (Germany), 2003, Physica E (to be published)

O. Brandt, Y. J. Sun, L. Däweritz, and K. H. Ploog, *Ga adsorption and desorption kinetics on M-plane GaN,* Phys. Rev. B (submitted)

Other publications related to this work:

Y. J. Sun, O. Brandt, T. Y. Liu, A. Trampert, K. H. Ploog, J. Bläsing, and A. Krost, *Determination of the azimuthal orientational spread of GaN films by x-ray diffraction,* Appl. Phys. Lett. **8**1, 4928 (2002)

P. Misra, Y. J. Sun, O. Brandt, and H. T. Grahn, *Angular dependence of the in-plane polarization anisotropy in the absorption coefficient of strained M-plane GaN films on $\gamma$-LiAlO$_2$,* 5th International Conference on Nitride Semiconductors, Nara (Japan) 2003, Phys. Stat. Sol. B **2**40, 293 (2003)

P. Misra, Y. J. Sun, O. Brandt, and H. T. Grahn, *In-plane polarization anisotropy and polarization rotation for M-plane GaN films on LiAlO$_2$,* Appl. Phys. Lett. **8**3, 4327 (2003).

# Inhaltsverzeichnis

# 1 Introduction

The recent advent of group III-nitrides has opened a new era in the field of semiconductor materials and devices. The III-nitrides, aluminum nitride (AlN), gallium nitride (GaN) and indium nitride (InN), are all direct band gap materials with band gaps (in hexagonal wurtzite structure) ranging from 0.7 eV ($\alpha$-InN) [1, 2] through 3.4 eV ($\alpha$-GaN) to 6.2 eV ($\alpha$-AlN). They form a complete series of ternary alloys which spans the whole visible spectrum and extends well into the infrared and ultraviolet (UV) region, i.e. from 1.7 $\mu$m to 200 nm. This advantage makes them ideal candidates for tailored optoelectronic devices, especially visible light emitters in the blue and green regions, which were previously difficult to achieve. For several decades with little success, billions of dollars have been expended in trying to make semiconductor diodes that emit blue light, especially blue lasers, operating continuously and at room temperature. Although realization of blue devices using II-VI compounds have been partially successful, [3] the problem of achieving acceptably long operating lifetimes has not yet been solved, thus leaving the space open to the III-nitride alternative.

**Historical Review of GaN** In the following, a brief history of the GaN is given. GaN was first synthesized by Johnson et al. in 1932 by passing ammonia through hot Ga [4]. Later, Juza and Hahn used the same technique and got GaN needles and platelets, that were used for studying the optical and structural properties [5, 6]. However, the progress in research and development of GaN before the 1970s was slowed down due to the lack of modern crystal growth techniques. With the technological development of epitaxial growth of high-quality thin films on appropriate substrate materials, in 1969 the first GaN was epitaxially grown by halide vapor phase epitaxy on sapphire [7]. The films at early time were unintentionally n-type doped, with electron concentrations ranging from $10^{18}$ to $10^{20}$ cm$^{-3}$. Such high n-type background concentrations made it difficult to achieve p-type doping. Most potential acceptor elements, such as Mg, Be, Zn and Cd, were incorporated into GaN, either during growth [8, 9, 10, 11] or by post-growth ion implantation [12], but there was no p-type conduction obtained. The first light emitting diode (LED) based on GaN was produced by a Zn-doped metal-insulator-semiconductor structure but showed only a low efficiency [13]. After this initial progress made during the 1970s, the pace of research of GaN became slow, because of the lack of high quality epilayers and the lack of success in making p-type GaN. The origin of high background doping was found to be due to O incorporation during the growth [14], instead of N vacancies as was assumed before. It was not until the modern growth techniques of molecular beam epitaxy (MBE) and metal-organic vapor phase epitaxy (MOVPE, also called metal-organic chemical vapor deposition, i.e. MOCVD) were developed that further development and progress took place. Strenuous efforts were made to optimize growth conditions and introduce more suitable buffer layers to reduce the n-type background doping levels. This eventually proved successful—background levels below $10^{17}$ cm$^{-3}$ at room temperature were achieved, in the late 1980s and the early 1990s. This remarkable progress was made by an insertion of either a low-temperature AlN [15, 16] or a low-temperature GaN buffer layer [17, 18] before the GaN growth. Concerning p-type doping, although the group II element Mg had long been expected to be a good acceptor dopant and significant amounts of Mg

could be incorporated into GaN during MOVPE growth, it was impossible to detect positive charge carriers at room temperature. The films turned out to be highly resistive. A rather accidental discovery allowed Amano et al. [19] to demonstrate that post-growth low-energy electron beam irradiation activates Mg-doped GaN films and converts them from the as-grown highly resistive state to a p-type conductive state. Previous observations in other III-V materials such as GaAs and InP had established that hydrogen incorporation plays a crucial role in passivating p-type dopants. Based on this knowledge, Nakamura et al. [20] have improved the activation of the Mg acceptors in MOVPE-grown GaN by utilizing thermal annealing in $N_2$. The resistivity was observed to drop from $\sim 10^6$ to 2 $\Omega$cm. These advances led to realizing the first GaN-based p-n junction LED in 1994 [21]. Present-day high-brightness nitride-based LEDs mostly comprise (In,Ga)N or GaN quantum well (QW) structures as active regions.
This breakthrough has paved the way for further rapid research and development of nitride-based devices. Compact solid state lamps consisting of high-brightness nitride-based LEDs are of current technological and commercial interest as an alternative to conventional Edison's fragile and energy-consuming light bulb. However, at present the best white LEDs made by combining blue InGaN LEDs and yttrium aluminum garnet (YAG) phosphor have only luminous efficiencies of $20-30$ lm/W, which is comparable with that of incandescent lamps, but lower than that of fluorescent lamps. Although their life time is orders of magnitude longer than conventional light bulbs, the expected energy-saving, with great economic and ecological consequences, is not yet realized. Nevertheless, GaN is one of the most promising wide bandgap semiconductors for applications in optoelectronic devices in the blue and ultraviolet (UV) wavelengths.

**Current Interest** Although the development of nitride-based light emitting devices has been achieved with great success, their luminous efficiencies, especially in the green or ultraviolet wavelength regions, are still quite low, due to the presence of electrostatic fields within the active layers [22]. These fields are generated by the spontaneous and piezoelectric polarization fields [23], since most structures are deposited along the conventional growth direction, i.e. [0001]. These polarization fields give rise to large internal electrostatic fields, which results in the confinement of a two-dimensional electron gas. Although this property can be used for certain device applications, for example, high electron mobility transistors (HEMT) [24,25,26], it is not desirable for light emitting devices, as the internal electrostatic field reduces the overlap of the electron-hole wave functions (quantum confined Stark effect) [22,27]. The poor overlap of electron-hole wavefunctions also results in a long radiative life time [28], and consequentially low internal quantum efficiency, as there are always some competing non-radiative recombination channels at elevated temperatures.
One solution to get rid of these notorious internal electric fields is the growth of cubic group III-nitride heterostructrures. [29,30] However, even after intense efforts [31,32], the lack of suitable substrates and the inherent thermodynamic metastability of this phase has detained the achievement of device-quality material. Alternatively, the wurtzite structure of $\alpha$-GaN indicates that any direction orthogonal to the unique [0001] axis, such as $[1\bar{1}00]$ and $[11\bar{2}0]$, is free of spontaneous polarization. In addition, these directions also do not carry piezoelectric polarization if shear stresses in the

growth plane are absent. Therefore, due to the resulting absence of electrostatic fields, these directions constitute a distinct advantage for fabricating high-efficiency GaN-based LEDs over corresponding [0001]-oriented structures on conventional substrates such as $Al_2O_3$(0001) and SiC(0001). Waltereit *et al.* first demonstrated an improved internal quantum efficiency of GaN/(Al,Ga)N quantum wells grown along the $[1\bar{1}00]$ direction on $\gamma$-$LiAlO_2$(100), as a result of the absence of internal electrostatic fields across the quantum wells [33]. This triggered a surge in studying nonpolar group-III nitride heterostructures [34,35,36,37,38,39,40,41,42,43,44,45]. Most recently, ultraviolet LEDs based on non-polar GaN/(Al,Ga)N$(11\bar{2}0)$ quantum wells have been realized [46].

**Aim of this work** As mentioned above, growth of $\alpha$-GaN along a nonpolar direction is a promising way to achieve high-efficiency light emitting devices, which is the motivation of this work.

As we see, getting rid of the internal electrostatic fields along the growth direction is an approach to improve the quantum efficiency. Fundamental knowledge concerning these fields in the wurtzite structure is thus needed, and is discussed in Chapter 2. Some important physical properties pertinent to that, such as strain and stress, spontaneous and piezoelectric polarization, are described. For the band structure calculation, one should also know how to estimate the strength of the internal electrostatic field caused by accumulation of polarization charges .

The substrate used in this work is $\gamma$-$LiAlO_2$, a rather novel candidate for the epitaxial growth of GaN. No detailed study of its properties with regard to the epilayers grown on this substrate has been yet carried out. Therefore, in Chapter 3, selected properties of $\gamma$-$LiAlO_2$ substrates are presented. Compared with conventional SiC or $Al_2O_3$ substrates, the $\gamma$-$LiAlO_2$ substrate provides some advantages, like small lattice mismatch and selectivity in the wet-chemical etching process. Most interesting, GaN$(1\bar{1}00)$ (the *M*-plane) can be realized on this substrate, which paves the way to get rid of the internal electrostatic fields. However, this promising substrate also has certain drawbacks. It is thermally and chemically unstable, which makes its preparation prior to the growth and growth very difficult.

Although there are a few reports on nonpolar group-III nitride heterostructures [34, 35, 36, 37, 38, 39, 40, 41, 42, 43, 44, 45], there is still a lack of a systematic knowledge of optimizing the growth of them. Chapter 4 starts with showing a systematic study of the impact of nucleation conditions on the growth of *M*-plane GaN$(1\bar{1}00)$ films with high phase purity. The optimum growth condition is then empirically established, and high quality *M*-plane GaN can be reproducibly obtained. Furthermore, a comprehensive study of Ga adsorption, desorption and consumption on the *M*-plane GaN is presented. All information obtained indicate an optimized growth regime for high quality *M*-plane GaN films. Based on this effort, the synthesis and investigation of (In,Ga)N/GaN MQWs becomes possible, which is presented in Chapter 6 .

A threading dislocation density of $10^8 - 10^{10}$ cm$^{-3}$ is typically observed in conventional *C*-plane GaN due to the large lattice and thermal mismatch between the SiC or $Al_2O_3$ substrates and the GaN layer. Good lattice match of $\gamma$-$LiAlO_2$(100) to *M*-plane GaN leads us to an investigation of the defects in *M*-plane GaN and their correlation with the optical properties of the films. Chapter 5 presents this study. In contrast to conventional *C*-plane GaN films, perfect threading dislocations in our *M*-plane GaN films are not detected. The dominant defects are basal plane stacking faults. The correlation of stacking faults and their optical properties is explored. A strong transition from excitons bound to stacking faults is observed at low temperature.

Although nonpolar wurzite GaN/(Al,Ga)N MQWs have been reported, either grown on $\gamma$-LiAlO$_2$(100) [33] or on $R$-plane($1\bar{1}02$) sapphire [34], their (In,Ga)N/GaN counterpart has not yet been seen in the literature. As the (In,Ga)N/GaN MQWs are widely used as active regions in group III-nitride-based optoelectronic devices, the growth of such structures is vital. The attempt of synthesizing $M$-plane (In,Ga)N/GaN MQWs has turned out to be successful. In incorporation into the $M$-plane orientation is discussed in Chapter 6. It is observed that significant In surface segregation occurs on the $M$-plane. Compared to the (0001) plane, a lower In incorporation efficiency on the ($1\bar{1}00$) plane is revealed. Nevertheless, these (In,Ga)N/GaN MQWs allow us to study their spontaneous emission mechanism. The presence of localized states has been found to be of importance to the spontaneous emission. Furthermore, a strong polarization anisotropy of the photoluminescence of such structures has been observed. This is interesting for the realization of polarization sensitive detectors. [47]

To realize LEDs based on $M$-plane GaN, p-type doping is definitely required. Therefore, Mg-doping of $M$-plane GaN is investigated. In Chapter 7, the impact of the growth temperature and stoichiometry on the Mg incorporation in GaN($1\bar{1}00$) is studied. A Mg doping level up to $8\times10^{20}$ cm$^{-3}$ can be obtained in the $M$-plane GaN, with no deterioration of the crystal quality. A pronounced dependence of O incorporation on Mg doping is observed, which is attributed to the high reactivity of Mg with residual O. Both optical and electrical measurements of Mg-doped $M$-plane GaN indicate that Mg, at least an appreciable amount, as acceptor.

A variety of characterization techniques have been employed during this work. Experimental details are not presented in a separate chapter, but are given in the relevant parts of the thesis.

# 2 Spontaneous and piezoelectric polarization in wurtzite group III-nitride heterostructures

In this Chapter, two of the most important properties with regard to wurtzite group III-nitride epilayers, i.e. strain and polarization fields, are briefly discussed, since they are of importance for the spontaneous emission of these materials.

## 2.1 Strain and stress

Most of group-III nitrides are grown on lattice mismatched substrates, such as $Al_2O_3$, SiC, and Si, so that strains are inevitably encountered in these materials systems. Therefore, a proper treatment of strains and stresses of epilayers is of importance to understand the modification of the band structure, which influences the optical and electrical properties of the material. In this section, the concept of strain and stress is outlined, in particular regarding the growth directions involved in this thesis, namely, $[1\bar{1}00]$ and [0001].

**Unit cell** The equilibrium structure of group-III nitrides is wurtzite. The unit cell is shown in Fig. 2.1.

The primitive translational vectors can be expressed in terms of the unstrained lattice constants $a_r$ and $c_r$ by

$$\begin{aligned} \mathbf{a}_1 &= a_\mathrm{r}\hat{\mathbf{e}}_x, \\ \mathbf{a}_2 &= -\frac{a_\mathrm{r}}{2}\hat{\mathbf{e}}_x + \frac{\sqrt{3}a_\mathrm{r}}{2}\hat{\mathbf{e}}_y, \\ \mathbf{a}_3 &= c_\mathrm{r}\hat{\mathbf{e}}_z \end{aligned} \tag{2.1}$$

with a set of orthonormal basis vectors ($\hat{\mathbf{e}}_\mathbf{x}$, $\hat{\mathbf{e}}_\mathbf{y}$, $\hat{\mathbf{e}}_\mathbf{z}$) in a Cartesian coordinate space.

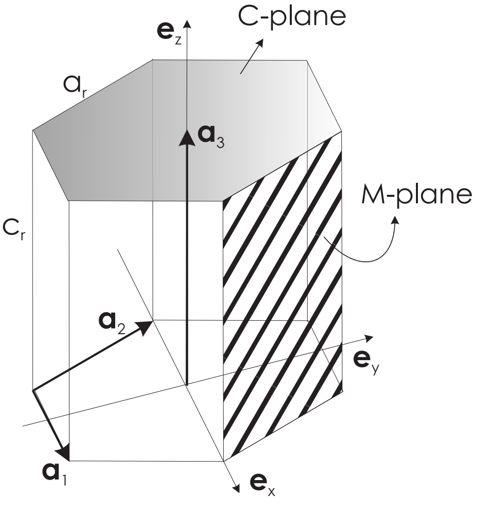

**Figure 2.1:** Scheme of the unstrained unit cell of wurtzite nitride semiconductors with the primitive translation vectors $\mathbf{a_i}$ and the set of Cartesian unit vectors ($\hat{\mathbf{e}}_\mathbf{x}$, $\hat{\mathbf{e}}_\mathbf{y}$, $\hat{\mathbf{e}}_\mathbf{z}$). $a_r$ and $c_r$ denote the unstrained lattice constants. The shaded and patterned areas present the C-plane and the M-plane, respectively.

**Strain tensor** The strain tensor describes the distortion of the unit cell with respect to the equilibrium structure. Under strain, the lengths and/or the directions of the primitive translational vectors are modified. The modified basis vectors ($\mathbf{e}'_\mathbf{x}$, $\mathbf{e}'_\mathbf{y}$, and $\mathbf{e}'_\mathbf{z}$) are related to the original set of vectors according to

$$\begin{array}{rcrcrcr} \mathbf{e}_x^{'} & = & (1+\epsilon_{xx})\,\hat{\mathbf{e}}_x & + & \epsilon_{xy}\,\hat{\mathbf{e}}_y & + & \epsilon_{xz}\,\hat{\mathbf{e}}_z \\ \mathbf{e}_y^{'} & = & \epsilon_{yx}\,\hat{\mathbf{e}}_x & + & (1+\epsilon_{yy})\,\hat{\mathbf{e}}_y & + & \epsilon_{yz}\,\hat{\mathbf{e}}_z \\ \mathbf{e}_z^{'} & = & \epsilon_{zx}\,\hat{\mathbf{e}}_x & + & \epsilon_{zy}\,\hat{\mathbf{e}}_y & + & (1+\epsilon_{zz})\,\hat{\mathbf{e}}_z \end{array} \tag{2.2}$$

with the strain tensor elements $\epsilon_{ij}$. The tensors consist of normal strain components $\epsilon_{xx}$, $\epsilon_{yy}$ and $\epsilon_{zz}$ as well as shear strain components $\epsilon_{xy}$, $\epsilon_{xz}$ and $\epsilon_{yz}$.

**Stress tensor** The stress tensor describes the pressure which has to be applied to the crystal in order to distort it. Similar to the strain tensor, the stress tensor has normal parts ($\sigma_{xx}$, $\sigma_{yy}$ and $\sigma_{zz}$) and shear parts ($\sigma_{xy}$, $\sigma_{xz}$ and $\sigma_{yz}$). The stress tensor is related to the strain tensor via the elastic constants according to Hooke's law. Considering the $C_{6v}$ symmetry of the wurtzite structure, one obtains, [48]

$$\begin{pmatrix} \sigma_{xx} \\ \sigma_{yy} \\ \sigma_{zz} \\ \sigma_{yz} \\ \sigma_{xz} \\ \sigma_{xy} \end{pmatrix} = \begin{pmatrix} C_{11} & C_{12} & C_{13} & 0 & 0 & 0 \\ C_{12} & C_{11} & C_{13} & 0 & 0 & 0 \\ C_{13} & C_{13} & C_{33} & 0 & 0 & 0 \\ 0 & 0 & 0 & C_{44} & 0 & 0 \\ 0 & 0 & 0 & 0 & C_{44} & 0 \\ 0 & 0 & 0 & 0 & 0 & C_{66} \end{pmatrix} \begin{pmatrix} \epsilon_{xx} \\ \epsilon_{yy} \\ \epsilon_{zz} \\ \epsilon_{yz} \\ \epsilon_{xz} \\ \epsilon_{xy} \end{pmatrix} \tag{2.3}$$

The samples investigated in this thesis were grown either along $[1\bar{1}00]$ or [0001] direction. In both cases, shear components of both stresses and strains are absent since the angles between the primitive translational vectors are conserved by stress along one of the unit vectors $\hat{\mathbf{e}}_\mathbf{x}$, $\hat{\mathbf{e}}_\mathbf{y}$,or $\hat{\mathbf{e}}_\mathbf{z}$. Therefore, the strain tensor has only three non-vanishing terms, namely, $\epsilon_{xx}$, $\epsilon_{yy}$ and $\epsilon_{zz}$.

**Growth along [0001]** In this case, the growth plane corresponds to the $xy$-plane and deposition takes place along the $z$ direction. As all C-plane samples were grown along [0001], the treatment of stress-strain relationship can be further simplified, since the in-plane strain is isotropic. Then the in-plane and out-of-plane strain components can be expressed as $\epsilon_{\|}$=$\epsilon_{xx}$=$\epsilon_{yy}$ and $\epsilon_{\perp}$=$\epsilon_{zz}$ (note: here the symbol $\|$ and $\perp$ indicate in-plane and out-of-plane, respectively. It is also applied hereafter). Equation (2.3) now reads

$$\begin{pmatrix} \sigma_{\|} \\ \sigma_{\perp} \end{pmatrix} = \begin{pmatrix} C_{11}+C_{12} & C_{13} \\ 2C_{13} & C_{33} \end{pmatrix} \begin{pmatrix} \epsilon_{\|} \\ \epsilon_{\perp} \end{pmatrix} \tag{2.4}$$

Since the film is free to expand or shrink along the growth direction, the out-off-plane stress $\sigma_{\perp}$ is equal to zero, and we thus obtain

$$\frac{\epsilon_{\perp}}{\epsilon_{\|}} = -2\frac{C_{13}}{C_{33}} \tag{2.5}$$

which describes the Poisson effect.

**Growth along $[\mathbf{1\bar{1}00}]$** In this case, the growth plane is the $xz$-plane, while the growth direction is along the $y$ axis. The in-plane strain of an epilayer is usually anisotropic ($\epsilon_{xx} \neq \epsilon_{yy}$), unlike the case of the $C$-plane films. Nevertheless, the out-of-plane stress ($\sigma_{yy}$) is zero. So the relation between the out-of-plane strain and the in-plane strain can be derived:

$$\epsilon_{yy} = \frac{-C_{12}\epsilon_{xx} - C_{13}\epsilon_{zz}}{C_{11}} \tag{2.6}$$

## 2.2 Electrical polarization

A noticeable red-shift of the spontaneous emission from wurzite nitride semiconductor quantum wells has been observed by many groups [28, 49, 50, 51], when the well thickness is increased. This phenomenon is attributed to the quantum-confined Stark effect (QCSE) caused by strong internal electrostatic fields along the growth direction. The underlying reason is the presence of huge polarization fields in the wurtzite nitride heterostructure, which has a singular polar axis and lacks inversion symmetry. The polarization consists of spontaneous and piezoelectric components. In the absence of external electric fields, the total macroscopic polarization $\mathbf{P}$ in a crystal is the sum of the spontaneous polarization $\mathbf{P_{sp}}$ in the equilibrium lattice and the strain-induced piezoelectric polarization $\mathbf{P_{pe}}$.

**Spontaneous polarization** The zincblende structure has four symmetry equivalent polar $\langle 111 \rangle$ axes which cancel the polarization contribution of each other, and is free of electrical polarization at equilibrium along the $\langle 001 \rangle$ direction. In contrast, the wurtzite structure has a singular polar axis, namely, the [0001] axis ($c$-axis). Thus, there is a spontaneous polarization along the $c$-axis even at equilibrium. However, both the prism $(1\bar{1}00)$ plane and the prismatic $(11\bar{2}0)$ plane are nonpolar since they are composed of equal numbers of threefold coordinated Ga and N atoms.

**Piezoelectric polarization** In practice, group III-nitride semiconductor structures are grown under strain, due to the existence of lattice mismatch with regard to the underlying layer. The consequent deformation of the unit cell leads to the piezoelectric polarization, which, like the spontaneous polarization, is related to the unit cell symmetry. Zincblende films grown along the $\langle 001 \rangle$ direction are free of the piezoelectric polarization since contributions from the four polar axes cancel each other. Films oriented along one of the polar axes, however, encounter the piezoelectric polarization. The wurtzite structure with its unique polar [0001] axis always carries piezoelectric polarization along the $c$-axis. This thesis is concerned with the wurtzite structure, so that we focus on this structure in the following. In general, the unit cell can be under arbitrary strain. The piezoelectric polarization is obtain by relating the piezoelectric tensor ($e_{ij}$) of the space group P6$_3$mc to the strain

$$\mathbf{P}_{\mathrm{PZ}} = \begin{pmatrix} 0 & 0 & 0 & 0 & e_{15} & 0 \\ 0 & 0 & 0 & e_{15} & 0 & 0 \\ e_{31} & e_{31} & e_{33} & 0 & 0 & 0 \end{pmatrix} \begin{pmatrix} \epsilon_{xx} \\ \epsilon_{yy} \\ \epsilon_{zz} \\ \epsilon_{yz} \\ \epsilon_{xz} \\ \epsilon_{xy} \end{pmatrix} = \begin{pmatrix} e_{15}\epsilon_{xz} \\ e_{15}\epsilon_{yz} \\ e_{31}(\epsilon_{xx}+\epsilon_{yy}) + e_{33}\epsilon_{zz} \end{pmatrix} \tag{2.7}$$

As mentioned earlier, no shear strain is present in the samples investigated in this thesis, therefore, both $\epsilon_{xz}$ and $\epsilon_{yz}$ vanish. The total polarization for the growth along [0001] and [1$\bar{1}$00] is

$$P^{C}_{\mathrm{PZ},[0001]} = e_{33}\epsilon_{\perp} + 2e_{31}\epsilon_{||} \tag{2.8}$$

and

$$P^{M}_{\mathrm{PZ},[1\bar{1}00]} = e_{15}\epsilon_{xz} = 0 \tag{2.9}$$

Symbol $C$ and $M$ in the equations above mean $C$-plane and $M$-plane systems, respectively. As we see, the total polarization along the [1$\bar{1}$00] direction is zero. However, one should keep in mind that the in-plane piezoelectric polarization in $M$-plane GaN is still present along the $c$-axis, with the magnitude of

$$P^{M}_{\mathrm{PZ},[0001]} = e_{31}(\epsilon_{xx}+\epsilon_{yy}) + e_{33}\epsilon_{zz}$$

**Nonlinearity of macroscopic polarization** The electrical polarization in nitride alloys were usually estimated by a linear interpolation between the values of the parent binary compounds [23, 52], which follows a Vegard-like law as a function of composition. However, a theoretical calculation from Bernardini and Fiorentini suggested a nonlinearity of macroscopic polarization in nitride alloys [53], which was later demonstrated by experimental results [54]. In this thesis, we use this approach for the calculation of the polarization. In general, the spontaneous polarization of a random ternary nitride alloy A$_x$B$_{1-x}$N can be expressed as, in C/m$^2$,

$$P^{SP}_{A_xB_{1-x}N} = xP^{SP}_{AN} + (1-x)P^{SP}_{BN} + bx(1-x) \tag{2.10}$$

where b is the bowing parameter.
For the piezoelectric polarization, it was shown in Ref. [53] that Vegard's law is still applicable if the nonlinearity of the the bulk piezoelectric polarization of the component binaries as a function of strain is taken into account. Then, for a generic A$_x$B$_{1-x}$N alloy, the piezoelectric polarization reads:

$$P^{PZ}_{A_xB_{1-x}N} = xP^{PZ}_{AN}[\epsilon(x)] + (1-x)P^{PZ}_{BN}[\epsilon(x)] \tag{2.11}$$

Note that the calculation of the piezoelectric polarization of the binary compounds for symmetry-conserving in-plane biaxial strains using Eq. (2.8) no longer holds, where the piezoelectric constants ($e_{33}$) and ($e_{31}$) are calculated in the equilibrium structure of the binary and are, by definition, independent of strain. Instead, the strain-dependent

**Table 2.1:** Lattice constants and spontaneous polarization of wurtzite group-III nitride semiconductors.

| | GaN | InN | AlN |
|---|---|---|---|
| $a_r$ $(nm)$ | $0.31876^a$ | $0.353715^b$ | $0.31120^c$ |
| $c_r$ $(nm)$ | $0.51846^a$ | $0.570360^b$ | $0.49820^c$ |
| $P_{SP}$ (C m$^{-2}$)$^d$ | $-0.034$ | $-0.042$ | $-0.090$ |

[a] Ref. [55];
[b] average value from Ref. [55] and Ref. [56];
[c] Ref. [57];
[d] Ref. [58];

bulk piezoelectric polarization $P^{PZ}_{(A,B)N}(\epsilon(x))$ of the relevant group III-nitride binary compounds is [54] ,

$$\begin{array}{l} P^{PZ}_{AlN} = -1.808\epsilon_{\|} + 5.624\epsilon_{\|}^2 \quad for \ \ \epsilon < 0, \\ P^{PZ}_{AlN} = -1.808\epsilon_{\|} - 7.888\epsilon_{\|}^2 \quad for \ \ \epsilon > 0, \\ P^{PZ}_{GaN} = -0.918\epsilon_{\|} + 9.541\epsilon_{\|}^2, \\ P^{PZ}_{InN} = -1.373\epsilon_{\|} + 7.559\epsilon_{\|}^2 \end{array} \tag{2.12}$$

It should be pointed that the coefficients in Eq. (2.12) are related, but not equal to the usual piezoelectric constants.

**Material parameters** In practice, the accurate interpretation of polarization effect using the abovementioned formulas strongly depends on the proper choice of materials parameters, such as lattice constants and polarization coefficients. In addition, lattice constants are also crucial for the precise determination of structural parameters by x-ray diffraction, which is used routinely for the analysis of quantum well structures in this work. The parameters chosen here are listed in Tab. 2.1.

## 2.3 Internal electrostatic fields due to electrical polarization

To give an example of the possible influence of polarization on the physical properties of nitride-based heterostructures, the internal electrostatic field caused by polarization within a Ga-face [0001]-oriented GaN/(In,Ga)N/GaN quantum well is calculated as below. The In$_x$Ga$_{1-x}$N alloy is assumed to be grown pseudomorphically on the GaN barrier, ie., $a_{In_xGa_{1-x}N} = a_{GaN}$, while GaN is fully relaxed. According to Eq. (2.10), the spontaneous polarization in the In$_x$Ga$_{1-x}$N well is

$$P^{SP}_{In_xGa_{1-x}N} = -0.042x - 0.034(1-x) + 0.038x(1-x) \quad \mathrm{C\,m^{-2}} \tag{2.13}$$

Here, the values of spontaneous polarization for GaN and InN are taken from Ref. [58], while the bowing parameter is chosen from Ref. [53,54]. In conjunction with Eq. (2.12), Eq. (2.11) yields the piezoelectric polarization in the well,

$$P^{PZ}_{In_xGa_{1-x}N} = xP^{PZ}_{InN} + (1-x)P^{PZ}_{GaN} = (-1.982\epsilon^2 - 0.455\epsilon)x - 0.918\epsilon + 9.541\epsilon \quad \mathrm{C\,m^{-2}} \tag{2.14}$$

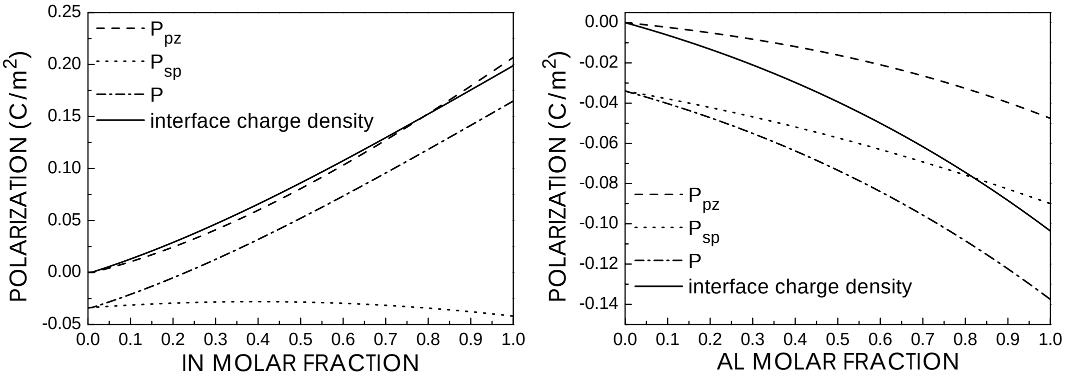

**Figure 2.2:** Polarization (spontaneous, piezoelectric, total) of (a) a fully-strained $In_xGa_{1-x}N$ layer and (b) a fully-strained $Al_xGa_{1-x}N$ layer on the relaxed GaN as a function of the In and Al content, respectively. The interface charge $\sigma$ for both cases is also plotted.

where

$$\epsilon = \frac{a_0 - a(x)}{a(x)} = \frac{-0.034955x}{0.31876 + 0.034955x} \tag{2.15}$$

where $a_0$ is the relaxed GaN lattice constant, as a thick GaN buffer is deposited first. The total polarization reads:

$$P(InGaN) = P^{SP}_{InGaN} + P^{PZ}_{InGaN} \tag{2.16}$$

The GaN barrier is assumed to be free of strain, therefore the piezoelectric polarization is equal to zero. The total polarization of the GaN simply equals its spontaneous polarization, that is,

$$P(GaN) = P^{SP}_{GaN} = -0.034 \quad \mathrm{C\,m^{-2}} \tag{2.17}$$

The difference in polarization of (In,Ga)N and GaN leads to a charge density at the (In,Ga)N/GaN interfaces, $\sigma$:

$$\pm\,\sigma = P_{InGaN} - P_{GaN} \quad \mathrm{C\,m^{-2}} \tag{2.18}$$

Once the interface charge density is known, it is convenient to insert an artificial $\delta$-doping layer at the interface as a result of the two-dimensional charges for self-consistent Schrödinger-Poisson calculations, with a sheet carrier density,

$$n_s = \frac{\sigma}{e} \quad \mathrm{m^{-2}} \tag{2.19}$$

where e is the elementary charge.

For GaN/(Al,Ga)N heterostructures, the polarization charge can be obtained in an analogous way.

The calculated spontaneous $P^{SP}$, piezoelectric $P^{PZ}$ and total polarization P as well as the interface charge density for both (In,Ga)N/GaN and GaN/(Al,Ga)N heterostructures are shown in Fig. 2.2 (a) and (b), respectively. Note that in (In,Ga)N/GaN heterostructures the polarization contribution from the piezoelectric polarization is dominant, while the spontaneous polarization has more influence in GaN/(Al,Ga)N heterostructures. Furthermore, based on Eq. (2.19), the doping sheet density used, for example, in self-consistent Schrödinger-Poisson calculations are plotted versus the In or Al fraction in Fig. 2.3 (a) and (b), respectively.

In the next paragraphs, the impact of the electrical polarization on [0001] and $[1\bar{1}00]$ oriented (In,Ga)N/GaN quantum wells will be discussed. The examples evidence that the former exhibit strong internal electrostatic fields normal to the wells, while the latter are free of such fields. For both cases, a 10-period $In_{0.15}Ga_{0.85}N$/GaN multiple quantum wells structure pseudomorphically grown on either a GaN(0001) or a GaN$(1\bar{1}00)$ buffer layer is taken as an example. The wells are thus fully strained. The well and barrier thickness are assumed to be 3 nm and 7 nm, respectively.

**[0001]-oriented quantum wells** In this structure, the growth direction is parallel to the total polarization vector $\mathbf{P}$. This polarization results in charges with alternating sign which are built up at the interfaces, which in turn results in internal electrostatic fields [Fig. 2.4 (a)]. The strength of these fields can be calculated in an analytical way [59], which, however, is valid only under certain circumstances since it neglects free carrier screening and the finite number of periods. Hence, a self-consistent solution is required. In this work, a freeware program [60] is used to simultaneously solve the Poisson and Schrödinger equations in an effective mass approximation. To give an example, the background electron doping concentration is set to $10^{17}$ cm$^{-3}$, according to the Hall measurements on our typical undoped *C*-plane samples. The calculated results are shown in Fig. 2.4. The electric field in the well is as large as 1.9 MV/cm. The strong internal electrostatic fields within the layers cause a localization of the electron and hole wavefunctions at both sides of the quantum well. This carrier separation has two consequences. First, the interband transition energy red-shifts by more than 200 meV, compared with the flat-band condition with quantum confinement [*cf.* Fig. 2.5 (b)]. Second, the spatial separation of electron and hole wavefunctions reduces the overlap between them and thus the transition probability. As a result, the radiative decay time is prolonged due to the reduced oscillator strength for recombination. The long life time of carriers increases the probability of carriers captured by nonradiative centers. Furthermore, the quantum-confinement Stark effect and the spatial separation of wavefunctions are more pronounced as the well thickness increases.

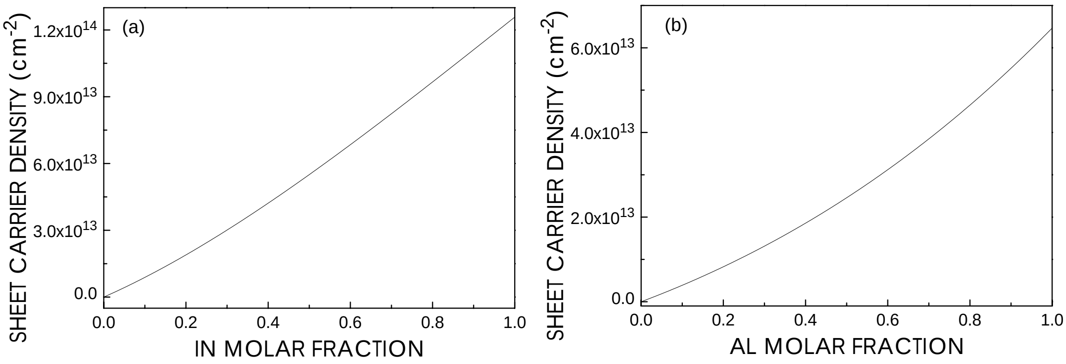

**Figure 2.3:** Calculated sheet carrier densities reflecting the two dimensional charges at interface due to polarization fields: (a) a fully-strained $In_xGa_{1-x}N$ layer and (b) a fully-strained $Al_xGa_{1-x}N$ layer on the relaxed GaN as a function of the In and Al content, respectively.

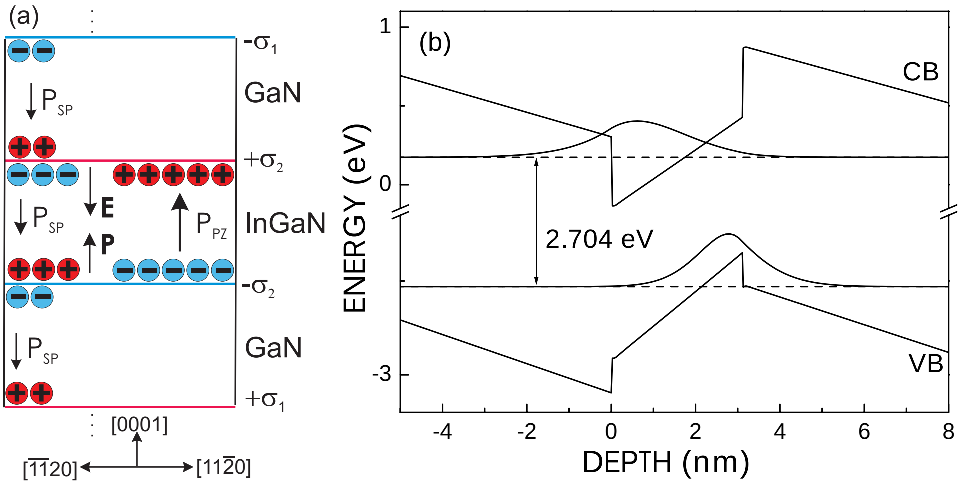

**Figure 2.4:** (a) Scheme of influence of electrical polarization on a 10-period (3 nm In$_{0.15}$Ga$_{0.85}$N)/(7 nm GaN) MQW pseudomorphically grown on a GaN(0001) buffer. The changes in total polarization of the individual layers lead to interface charges, which further result in strong internal electrostatic fields. (b) Calculated band profile, energy state, and electron-hole wavefunctions of this structure. Note the spatial separation of electron-hole wavefunctions. CB and VB denote the conduction band and valence band, respectively.

**[1$\bar{1}$00]-oriented quantum wells** In contrast to the *C*-plane structure mentioned above, the growth direction of the *M*-plane structures is normal to the direction of the total polarization. Therefore, there is no change in the polarization component along the growth direction and no charge accumulation at the interfaces, as shown in Fig. 2.5 (a). A flat-band condition in principle exists in such oriented heterostructures.
Obviously, the emission energy from quantum wells is solely determined by quantum confinement. The overlap of electron-hole wavefunctions is close to unity, which enhances the recombination efficiency. The subjective of this work is to grow and study structures based on non-polar *M*-plane nitrides.

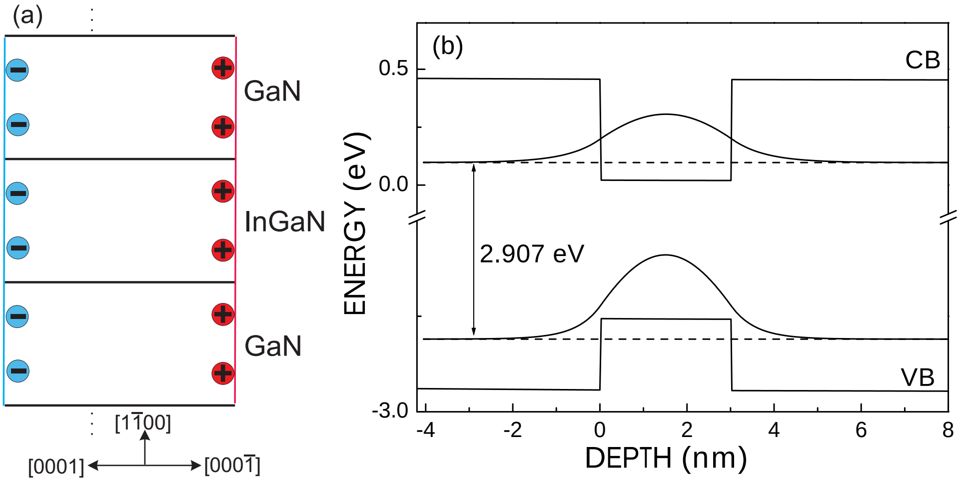

**Figure 2.5:** (a) Influence of electrical polarization on a 10-period (3 nm In$_{0.15}$Ga$_{0.85}$N)/(7 nm GaN) MQW pseudomorphically grown on a GaN(1$\bar{1}$00) buffer. The scheme of one period (a) and calculated band profile, energy state, and electron-hole wavefunctions of this structure (b). Note the difference from Fig. 2.4.

# 3 Substrate: $\gamma$-LiAlO$_2$

This chapter first gives a brief description of the crystal structure of $\gamma$-LiAlO$_2$, used as substrate in this study. Then its preparation for growth is discussed. Selected properties of LiAlO$_2$ wafers related to the epilayers are pointed out.

## 3.1 Properties of $\gamma$-LiAlO$_2$

**Crystal structure** $\gamma$-LiAlO$_2$ (LAO) has a tetragonal structure with lattice constants a=b= 0.51687 nm and c= 0.62679 nm and belongs to the space group P4$_1$2$_1$2 [61]. The LAO(100) plane exhibits a comparatively small lattice mismatch to GaN(1$\bar{1}$00) (the M-plane), namely, $[0001]_{\mathrm{GaN}} \| [010]_{\mathrm{LAO}}$ $\sim$0.3% and $[11\bar{2}0]_{\mathrm{GaN}} \| [001]_{\mathrm{LAO}}$ $\sim$1.7%, while conventional substrates used for epitaxy of GaN have much larger lattice mismatch (*cf.* Table 3.1). Most interestingly, as we dicussed in Chapter 2, the [1$\bar{1}$00]-oriented GaN thus grown on $\gamma$-LiAlO$_2$(100) can prove advantages for improving the internal quantum eifficiency of light-emitting devices, as it is free of eletrostatic fields along the growth direction. In addition, LAO can be selectively etched with respect to the GaN epilayers, allowing the fabrication of on-chip LEDs.

Figure 3.1 schematically displays the top view for LAO(100), and SiC(0001) as well for comparison. The previous report of GaN(0001) on LAO(100) [62] might be the consequence of the near-hexagonal symmetry on the substrate surface, as indicated by the dark shaded areas in Fig. 3.1 (a), probably due to the improper nucleation (*cf.* section 4.1). From the energetics point of view [63], GaN(1$\bar{1}$00) on LAO(100) is more favorable than GaN(0001) on LAO(100).

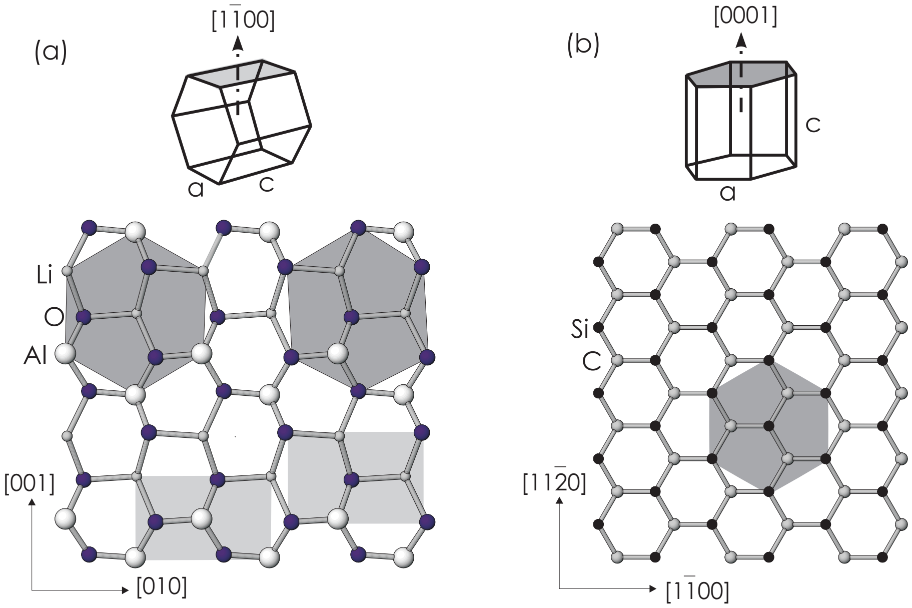

**Figure 3.1:** Unit cells and ball-and-stick models for the growth of GaN on $\gamma$-LiAlO$_2$(100) (a) and SiC(0001) (b). The light and dark shaded areas represent nucleation sites for GaN(1$\bar{1}$00) and GaN(0001). Modified from Ref [64].

**Table 3.1:** Properties of substrates used for GaN. a, f, and $\alpha$ denote the effective in-plane lattice constant, the in-plane lattice mismatch, and the in-plane thermal expansion coefficient, respectively. The price corresponds to a 2-inch wafer (US$).

| Substrate | Symmetry | a ($\mathring{A}$) | f(%) | $\alpha$ ($10^{-6}$)$K^{-1}$ | price |
|---|---|---|---|---|---|
| $\gamma$-$LiAlO_2$(100) | tetragonal | 5.1687/6.2679 | -0.3/-1.7 | 7.5 | 500 |
| $Al_2O_3$(0001) | hexagonal | 4.758 | −14 | 7.5 | 150 |
| 6H-SiC(0001) | wurtzite | 3.08123 | −3.3 | 3.2 | 1000 |
| 4H-SiC(0001) | wurtzite | 3.07902 | −3.4 | 3.2 | 1000 |
| Si(111) | cubic | 3.8396 | +20.4 | 3.59 | 20 |
| GaN(0001) | hexagonal | 3.1876 | 0 | 5.59 | – |

**Properties list** To select a suitable substrate, several issues concerning its properties must be considered, for example, lattice matching, thermal matching, price and processing issues. Table 3.1 lists properties of substrates currently used for group III nitride epitaxy. Currently, commercial group III-nitride based devices use either sapphire or SiC as substrates. The most fascinating property of GaN($1\bar{1}00$) is the absence of internal electrostatic field normal to the surface, which makes the growth of GaN on $LiAlO_2$ interesting for both research and device fabrication.

**Disadvantage** Despite the potential merits of LAO as substrate for GaN as mentioned above, it also possesses a number of drawbacks which one should bear in mind. For instance, LAO is inhomogeneously etched by a variety of acids [65], making chemical polishing an intricate task. Worse, LAO is hydrolytic [66], and care must be taken to limit the exposure to $H_2O$ to a brief dip. Furthermore, LAO is thermally much less stable than, for example, $Al_2O_3$ or SiC, despite its high melting point of about 1700°C [67]. Lee *et al.* [68] pointed out that the dissociation of LAO at the typical metal organic chemical vapor deposition (MOCVD) growth temperature of $\sim$1040°C might restrict its use to the MBE technique and indeed the incongruent evaporation of $Li_2O$ occurs at high temperature [69]. However, we did not observe the potential dissociation of this material below 1300°C in vacuum, as seen in the following paragraphs.

**$LiAlO_2$ dissociation** The thermal dissociation of $LiAlO_2$ is expected to occur according to the following reactions: [69]

$$\begin{aligned}
2LiAlO_{2(s,l)} &\rightarrow Li_2O_{(g)} + Al_2O_{3(s)}, \\
Li_2O_{(g)} &\rightarrow 2Li_{(g)} + \frac{1}{2}O_{2(g)}, \\
Al_2O_{3(s)} &\rightarrow Al_2O_{(g)} + O_{2(g)}, \\
Al_2O_{(g)} &\rightarrow 2Al_{(g)} + \frac{1}{2}O_{2(g)}, \\
O_{2(g)} &\rightarrow 2O_{(g)}
\end{aligned}$$

Note that the melting points for $LiAlO_2$, $Li_2O$ and $Al_2O_3$ are 1700°C [67], 1570°C, and 2054°C, respectively. The dominant partial pressure at and below 1700°C was found

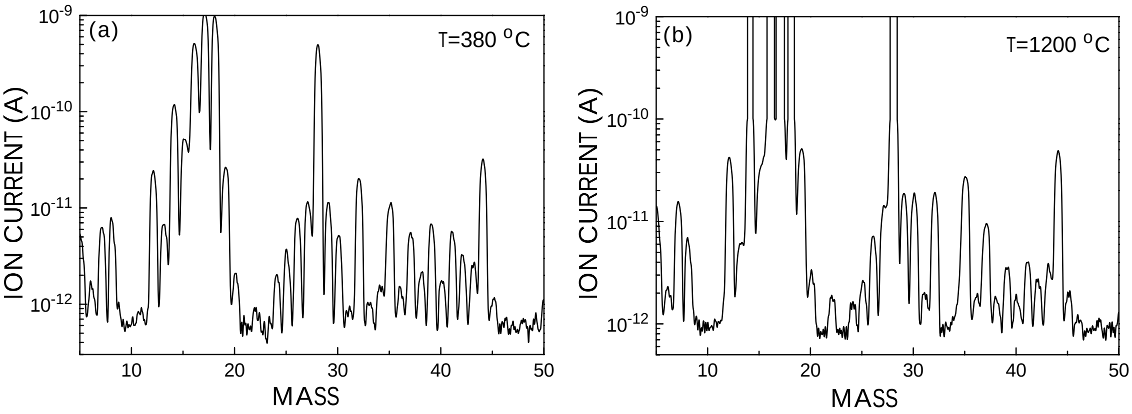

**Figure 3.2:** Mass spectra of $LiAlO_2$ heated to 380°C (a) and 1200°C (b), respectively.

to be from $Li_2O$ with mass 30 [69].

0.1 $cm^{-3}$ $\gamma$-$LiAlO_2$ was filled into an effusion cell, which was then mounted in a bake-out system with a base pressure $1\times10^{-8}$ torr. The $LiAlO_2$ was outgassed at 300°C for 2 hours. The effusion cell was then heated slowly up to 1324°C. A quadrapole mass spectroscope was used for detection. A series of mass spectra at various temperatures was recorded. Figure 3.2 (a) and (b) show the spectra at 380°C and 1200°C, respectively. The peak at Mass 30 is clearly observed, however, even before introducing $LiAlO_2$, and thus presumably related to NO. This peak rises when the temperature increases, while other peaks in the spectra also go up, which can be featured in Fig. 3.3. Mass 12 is chosen as a reference, because C is a common residual element in the high vacuum chamber. The similar temperature evolution for Mass 30 and 12 indicates a normal chamber outgassing process. Significant $LiAlO_2$ dissociation is not observed. This suggests that the decomposition of $LiAlO_2$ below 1324°C is indeed insignificant, in contrast to the conclusion of Lee *et al.* [68].

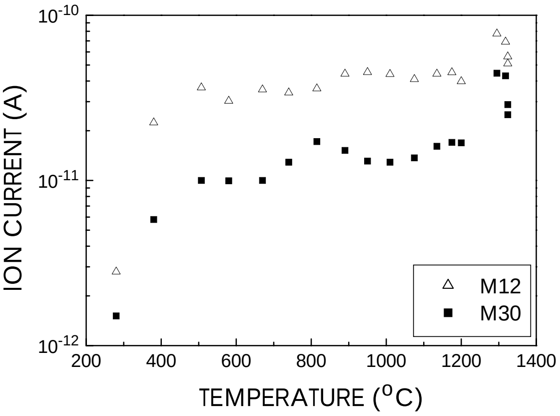

**Figure 3.3:** The intensity of Mass 30 and 12 in mass spectra as a function of temperature of the effusion cell.

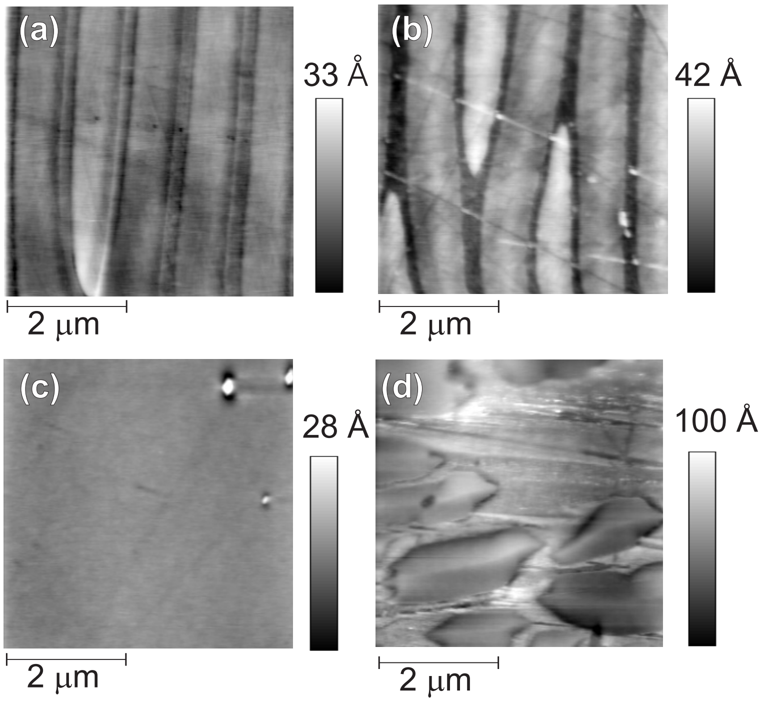

**Figure 3.4:** 5×5 $\mu$m$^2$ AFM micrographs of a typical AE $\gamma$-LiAlO$_2$(100) substrate, side A (a) and the opposite side B (b), a NP one from side A (c) and side B (d).

## 3.2 $\gamma$-LiAlO$_2$(100) substrates

The $\gamma$-LiAlO$_2$ substrates used in this study were grown by Czochralski method at the Institut für Kristallzüchtung and chemo-mechanially polished by a commercial vendor[1].

**Surface morphology** It is clear that the surface quality of substrate has decisive influence on the epilayer. The surface morphology of LiAlO$_2$ is checked by atomic force spectroscopy (AFM). We use a Park Scientific Instruments AFM system operating in contact mode. Figure 3.4 (a) and (b) shows both sides of the surface morphology of a typical long-term air-exposed (AE) LAO(100) substrate, while Fig. 3.4 (c) and (d) present a LAO substrate kept in an inert atmosphere (N$_2$) before mounting. Hereafter we call such a substrate N$_2$-protected (NP) LAO. The surface of AE LAO(100) appears still quite smooth as indicated from the peak-to-valley (P/V) roughness of less than 5 nm and an RMS roughness of 0.36 and 0.67 nm for face A and B, respectively. However, a periodic trench pattern is clearly observed on both sides. The stripes run along the [001] direction. In contrast, NP LAO substrates do not exhibit this pattern. Side A of a typical NP LAO substrates has featureless areas among random distributed submicrometer-scale hillocks. The P/V roughness and RMS roughness of those smooth regions have values of 1.6 nm and 0.12 nm, respectively, across a 3×3 $\mu$m$^2$ area, indicating a high surface quality. In contrast, side B of a typical NP LAO substrate exhibit a high density of shallow depression, as shown in Fig. 3.4 (d). Note that for both AE and NP LAO substrates, side A and B can be distinguished by

---

[1] CrysTec GmbH Kristalltechnologie, Köpenicker Str. 325, D-12555 Berlin, Germany

chemical etching, as side A is more resistive to the acid than side B. Furthermore, pure *M*-plane epilayers are preferentially grown on side A (see section 3.3).

Although the origin of a trench pattern on the AE LAO surface is unclear yet and still under investigation, we believe that it might be the result of the substrate's reaction to air, since we do not observe this pattern from the NP substrates. Under exposure to water vapor and carbon dioxide at 25°C, $\gamma$-LAO was found to react with both $H_2O$ and $CO_2$ to produce the complex resultants [66].

$$4\mathrm{LiAlO_2} + 9\mathrm{H_2O} + 2\mathrm{CO_2} \rightarrow \mathrm{Li_2Al_4(CO_3)(OH)_{12}} \cdot 3\mathrm{H_2O} + \mathrm{Li_2CO_3}$$

It should be pointed that this reaction might occur via a multistep mechanism involving amorphous intermediates [66]. However, examination by time-of-flight secondary-ion mass spectroscopy (TOF-SIMS) and x-ray photoelectron spectroscopy (XPS) did not reveal any evidence for the existence of other compounds on the surface of either type of substrates. There is also no composition difference between AE and NP substrates. Therefore, the change of surface morphologies of our substrates might be a low-angle faceting process with time, promoted by an as yet unknown chemical reaction.

Nevertheless, it is evident the surface quality of $LiAlO_2$ is inferior, compared with the typical state-of-the-art polished SiC or $Al_2O_3$ substrates. Further improvement of the surface morphology of $LiAlO_2$ substrate would be highly desirable.

The influence of AE and NP LAO substrates on the epilayers' properties is studied in this work. It is demonstrated that except for the surface morphology, all other properties are virtually identical for layers grown on either substrate. In fact, the epilayers grown on NP LAO substrate have better surface morphology than their counterpart on AE LAO (see section 4.2). The dominant micro-defects in layers grown on either type of substrate are basal plane stacking faults. Furthermore, the optical properties are essentially identical [see section 5.1]. The comparison of fundamental properties of GaN($1\bar{1}00$) grown on such two kinds of LAO substrates is presented in the Chapter 4 and Chapter 5, while LAO substrates involved in other chapters refer to NP ones, if not specified.

**Substrate preparation** Substrate preparation should deserve the most attention, in order to obtain reproducible high-quality epilayer. Usually, a chemical preparation before loading into the growth reactor is performed. In the MOCVD technique, sapphire is commonly treated by a flux of $H_2$ prior to deposit of a low-temperature buffer. For SiC substrates, a dramatic improvement of the surface quality is attained after annealing the wafers to about 1600°C in flowing $H_2$ [70]. Etched SiC wafers exhibit a well-ordered stepped surface. Since LAO is attacked by various acids and even water, and the well-established cleaning process for other substrates used for GaN growth is obviously not applicable for this case. In fact, we have not yet found any effective method, such as thermal or chemical etching to improve the surface morphology of the as-received LAO, especially considering the periodic pattern on the AE LAO substrates. The as-received substrates were thus only degreased sequentially in trichloroethylene (10 min), acetone (5 min) and methanol (5 min) in an ultrasonic bath. Finally, the substrate was dipped briefly ($30-60$ s) in deionized water (DI $H_2O$). The LAO substrate was then fixed with In onto a Si substrate clipped to a Mo holder. Prior to growth, the substrate was outgassed in the load-lock chamber for 1 hour at 200–300°C. During mounting and loading, the substrate surface is again exposed to air and thus recontaminated. Although outgassing procedure can remove a part of these contaminants, especially water, it would be desirable to have a method for further substrate cleaning inside the MBE system. For SiC(0001), Kaplan proposed that Ga polishing can be a good way for removing O related contaminants [71], which was later confirmed by Strite *et al.* [72]. The procedure is to deposit Ga on the surface where it reacts with contaminants to form a volatile compound, e.g., $Ga_2O$. An annealing step up to 750°C can desorb these products and extra Ga remaining on the surface. Analogously, such a Ga treatment was adopted for LAO substrates. However, neither the *in situ* reflection high-energy electron diffraction (RHEED) pattern after this polishing procedure nor the *ex situ* characterization of epifilms shows any improvement.

## 3.3 Polarity

Considering the polar nature of LAO(100), we first investigate the influence of its polarity on the growth of *M*-plane GaN.

**Chemical etching** While we cannot yet provide a microscopic identification of the two polarities, it is at this stage perhaps more important to be able to phenomenologically distinguish them by simple chemical etching. Figure 3.5 shows the surface morphology of either face after a 30 min exposure to HCl(32%) at 60°C, recorded by a Zeiss interference contrast microscope. The most obvious feature in both these micrographs are rhomboidal etch pits which we believe to occur at locations where dislocations in LAO intersect the surface. The elongated side of the etch pits is along [010] direction. Indeed, the distinct linear arrangement of these etch pits was attributed to subgrain boundaries formed by dislocations [73]. More important, however, is the fact that in between these etch pits the surface of face A remains relatively smooth, whereas face B becomes clearly corrugated. Note, however, that a longer treatment or higher temperatures tend to obscure this difference due to the resulting excessive roughening of both faces. Note that the impact of this chemical treatment on LAO is the same for both AE and NP $LiAlO_2$.

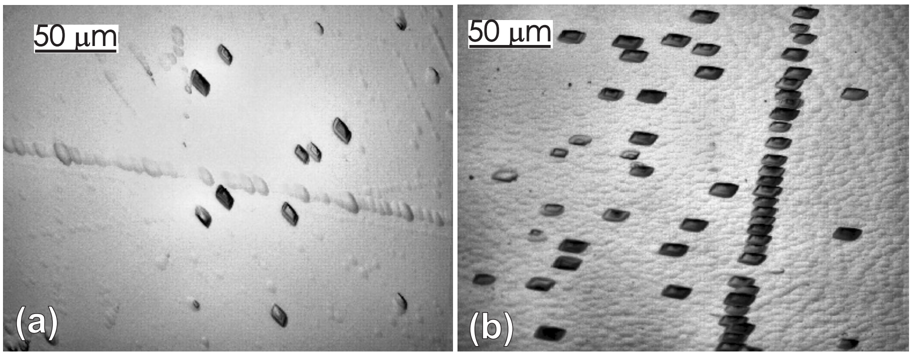

**Figure 3.5:** Interference contrast micrographs of the surface of side A (a) and side B (b) of LAO(100) exposed to HCl(32%) at 60°C for 30 min.

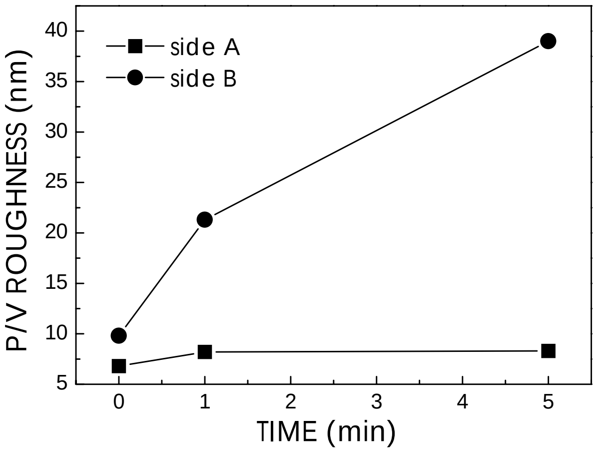

**Figure 3.6:** Peak-to-valley roughness over 10×10 $\mu m^2$ as a function of exposure time to $H_2O$ of two sides of a LAO substrate.

**Hydrolysis** A further means of distinction arises from the vastly different hydrolytic properties of the two faces. Figure 3.6 presents the P/V values of both faces as a function of time when the substrate has been immersed in DI-$H_2O$. Both faces becomes rougher with time, but evidently the reaction of face B is far stronger than that of side A. Note that this roughening is not as readily visible as that discussed above. The increase in roughness after a short time immersion in water is easily measured by AFM, but difficult to distinguish by an optical microscope. Exposure to water for a long time, for example 30 min, makes both sides severely rough, which is even observable under the optical microscope. The transparent substrate even gradually becomes milky for long immersion times. Such a serious reaction with water indicates that care must be taken to limit the exposure of LAO to $H_2O$ during the substrate preparation, which however raises the risk of introducing contamination, e.g. C, into the growth chamber due to residue of organic solvents.

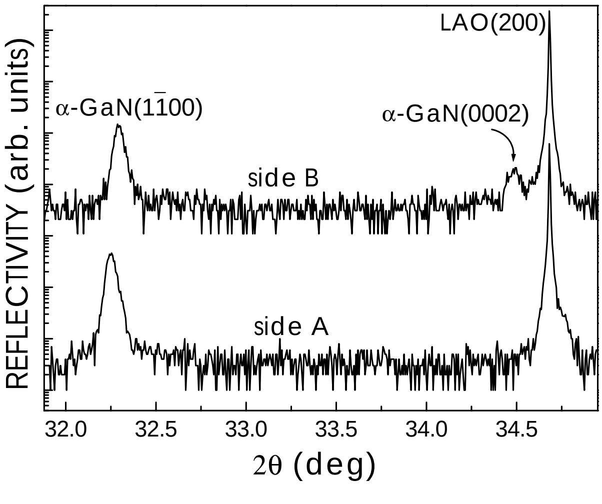

**Figure 3.7:** $\omega$-$2\theta$ triple-crystal scans of two samples grown on two opposite sides but the same conditions.

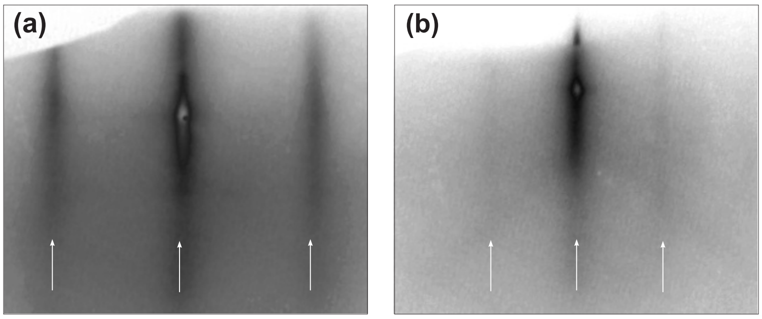

**Figure 3.8:** Typical RHEED patterns of a $\gamma$-LiAlO$_2$(100) substrate, recorded along the [010] (a) and [001] (b) azimuths.

**Epilayer** The influence of polarity of the substrate on the epi-film are checked by growth on two opposite sides of LAO(100) substrate. Figure 3.7 shows triple-crystal $\omega$-$2\theta$ scans for two films grown on each face under the same conditions. In both profiles, the peaks located at $2\theta = 34.682°$ and $\sim 32.254°$ are due to the LAO(200) and GaN($1\bar{1}00$) reflections, respectively. The film grown on face B exhibits an additional weak peak in the left vicinity of the LAO(200) diffraction peak, namely, at 34.5°. Although this angular position coincides with those of either wurtzite GaN(0002) or cubic GaN(111), the RHEED pattern of this sample shows additional reflections stemming from GaN(0001). However, no such peak is detected on the film grown on face A, indicating a high phase purity of this film. In fact, pure *M*-plane GaN epilayers can be reproducibly synthesized on face A if the nucleation conditions are appropriately chosen (see section 4.1). Because of this finding, we will concentrate in the following on layers grown on face A.

## 3.4 Growth on $\gamma$-LiAlO$_2$(100)

**RHEED of $\gamma$-LiAlO$_2$(100)** At room temperature, no RHEED pattern is observed from the substrates due to surface charging, because they are electrically insulating at low temperatures. When the substrate temperature is increased above 400°C, however, a streaky but diffuse ($1\times1$) pattern appears, as seen in Fig. 3.8. Patterns originating from other phases, e.g. $\alpha$-and $\beta$-LiAlO$_2$, are not detected. Furthermore, there is no difference of the RHEED patterns of AE and NP LAO substrates. This is consistent with the results of TOF-SIMS and XPS.

**In-plane orientation relationship** In section 3.3, it is noted that high-resolution $\omega$-$2\theta$ scan can indicate the out-off-plane orientation relationship between the LAO substrate and GaN epilayer. To confirm the expected in-plane azimuthal correlativity as mentioned at beginning of this chapter, selected area electron diffraction (SAD) technique, for example, is presented here. Figure 3.9 (a) and (b) show SAD patterns along GaN [0001] and [$11\bar{2}0$] direction, respectively. Obviously, the GaN film grows epitaxially on the substrate with the expected orientation relationship, i.e., $[0001]_{\mathrm{GaN}}||[010]_{\mathrm{LAO}}$ and $[11\bar{2}0]_{\mathrm{GaN}}||[001]_{\mathrm{LAO}}$. The coincidence of the diffraction spots from the epilayer and substrate in both figures evidences the small lattice mismatch along these two azimuths. In addition, the elongated GaN spots in Fig. 3.9 (b) along the [0001] direction reveal that there are high-density planar defects lying in the basal plane of GaN, which are indeed demonstrated to be stacking faults (see section 5.1).

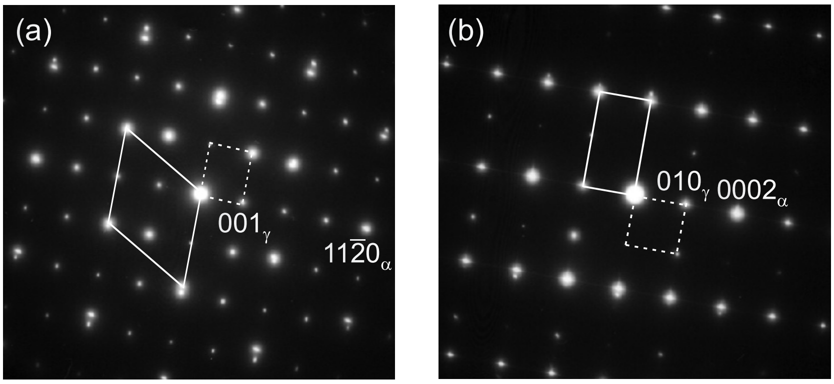

**Figure 3.9:** SAD pattern along $[0001]_{GaN}$ or $[010]_{LAO}$ (a) and $[11\bar{2}0]_{GaN}$ or $[001]_{LAO}$. $\alpha$ and $\gamma$ denote the wurtzite GaN film and the $\gamma$-$LiAlO_2$ substrate, respectively. The unit meshes of the epilayer and the substrate are indicated by the solid and dash lines, respectively.

# 4 Optimization of heteroepitaxy of GaN films on $\gamma$-LiAlO$_2$(100)

Despite the potential advantages mentioned in Chapter 3, LiAlO$_2$ has been rarely used as a substrate for GaN growth. Hellman *et al.* [62] first attempted GaN growth on this substrate, but the films turned out to be [0001]-oriented, instead of the postulate orientation (i.e. [1$\bar{1}$00]). Later, Waltereit *et al.* reported the synthesis of *M*-plane GaN [33], which greatly attracted attention on nonpolar wurtzite group-III nitrides [34, 35, 36,39,44]. However, systematic knowledge of optimizing the growth of these nonpolar GaN epilayers is still lacking. This chapter just focuses on this issue for *M*-plane GaN. First, the impact of nucleation conditions on the structural and morphological qualities of *M*-plane GaN films is investigated. Optimum growth conditions are empirically established. Then a comprehensive study on Ga adsorption and desorption kinetics is presented.

## 4.1 Impact of nucleation conditions on phase purity and structural quality

Nucleation is generally believed to be the most critical step for obtaining high-quality C-plane GaN layers [74, 75, 76]. This is thought to be also applicable for the growth of *M*-plane films.

### 4.1.1 Growth and characterization techniques

**Growth** Growth was carried out in a custom-designed, solid-source three-chamber MBE system equipped with a water-cooled rf plasma source (EPI) to provide atomic nitrogen. The N source is operating at a plasma power of 250–500 W with a N$_2$-flow of 0.3–0.4 sccm, yielding a GaN growth rate of 0.25–0.4 $\mu$m/h. The base pressure in the growth chamber is held below $10^{-10}$ Torr by an ion-getter pump and a Ti-sublimation pump. During growth, the chamber is cryo-pumped and has a pressure around $1.5\times10^{-5}$ Torr for a typical N$_2$ flow of 0.3 sccm. The growth front is monitored *in situ* by reflection high-energy electron diffraction (RHEED) using a 20 kV electron gun. The diffraction pattern is recorded using a CCD camera.

**RHEED** First of all, it should be stressed that MBE offers an excellent tool for determining the phase purity of the layers in real time, namely, by RHEED. During nucleation, a spotty pattern appears which already allows a judgment of the success of the nucleation procedure, since the symmetries of *M*- and *C*-plane GaN are distinctly different. Further growth at Ga-stable conditions yields a streaky RHEED pattern, reflecting the progressive smoothening of the surface. Phase mixture manifests itself in the occurrence of additional reflections (typically spots), which are readily distinguishable from the "clean"*M*-plane pattern as shown in Fig. 4.9 later in this section. In addition, RHEED patterns also can tell the in-plane orientation relationship between epilayer and substrate.

**XRD** Conventionally high-resolution x-ray diffraction (XRD) provides an *ex situ* non-destructive tool to check the relationship of corresponding out-off-plane orientations between the epilayer and the substrate underneath, and simultaneously the phase purity, at least at the angular resolution and detection limit of the diffractometer. Hereafter, the samples' phase purity and the surface orientation are checked by XRD. All symmetric $\omega$ scans (x-ray rocking curve or XRC) were recorded with a Philips double-crystal diffractometer with wide open detector which has an acceptance angle of $\sim 3^o$, while symmetric $\omega$-$2\theta$ scans were taken with a Bede D3 four-circle high-resolution triple-crystal diffractometer with a Si(111) analyzer, having to an angular resolution of 11 arcsec. For thin layers, namely less than 250 nm, instead of the analyzer, two 500 $\mu$m slits were put in front of the detector, with an angular resolution of 300 arcsec, in order to obtain sufficient intensity. Off-axis $\omega$-scans were recorded in skew geometry, where the goniometer is rotated by an appropriate angle $\chi$ such that $\omega = \theta$. Both diffractometers are equipped with a Bartels-type Ge(022) monochromator and utilize Cu K$\alpha_1$ radiation with a wavelength of 0.1540562 nm.

### 4.1.2 Various nucleation conditions

The nucleation regime can be divided into three groups, namely, insertion of an AlN buffer, nitridation prior to growth, and direct deposition. The growth of AlN buffer was initiated at 580°C under different stoichiometry. Then, the growth of GaN was performed under slightly Ga-rich conditions at high temperature. Nitridation was carried out by exposing the substrate to the N plasma at 350 W and 660°C for 40 min. Subsequent nucleation was executed under either N-rich or Ga-rich conditions. The initial stage of direct deposition of GaN (nucleation) was performed at various temperatures and under different stoichiometry. In all cases, the nucleation temperature $T_N$ can be divided into four regimes: high (740°C, actually the growth temperature $T_G$) , intermediate (660°C), low (580°C) and very low (510°C). The thickness of the AlN buffer or the GaN nucleation layers at very low, low and intermediate $T_N$ was

**Table 4.1:** Nucleation conditions for the samples investigated. The table provides information whether nitridation was employed (yes ✓/no −), as well as about the stoichiometry (N-rich/Al- or Ga-rich) and temperature (low/medium/high) during nucleation. We furthermore indicate the phase purity of the layers (M: *M*-plane, C: *C*-plane) as well as the rms roughness obtained by AFM over 5×5 $\mu$m$^2$. All films listed have a thickness of 500–600 nm except for sample I, which is 1.5 $\mu$m thick.

| Sample | AlN buffer | Nitridation | Stoichiometry | $T_N$ (°C) | Phases | rms (nm) |
|---|---|---|---|---|---|---|
| A | ✓ | − | N | 580 | C | ... |
| B | ✓ | − | Al | 580 | C | ... |
| C | − | ✓ | N | 660 | M/C | 80 |
| D | − | ✓ | Ga | 660 | M/C | 15 |
| E | − | − | N | 660 | C/M | 38 |
| F | − | − | Ga | 740 | M | 23 |
| G | − | − | Ga | 660 | M | 7.5 |
| H | − | − | Ga | 580 | M | 2.9 |
| I | − | − | Ga | 580 | M | 1.7 |

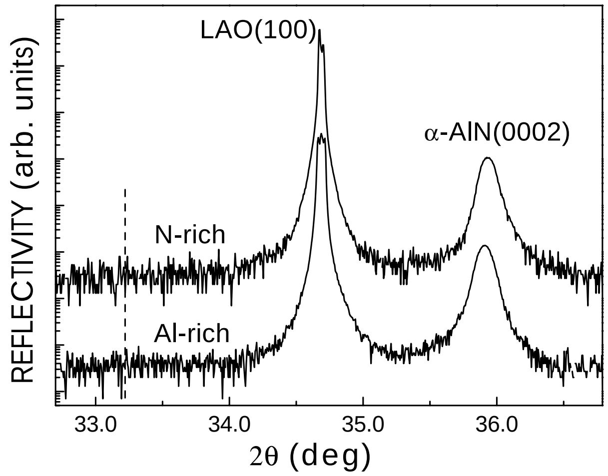

**Figure 4.1:** XRCs of two 200 nm thick AlN layers grown on LAO(100) at 580°C under either Al- or N-rich conditions. The dashed line indicates the potential position for the M-plane AlN.

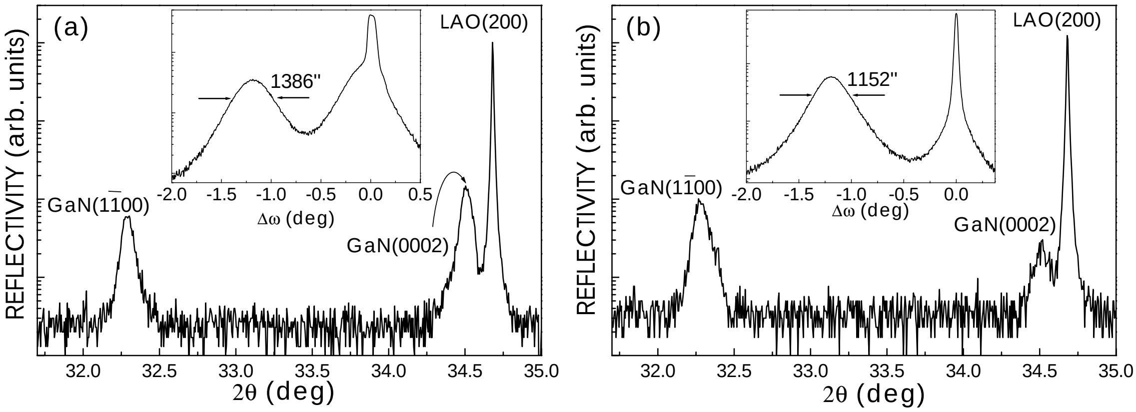

**Figure 4.2:** $\omega$-$2\theta$ triple-crystal scans of sample C along [0001] (a) and [11$\bar{2}$0] (b) directions. The corresponding rocking curves are shown in the respective inset.

about 100 nm. For all samples, the growth temperature $T_G$ of 740°C was kept constant during the subsequent growth and the stoichiometry was set to slightly Ga-rich. For clarity, the typical samples discussed in the following paragraphs are summarized in Table 4.1, including the respective nucleation conditions, phase purities, and surface morphologies.

**AlN buffer** It is occasionally claimed that the use of an AlN nucleation layer has a positive impact on the properties of *C*-plane GaN grown on it [77,78]. Intuitively we first considered whether it also benefits the growth of *M*-plane films. As seen from Tab. 4.1, the samples grown under either Al-rich or N-rich conditions however lead to a predominant *C*-plane structure. To investigate the origin of this effect, one 200 nm thick AlN layer deposited at the same temperature as the buffer used in sample A and B were grown and measured by XRD with two slits in front of the detector. Figure 4.1 clearly shows that the AlN layers are [0001]-oriented, while no peak pertinent to the *M*-plane orientation is detected. AlN nucleation layers (at least with our nucleation conditions) are thus clearly detrimental for the growth of *M*-plane GaN layers.

**Nitridation** Considering that nitridation of $Al_2O_3$ substrates prior to nucleation is well established to improve the crystal quality of the subsequent GaN film by the formation of an AlN template [79,80,81,82], we have studied the nitridation of LAO as a potential means to improve epitaxial growth also in this case.

Figure 4.2 (a) and (b) show the XRD profiles of sample C with the incidence plane parallel to the [0001] and $[11\bar{2}0]$ azimuth, respectively. The profiles exhibit both the *M*- and the *C*-plane reflection, however with different proportions. Considering the line focus of the x-ray beam (a $\sim 2 \times 0.1$ cm$^2$ rectangle oriented perpendicular to the incidence plane), we conclude that the *C*-plane phase is distributed preferentially along the $[11\bar{2}0]$ direction. In fact, scanning electron microscopy of this sample (not shown here) reveals that hexagonal crystallites with diameters ranging from 100 nm to 500 nm accumulate and aligned along $[11\bar{2}0]$. The full-width-at-half-maximum (FWHM) of the corresponding rocking curve as shown in the respective inset are comparable, in contrast to the case shown next. Figure 4.3 shows XRD profiles of sample D along the two orthogonal azimuths. In contrast to sample C, the triple-crystal $\omega$-$2\theta$ scans indicate a more or less isotropic distribution of the *C*-plane phase in this film. However, it is interesting that the FWHM of the rocking curve with the incidence plane along $[11\bar{2}0]$ is more than twice as broad as that perpendicular to it. This anisotropic broadening might result from an anisotropic coherence length, although its actual microstructural origin is not clear yet. It should be noted that $\omega$-scans are insensitive to the phase purity, as this case clearly shows.

**N-rich nucleation** Though N-stable growth has been established to be disadvantageous for the PAMBE growth of *C*-plane GaN epilayers on either $Al_2O_3$ [83], SiC [84], or GaN [85], particularly concerning the surface morphology, it is not clear whether this condition is unfavorable for *M*-plane films too. Figure 4.4 shows a high-resolution $\omega$-$2\theta$ profile as well as a XRC of sample E. Even when considering that the structure factor of the $(1\bar{1}00)$ reflection is about three times smaller than that of the (0001) reflection, these profiles indicate that the film consists predominantly of *C*-plane GaN. The $\omega$-$2\theta$ profile obtained along the $[11\bar{2}0]$ direction is virtually identical and thus not shown here.

Finally, we note that all samples discussed above are quite rough, as can be seen by the

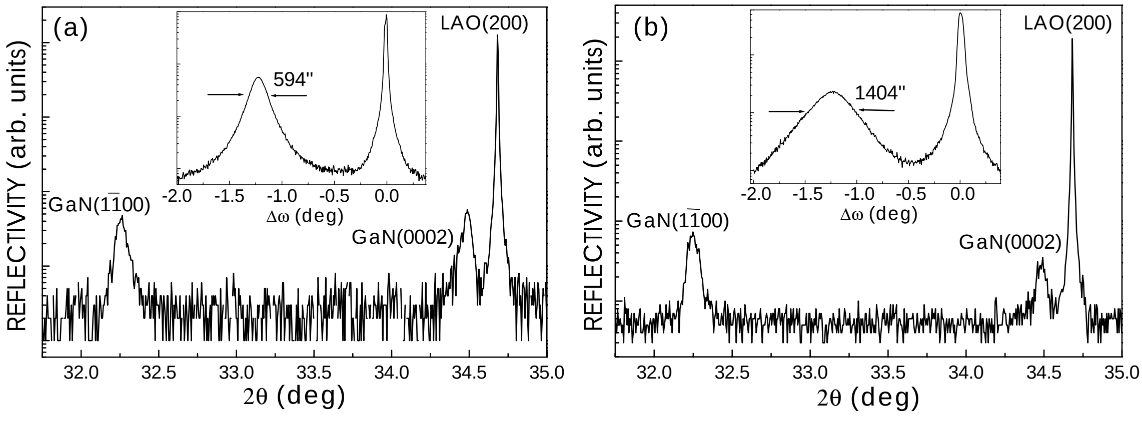

**Figure 4.3:** $\omega$-$2\theta$ triple-crystal scans of sample D along [0001] (a) and $[11\bar{2}0]$ (b) directions. The corresponding rocking curves are shown in the respective inset.

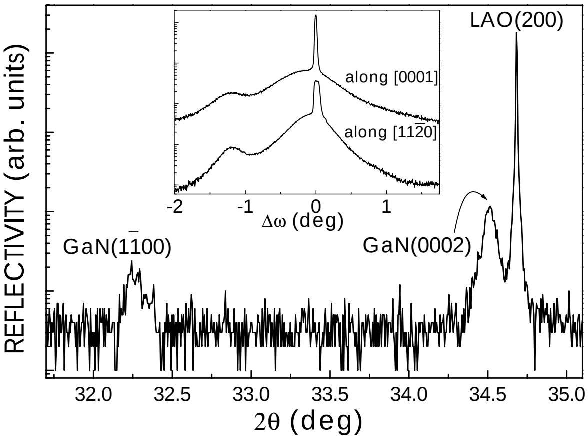

**Figure 4.4:** $\omega$-$2\theta$ triple-crystal scan of sample E along [0001] direction. The rocking curves are shown in the respective inset.

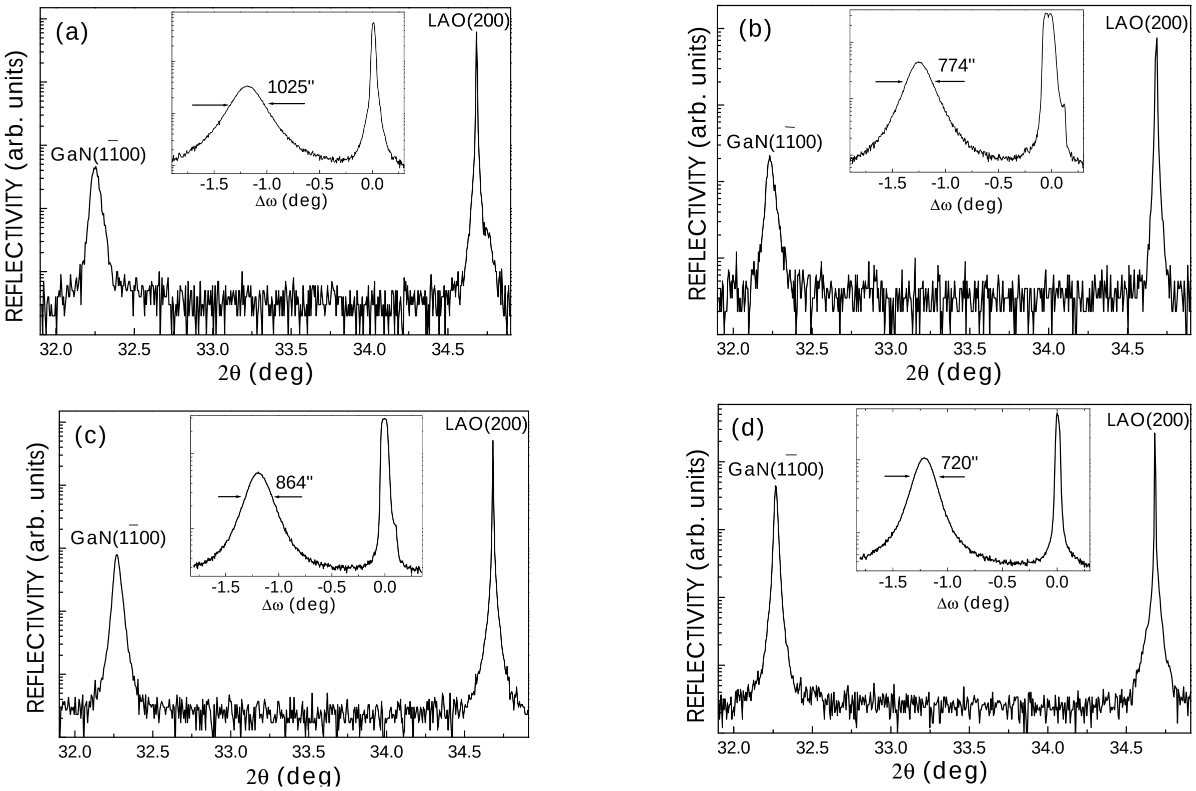

**Figure 4.5:** $\omega$-$2\theta$ triple-crystal scan of sample F (a), sample G (b), sample H (c) and sample I (d) along [11$\bar{2}$0] direction. The insets are their XRCs along the same direction.

values for the rms roughness listed in Tab. 4.1.

**Ga-rich nucleation** Since apparently neither the insertion of an AlN buffer, nor a nitridation step prior to nucleation, nor N-rich nucleation results in satisfactory film qualities, we now turn to immediate nucleation under Ga-stable conditions. We focus on four typical samples, (F, G, H, and I), three of which were nucleated at different temperatures (high, medium, and low, respectively) while sample I was grown under identical conditions as sample H but is thicker (*cf.* Tab. 4.1). Figure 4.5 exhibits the XRD profiles of samples F–I. In contrast to the samples discussed above, none of the present samples exhibits any significant anisotropy in mosaicity or phase purity, for which we show scans along $[11\bar{2}0]$ only. Obviously, all samples are pure *M*-plane films, without any detectable *C*-plane admixture. The mosaicity of the films tends to decrease with decreasing nucleation temperature. This reduction of the linewidth of symmetrical rocking curves is most likely related to a reduced density of structural defects. In fact, the density of stacking faults, which are the dominant structural defects in our *M*-plane layers, reduces dramatically when the nucleation temperature is reduced (see section 5.1). The reduction of mosaicity with the thickness of the layer is apparently not as pronounced, as can be seen from comparing the linewidths obtained for sample H (860 arcsec) with that of its thicker counterpart, sample I (720 arcsec). These values indicate a comparatively high structural quality when compared to the available results reported in the literature. For example, Kuokstis *et al.* [37] recently reported a value of 1200 arcsec for 350-$\mu$m-thick *M*-plane GaN quasi-substrates grown by hydride vapor epitaxy. It should be also noted that the smallest FWHM of the symmetric rocking curve of only 270 arcsec obtained so far is from our Mg-doped *M*-plane GaN nucleated at 580°C (see section 7.1).

It should also be pointed that although the surface morphology of *M*-plane epilayers grown under the same conditions as sample H on the NP LAO substrates are greatly improved, (*cf.* section 4.2) their FWHMs of XRCs range from 750 arcsec to 950 arcsec and do not seem different from its counterpart on the AE LAO substrates. Apparently, the defect densities reflected by the XRC width have no direct correlation with the surface roughness. As we see earlier (*cf.* Fig. 4.1), a direct AlN nucleation leads to [0001]-oriented films on LAO(100). It is interesting to examine the possibility of growth of pure *M*-plane AlN films by the insertion of a low-temperature GaN buffer layer. As an example, one AlN layer is taken into account. First the ~200 nm-thick GaN buffer was deposited with the nucleation temperature of 580°C and under Ga-rich conditions. Then, the 200 nm-thick AlN was grown at 740°C with a rate of 150 nm/h. The *in situ* RHEED pattern indicates that during the whole growth run, the surface is $(1\bar{1}00)$ plane. This finding is confirmed by XRD, as shown in Fig. 4.6. Evidently, *M*-plane GaN buffers allow the realization of *M*-plane AlN films on top.

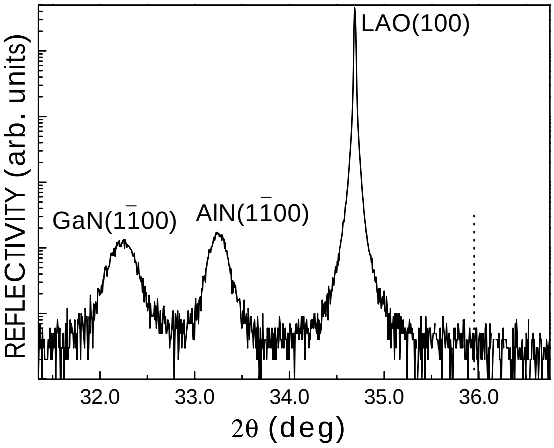

**Figure 4.6:** $\omega$-$2\theta$ scan of a 200 nm thick AlN layer deposited on a 200 nm thick GaN buffer, which is grown on LAO(100). The dotted line indicates the potential position for C-plane AlN.

### 4.1.3 Mosaicity

The broadening of XRC of heteroepitaxial layers grown on lattice mismatched substrates is mainly determined by its mosaicity. The mosaicity is composed of the out-of-plane rotation (tilt), the in-plane rotation (twist), and the lateral ($L_{||}$) and vertical correlation length ($L_\perp$) of the mosaic blocks. In *C*-plane GaN, several studies have been carried out to determine these parameters separately by XRD [86,87,88,89,90]. However, similar work has not yet been performed for GaN with other orientations, such as *M*-plane GaN. A preliminary investigation on this issue is given in the following.

**Williamson-Hall plots** As we see early, the FWHMs of symmetrical XRCs along two orthogonal directions are always different in our *M*-plane films. Usually the scan along the [0001] direction is broader than that along the $[11\bar{2}0]$ direction. The broadening of $\omega$-scans of the symmetrical reflections is influenced by the tilt (out-of-plane mosaic spread) and the finite lateral correlation length ($L_{||}$). These two contributions can be separated by Williamson-Hall plots [91,86]. On the other hand, the broadening of $\omega$-$2\theta$ scans of these reflections is caused by the finite vertical correlation length ($L_\perp$) and the heterogeneous strain along the growth direction ($\varepsilon_\perp$). Figure 4.7 shows Williamson-Hall plots for a *M*-plane GaN with a thickness of 500 nm grown under the same conditions as sample H. Note that the XRD scans are performed with the incidence plane parallel and perpendicular to the *c*-axis. The FWHMs of the $(1\bar{1}00)$ reflection along the [0001] and $[11\bar{2}0]$ directions are 1500 and 1230 arcsec, respectively. Deduced from the slope and *y*-intersection of these plots, the tilt and the lateral correlation length ($L_{||}$) are obtained as 0.382° (0.332°) and 0.28 $\mu$m (3.56 $\mu$m) parallel to (perpendicular to) the [0001] direction, respectively. The analysis of Fig. 4.7 (b) turns out that the vertical lateral correlation length is close to the thickness of the sample and $\varepsilon_\perp$ is about $1.2\times10^{-3}$. It is not surprising that the lateral correlation length along the *c*-axis is much smaller than that perpendicular to the *c*-axis, since a high density of basal plane stack faults are present in this *M*-plane material (*cf.* section 5.1). As no perfect screw dislocation is found from TEM in this material, the large tilt angle (~0.3°) usually found in *M*-plane GaN films must originate from partial dislocations with Burgers vectors having [0001] components.

It is also noted that the anisotropic broadening in sample D (see Fig. 4.3) is unusual, as the XRC perpendicular to the *c*-axis is much broader. Its actual microstructural origin

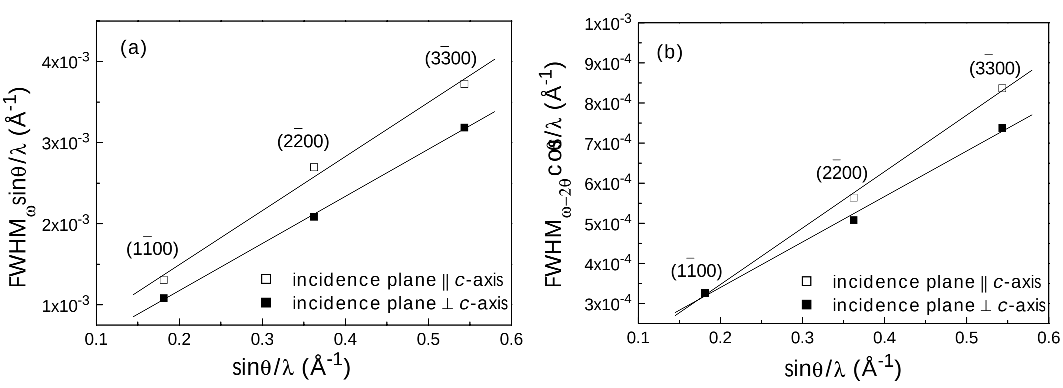

**Figure 4.7:** Williamson-Hall plots of one 500 nm *M*-plane GaN film. The straight lines are linear fitting.

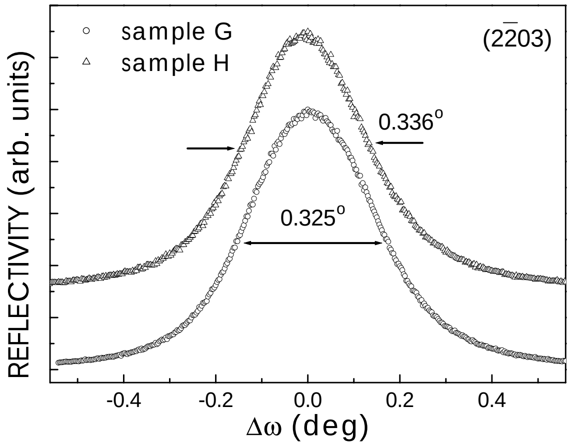

**Figure 4.8:** Rocking curves across the asymmetric $(2\bar{2}03)$ reflection of samples G and H, recorded according a skew geometry.

is unclear at present, but might be related to the distribution of *C*-plane inclusions present in this sample.

**Asymmetric reflection** To obtain a more complete picture of the structural quality of our *M*-plane GaN films, we have also measured rocking curves across the asymmetric $(2\bar{2}03)$ reflection with an inclination angle of 38.614° as shown in Fig. 4.8. This reflection is similar in asymmetry as the commonly used $(10\bar{1}2)$ reflection in the case of *C*-plane GaN and thus has a similar degree of sensitivity to in-plane mosaicity. The value of about 1200 arcsec obtained here suggest that the structural quality of our *M*-plane layers is quite comparable to that of *C*-plane GaN grown by MBE [89]. However, care must be taken when comparing these values. While the relation between the out-of-plane and in-plane orientational spread and threading screw-type and edge-type dislocations, respectively, is well established in *C*-plane films [86], the situation is less clear in *M*-plane films because of their distinctly different microstructure (*cf*. section 5.1).

## 4.2 Influence of nucleation temperatures on surface morphology

**RHEED** Figure 4.9 show the typical RHEED patterns for a 500 nm GaN film grown under the same conditions as sample H. Note that these patterns are recorded after growth of about 300 nm along four different azimuths. Both the angles and the spacings observed agree with those expected for the four major azimuths of the GaN$(1\bar{1}00)$ surface, namely the $[11\bar{2}0]$, $[22\bar{4}3]$, $[11\bar{2}3]$, and [0001] directions shown in Fig. 4.9 (e) [92]. The streaky patterns indicate a smooth surface.

**AFM** The surface morphologies of several *M*-plane GaN films grown under the same conditions as sample H are shown in Fig. 4.10. Both samples H and I are grown on AE LAO substrate, while sample J is grown on NP LAO substrate. Samples H and I exhibit a highly periodic stripe-like pattern, while sample J shows a similar pattern, but without the additional micrometer-scale surface corrugation as found on samples H

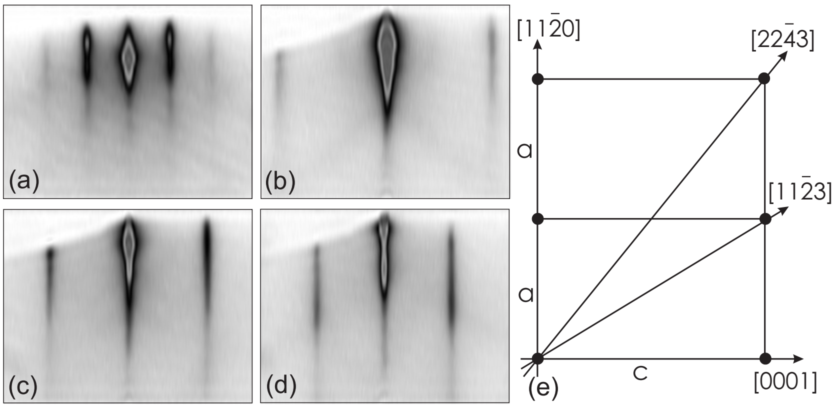

**Figure 4.9:** RHEED patterns of a GaN($1\bar{1}00$) film of 500 nm thickness, recorded along the [$11\bar{2}0$] (a), [$22\bar{4}3$] (b), [$11\bar{2}3$] (c), and [0001] (d) azimuths. (e) shows a sketch of the unit meshes on the ($1\bar{1}00$) surface with the corresponding directions.

and I. The orientation of these stripes, investigated by Raman scattering, is found to be along $\langle 11\bar{2}0\rangle$, i. e., perpendicular to the c-axis. Since the orientation-relationship of *M*-plane GaN and LAO is $[11\bar{2}0]_{GaN}\|[001]_{LAO}$, the micrometer-scale trenches on samples H and I run along the same direction as those observed on the AE LAO substrate (*cf.* Fig. 3.4 (a)). It thus appears that the morphology of GaN films grown on AE LAO basically replicates that of the substrate.

**Roughness vs. T$_N$** The P/V and rms roughness of samples are plotted vs. nucleation temperature in Fig. 4.11. For comparison, two sets of samples grown on either AE or NP LAO substrates are shown. Several conclusions can be drawn from these two plots. (i) Obviously, the impact of T$_N$ on the surface roughness is dramatic. Films grown at low nucleation temperature are significantly smoother than those grown at high nucleation temperature. In both cases, the nucleation temperature at 580°C is apparently the optimum one. In addition, it also should be noted that the samples nucleated at very low temperature, i.e., 510°C, do not show a further improvement concerning the surface morphology, but are rougher than those nucleated at 580°C. Furthermore, the optimum nucleation temperature with regard to the surface morphology turns out to be the same for both AE and NP LAO substrates.

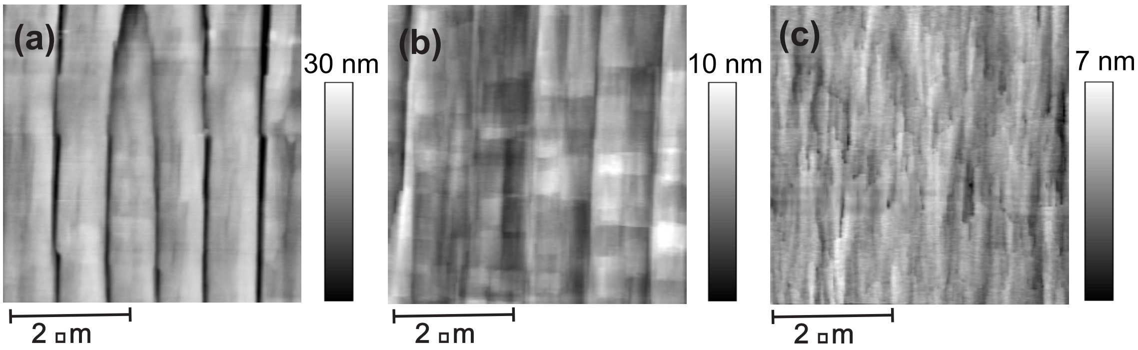

**Figure 4.10:** 5×5 $\mu$m$^2$ AFM micrographs of the surfaces of three typical *M*-plane GaN films nucleated at 580°C: (a) the 600 nm thick sample H and (b) the 1.5 $\mu$m thick sample I are grown on AE LAO, while (c) the 600 nm thick sample J on NP LAO is grown under identical conditions.

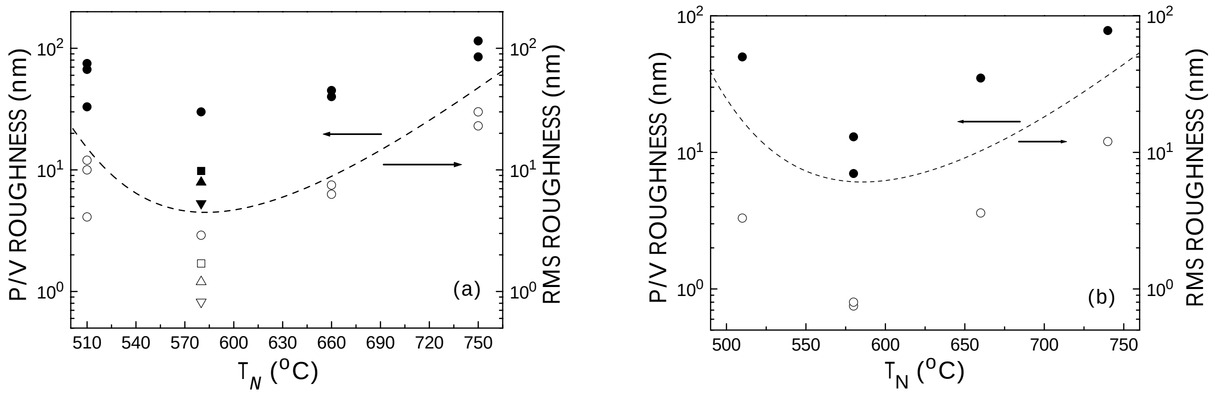

**Figure 4.11:** P/V (solid symbols) and rms (open symbols) roughness over an area of $5 \times 5$ $\mu$m$^2$ as a function of the nucleation temperature. Samples are grown either AE LAO (a) or NP LAO substrates. Circles, squares and triangles represent the films with thicknesses of 500–600 nm, 1.5 $\mu$m, and 1.8 $\mu$m, respectively.

(ii) In general, the samples grown on NP LAO substrates are smoother than their corresponding ones grown on AE LAO substrates. This obviously reflects the difference of these two types of substrates with their different surface morphology.
(iii) The best value grown on AE LAO substrates as seen in Fig. 4.11 (a) is 5 nm and 0.8 nm for the P/V roughnesses and the rms roughnesses, respectively. It should be pointed out that these smoothest samples are 1.8 $\mu$m thick. On the other hand, 600 nm-thick films grown on NP LAO substrates reach a P/V roughness of 6.6 nm and rms roughness of 0.75 nm, which are comparable with the best value as seen in Fig. 4.11 (a). It evidences the significant influence of the substrate's surface morphology on the epilayer surface quality.
Chen *et al.* [38] recently reported an rms roughness of 0.7 nm over $2 \times 2$ $\mu$m$^2$ for a 4-$\mu$m-thick homoepitaxial *M*-plane GaN layer grown by metal-organic vapor phase epitaxy. This compares to 0.6 nm for the best samples in Fig. 4.11 over the same area, demonstrating a virtually identical degree of roughness. As concluded by Chen *et al.* [38], this degree of roughness is close to that obtained on *C*-plane films and is well suited for the growth of heterostructures.

## 4.3 Ga adsorption and desorption kinetics

In the case of GaN(0001), several studies have established the optimum growth conditions in MBE and related them to the existence of a Ga bilayer on the growth front [93,94,95,96,97]. This Ga bilayer is predicted by density-functional calculations to consist of a bottom Ga monolayer (ML) commensurate to the Ga-terminated GaN(0001) surface, and a laterally contracted, incommensurate top Ga ML [94]. This structure was found to be stable under Ga-rich conditions due to the reduced Ga-Ga spacing in the top layer which is predicted to be close to that of bulk Ga. The total amount of Ga contained within this structure is 2.3 ML [1 ML= $1.136 \times 10^{15}$ Ga adatoms cm$^{-2}$ on GaN(0001]. The lateral mobility of the Ga atoms within the bilayer is predicted to be high, consistent with the high morphological quality of GaN(0001) grown under conditions giving rise to bilayer coverage. A direct experimental evidence for the presence of this bilayer is obtained by reflection high-energy electron diffraction (RHEED). GaN layers grown under Ga stable conditions exhibit a dim (1×1) RHEED pattern during growth, but when quenched to temperatures below 300°C, diffuse "sidebands"with a spacing slightly larger than the first order bulk streaks are observed [97]. This spacing corresponds exactly to the theoretically predicted Ga-Ga spacing in the laterally contracted top ML of the Ga bilayer structure.

For GaN($1\bar{1}00$), such a detailed understanding of the surface structure in MBE is lacking. Empirically, we have found that Ga-rich conditions [98, 92] result in GaN($1\bar{1}00$) layers with comparatively smooth surface morphology, whereas N-rich conditions lead to a severe roughening of the growth front. In this study, it has been found that optimum growth conditions (or called standard conditions) for *M*-plane GaN, with regard to the surface smoothness, are Ga-rich nucleation at 580°C, Ga stable growth ($\phi_{Ga} = 0.475$ ML/s, $\phi_N = 0.275$ ML/s) and a substrate temperature of 740°C.

Recently, Lee *et al.* [39] observed a reconstruction of approximate symmetry "(4×5)"on Ga-rich grown GaN($1\bar{1}00$) on ZnO by scanning tunneling microscopy. The surface was found to be metallic in nature, and the authors proposed that it consists of $\geq$2 ML [1 ML= $1.21 \times 10^{15}$ Ga adatoms cm$^{-2}$ on GaN($1\bar{1}00$)] of Ga. This proposal is based on density-functional calculations predicting that Ga-adlayer structures with (1×1) symmetry and coverages between 2 and 3 ML on GaN($1\bar{1}00$) are energetically favorable under Ga-rich conditions [39].

### 4.3.1 Surface reconstruction

In the course of our work, we have noticed that the smoothest layers exhibited a complex RHEED pattern when the surface was quenched to about 150°C with a cooling rate of 40°C/min and the N flux shut off immediately at the termination of growth. The RHEED pattern observed exhibits a fourfold periodicity along all major azimuths

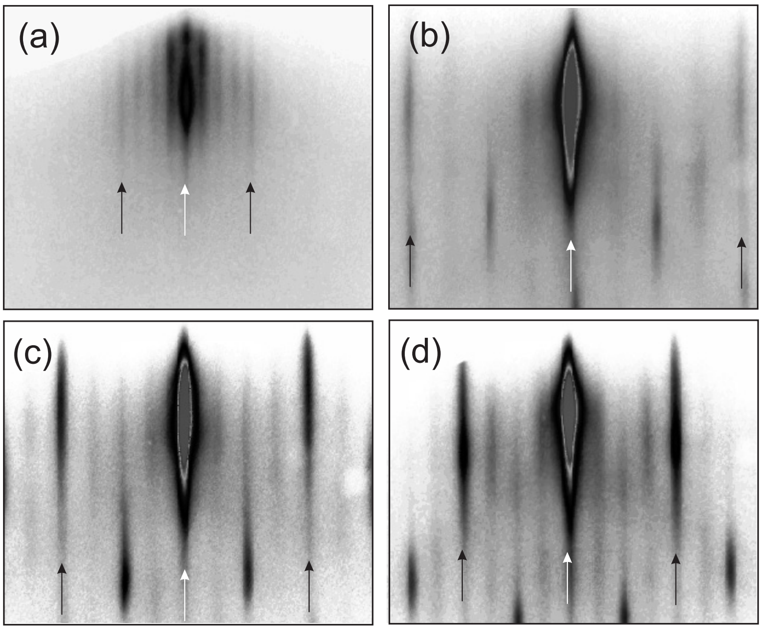

**Figure 4.12:** RHEED patterns of a typical low $T_N$ GaN($1\bar{1}00$) film, recorded at 100 °C along azimuths of [$11\bar{2}0$] (a), [$22\bar{4}3$] (b), [$11\bar{2}3$] (c), and [0001] (d). The arrows denote bulk streaks of zeroth and first order.

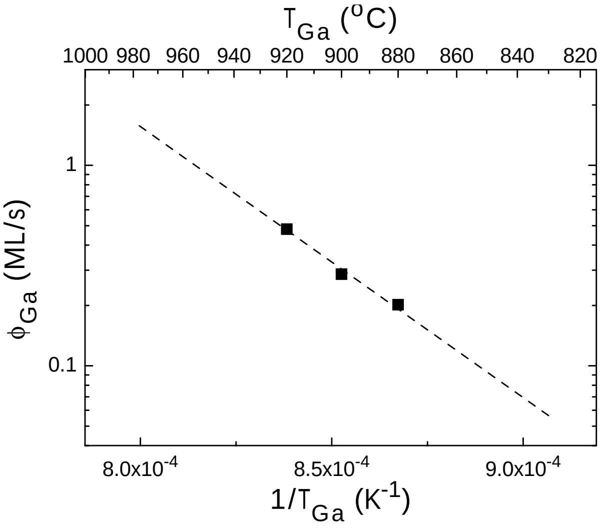

**Figure 4.13:** Ga flux as a function of inverse Ga cell temperatures. The dashed line is the Ga vapor pressure plot with an arbitrary scale.

as seen in Fig. 4.12, consistent with a (4×4) reconstruction with respect to the unit mesh of the GaN($1\bar{1}00$) surface. Note that this reconstruction is not identical to the pseudo-(4×5) reported by Lee *et al.* [39], which gave rise to a fourfold pattern along the [0001] azimuth only. In the following, we establish a relation between the adsorbed Ga coverage and reconstructions of the surface.

**Determination of Ga flux** The Ga flux $\phi_{Ga}$ was determined by the thickness of layers grown under (slightly) N-rich conditions at a temperature of 580°C where Ga desorption can be neglected. This procedure is possible only in a limited range of Ga fluxes (0.2–0.5 ML/s), outside of which it was determined by the vapor pressure of Ga fit to the experimentally obtained values for the absolute flux, as shown in Fig. 4.13. Similarly, an active N flux $\phi_N$ used in this study (a plasma power of 400 W with a $N_2$-flow of 0.3 sccm) was determined to be $0.275 \pm 0.05$ ML/s from the thickness of layers grown under Ga-rich conditions.

**Relation between Ga coverage and surface reconstruction** The growth front was monitored *in situ* by RHEED at 20 kV energy and an incidence angle of 1.5°. The diffraction patterns along all major azimuths of GaN($1\bar{1}00$), i. e., [$11\bar{2}0$] (0°), [$22\bar{4}3$] (≈39°), [$11\bar{2}3$] (≈58°), and [0001] (90°), were recorded using a charge-coupled device (CCD) camera. The intensity of the specular spot and other regions of interest are recorded using a digital RHEED analysis system [99], which was set to sample data at a rate of 25 Hz. Growth was initiated by nucleation at 580°C under Ga-rich conditions. The growth temperature was then raised to 740°C and kept constant during the subsequent adsorption/desorption studies and growth. All of these studies have been done using a 500 nm thick GaN($1\bar{1}00$) layer grown under standard conditions, i. e., Ga stable growth ($\phi_{Ga} = 0.475$ ML/s, $\phi_N = 0.275$ ML/s) and a substrate temperature of 740°C. Figure 4.14 shows the characteristic (1×1) RHEED pattern observed during growth of *M*-plane GaN under standard conditions as given above. The pattern is entirely streaky, but dim, very similar to the RHEED pattern observed during growth of *C*-

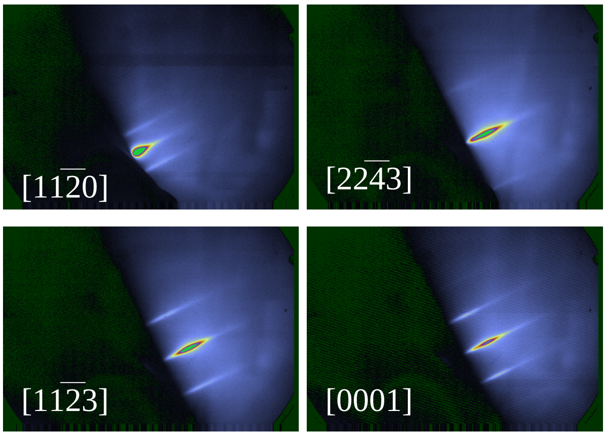

**Figure 4.14:** RHEED patterns of the GaN(1$\bar{1}$00) film, recorded during growth at 740°C along the major azimuths of GaN(1$\bar{1}$00) as indicated.

plane GaN. Upon interrupting the growth for about 20 s at constant temperature and the N flux on, the intensity of the pattern increases greatly, while the (1×1) symmetry does not change. Figure 4.15 shows the RHEED pattern of the *M*-plane GaN film after complete recovery has taken place. We will investigate this recovery behavior in detail in the following sections.

The RHEED pattern of the recovered surface does not exhibit any appreciable change when switching the N flux off. It does not change either when subsequently cooling the sample down to 100°C. Upon deposition of up to 4 ML of Ga on this surface at 100°C, the only noticeable change is that the RHEED pattern becomes dim similar to that observed during growth (*cf.* Fig. 4.14). This finding is in marked contrast to the observation of a (4×4) reconstruction for the surface quenched to low temperature immediately after growth. Apparently, the thermal energy at 100°C is insufficient for the Ga adatoms to condense into this reconstruction.

To study the formation of the (4×4) reconstruction further with this sample, the excess Ga deposited at 100°C is first flashed off by heating the sample to 740°C, leaving a Ga terminated surface that is virtually identical to that observed during growth in-

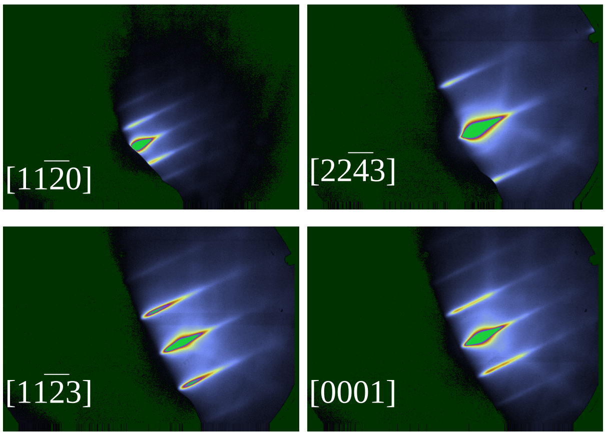

**Figure 4.15:** RHEED patterns of the GaN(1$\bar{1}$00) film, recorded during a growth interruption at 740°C along the major azimuths of GaN(1$\bar{1}$00) as indicated. Note the significantly higher intensity of the bulk streaks compared to Fig. 4.14.

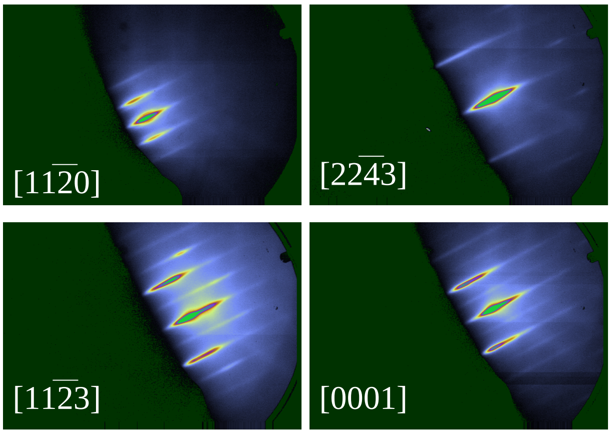

**Figure 4.16:** RHEED patterns of the GaN(1$\bar{1}$00) film, recorded at 100°C after a 2-step deposition of 2 ML Ga at 580°C along the major azimuths of GaN(1$\bar{1}$00) as indicated. Note the intense half-order streaks along all azimuths.

terruptions. The sample is next cooled down to 580°C, at which the desorption of Ga is negligible. Next, we deposit 1 ML of Ga onto this surface. Upon cooling to 100°C, clear half-order streaks are observed along all azimuths except for [11$\bar{2}$0] as shown in Fig. 4.16, consistent with a (1×2) reconstruction of GaN(1$\bar{1}$00). Upon heating, the half-order streaks abruptly disappear at a temperature of 250°C, but the pattern stays dim in comparison to that of the recovered surface. An additional ML of Ga is then deposited at 580°C, which gives rise to a more intense (1×2) reconstruction after cooling to 100°C as shown in Fig. 4.16. However, we often observe the formation of 1/4-order streaks [i. e., next to the (00) streak] along the [11$\bar{2}$0] azimuth at this coverage, which would indicate a (4×2) reconstruction. This observation might indicate a chainlike ordering of (1×2)-reconstructed domains.

The sample is then heated to 580°C again. Finally, the procedure is repeated for the deposition of an additional ML of Ga, resulting in a total of 3 ML of Ga on the surface. Figure 4.17 shows the resulting RHEED pattern, which exhibits an intense (4×4)

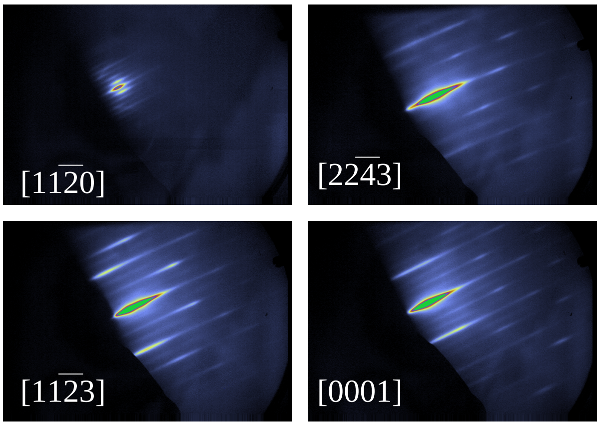

**Figure 4.17:** RHEED patterns of the GaN(1$\bar{1}$00) film, recorded at 100°C after a 3-step deposition of 3 ML Ga at 580°C along the major azimuths of GaN(1$\bar{1}$00) as indicated. Note the intense quarter-order streaks along all azimuths.

reconstruction identical to that observed when quenching the sample after growth under standard conditions.

We have checked that the deposition of 2 and 3 ML of Ga in one step at 580°C results in RHEED patterns which are indistinguishable from those displayed in Figs. 4.16 and 4.17, respectively. Deposition of intermediate amounts, such as 2.5 ML, results in a four-fold periodicity along [11$\bar{2}$0], but a two-fold along all other azimuths, i. e., the (4×2) reconstruction mentioned above. Deposition of larger amounts than 3 ML reduces the overall intensity of the pattern, but does not change its symmetry. In all cases, the quarter-order streaks get diffuse and eventually disappear at temperatures above 250°C.

It is clear from these experiments that Ga adlayers at two stable coverages exist, which condense at low temperatures into a (1×2)/(4×2) reconstruction at bilayer coverage and a (4×4) reconstruction at trilayer coverage. On surfaces with intermediate amounts of adsorbed Ga, both reconstructions may coexist, presumably in the form of domains.

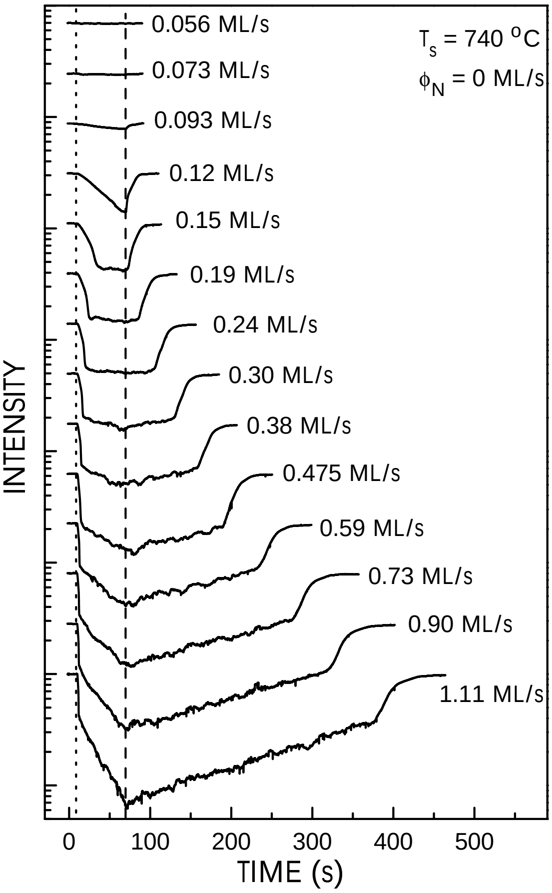

**Figure 4.18:** Variation of the specular RHEED intensity in vacuum (i. e., $\phi_N = 0$) upon adsorption of Ga for 60 s and subsequent desorption for a substrate temperature $T_S$ and Ga fluxes as indicated. The individual transients are vertically shifted for clarity. The dotted line at $t = 10$ s indicates the opening, the dashed line at $t = 70$ s the closing of the Ga shutter.

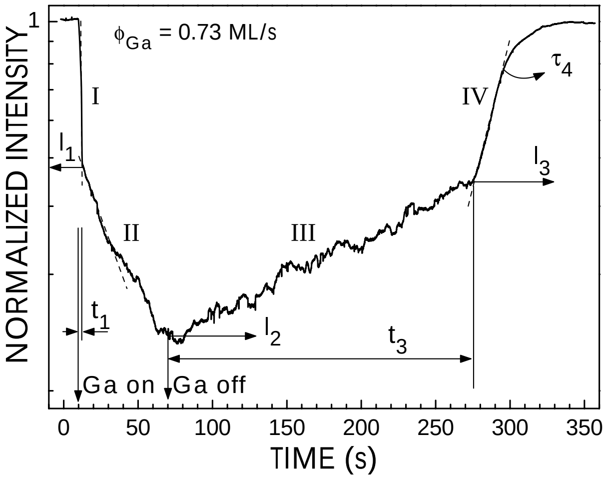

**Figure 4.19:** Definition of the parameters used for analyzing the RHEED transients for the example of $\phi_{Ga} = 0.73$ ML/s. The roman numerals denote the respective stage of the Ga adsorption/desorption process.

### 4.3.2 Ga adsorption/desorption kinetics in vacuum

The recovery behavior of the surface at elevated temperatures provides the opportunity to study the adsorption/desorption kinetics of Ga in real time. For the following experiments, the sample was held at a constant temperature of 740°C. Ga adsorption/desorption isotherms were recorded by monitoring the intensity of the specularly reflected beam along the $[22\bar{4}3]$ azimuth, starting with 60 s of adsorption and allowing the surface to recover completely prior to the next experiment.

Figure 4.18 shows the variation of the specular RHEED intensity $I_s$ for Ga fluxes between 0.056 and 1.11 ML/s. For the two lowest fluxes, no appreciable change in the RHEED intensity is observed, reflecting that Ga desorption at this temperature inhibits the adsorption of significant amounts of Ga on the surface. At higher fluxes (0.12 ML/s), the RHEED intensity exhibits a clear drop once Ga deposition is initiated, and an immediate recovery once the Ga supply is stopped. For $\phi_{Ga} = 0.15$ and 0.19 ML/s, the RHEED intensity stabilizes after the initial drop, and recovers without

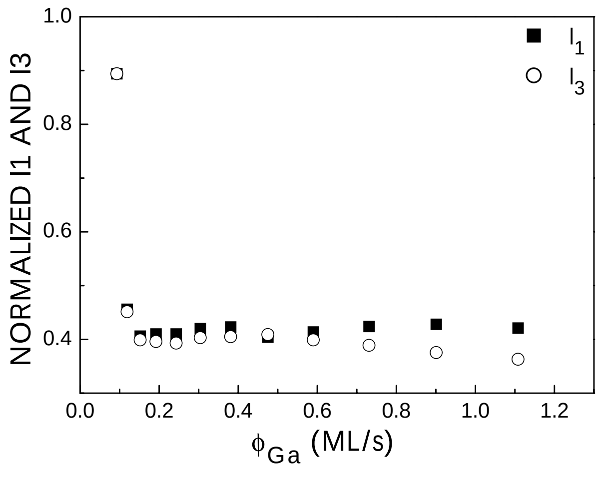

**Figure 4.20:** $I_1$ and $I_3$ vs. Ga flux.

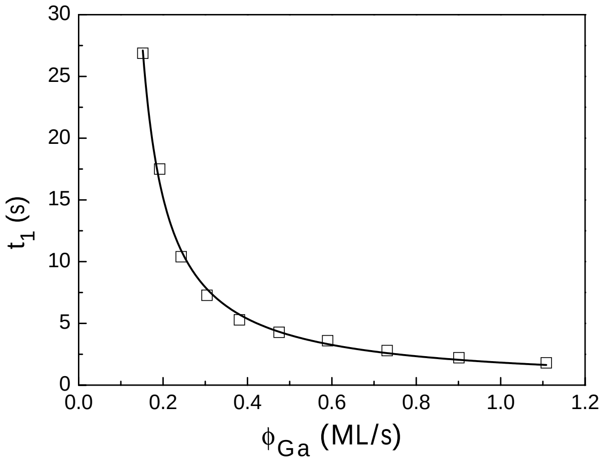

**Figure 4.21:** $t_1$ vs. Ga flux for adsorption in vacuum. The solid line is a fit as discussed in the text.

(0.15 ML/s) or with a very short (0.19 ML/s) delay. Apparently, this situation corresponds to a balance between impinging and desorbing Ga flux, thus establishing an steady-state Ga coverage at the surface independent of deposition time. For a Ga flux higher than this value, the recovery is progressively delayed. Furthermore, the RHEED intensity continues to decrease after the initial, rapid drop, albeit at a much slower rate. We interpret these observations according to the following four-stage scenario. Initially (stage I), Ga adsorbs in a layer-by-layer fashion, resulting in the initial, rapid drop of the RHEED intensity until full coverage is established. If the impinging Ga flux exceeds the desorbing flux, Ga accumulation takes place, eventually leading to the formation of droplets which manifests itself in a further but slower decrease of the RHEED intensity (stage II). Once the Ga supply is stopped, the Ga layer (the exact coverage of which we will attempt to determine below) starts to desorb. Excess Ga, however, acts as reservoir, thus stabilizing the Ga layer and delaying recovery (stage III). Once the excess Ga is depleted, the Ga layer desorbs, accounting for the rapid final recovery (stage IV).
To analyze these Ga isothermal transients quantitatively, we next define parameters

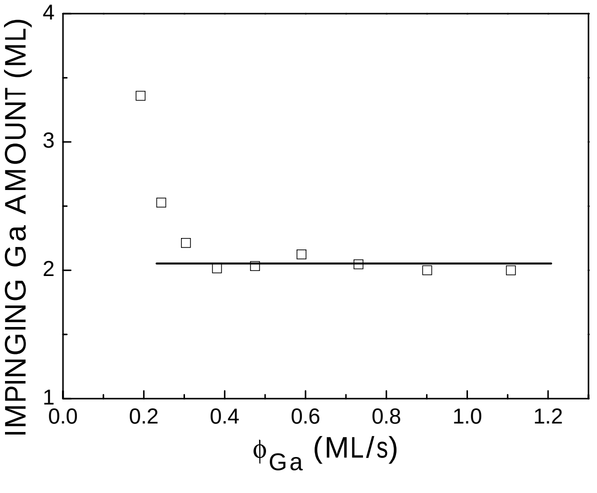

**Figure 4.22:** Amount of impinging Ga during stage I as obtained from $t_1$ vs. Ga flux in vacuum. The solid line is a fit of the data between 0.24 and 1.11 ML/s.

associated with the four stages of Ga adsorption/desorption introduced above. Figure 4.19 visualizes the relation between these parameters to the RHEED transients for the example of $\phi_{Ga} = 0.73$ ML/s. The time interval required for the completion of stage $i$ is denoted by $t_i$, while $I_i$ refers to the intensity at the end of this stage. While the time intervals $t_1 - t_3$ are well defined (note that $t_2 = 60 - t_1$), no such interval can be defined unambiguously for stage IV. In fact, plotting $\ln(1 - I_s)$ reveals the desorption process in this stage to be exponential, thus being characterized by a time constant $\tau_4$ rather than by a time interval. We will analyze stage IV in context with a quantitative description of these transients in section 4.3.4. Figures 4.20 and 4.21 shows the quantities associated with full Ga adlayer coverage, i. e., the intensities $I_1$ and $I_3$ (Fig. 4.20) and the time $t_1$ (Fig. 4.21). Apart from the lowest Ga fluxes used here, where full coverage cannot be reached, $I_1$ is found to be independent of the Ga flux. This finding confirms the view that stage I is related to the adsorption of a fixed amount of Ga. The same applies to $I_3$, which is seen to be identical to $I_1$ within experimental uncertainty. Stage IV thus indeed corresponds to the desorption of a fixed amount of Ga, and this amount seems to be identical to that adsorbed during stage I.

Figure 4.21 depicts the adsorption time interval $t_1$ as function of $\phi_{Ga}$. We see that this quantity exhibits the intuitively expected inverse proportionality to $\phi_{Ga}$. The fit shown by the solid line is based on the simple assumption that the Ga coverage $\theta$ is given by the product of $t_1$ and the Ga flux $\phi_{Ga}$, minus the product of $t_1$ and a mean desorption flux, i. e., $t_1 = \theta/(\phi_{Ga} - \overline{\phi}_{des})$. The good agreement between this expression and the experimentally measured values for $t_1$ confirms that the amount of Ga adsorbed in stage I is indeed constant for a Ga flux resulting in a complete Ga adlayer coverage. Quantitatively, the fit returns values $\theta = 1.62$ ML and $\overline{\phi}_{des} = 0.09$ ML/s. Let us stress that this approach is at best a rough approximation, as it is based on the implicit assumption that both the adsorption and the desorption processes are independent of coverage. We will analyze this situation in section 4.3.4 in more detail. A quantity that can be determined at the present stage without ambiguity is the amount of Ga impinging onto the surface, which is given simply by $t_1\phi_{Ga}$. Figure 4.22 shows the impinging amount of Ga during $t_1$ as a function of the Ga flux. For the lowest fluxes, this amount is vastly overestimated since this analysis neglects desorption altogether.

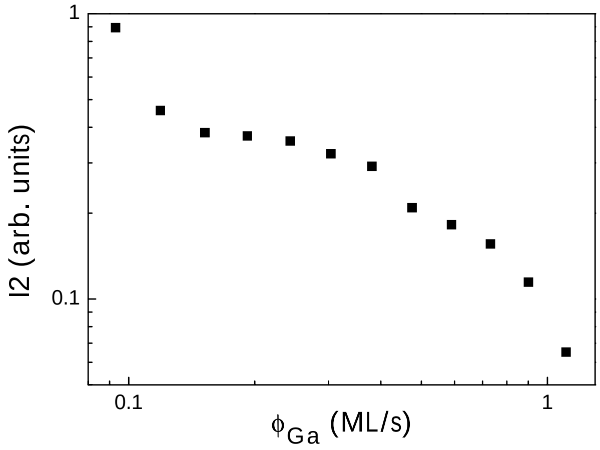

**Figure 4.23:** $I_2$ vs. Ga flux for adsorption in vacuum.

For higher fluxes, the amount is constant as indicated by the solid line and corresponds to 2.04 ± 0.02 ML.

This amount corresponds to 2.04 ± 0.02 ML. As we will show in section 4.3.4, this value closely corresponds to the actually adsorbed amount since Ga desorbing from the adlayer is replaced by excess Ga at these high Ga fluxes. In fact, the above view that excess Ga forms only after completion of the Ga adlayer is overly simplistic, since an infinite diffusion rate of the excess Ga adatoms would be required for this strict separation. The same statement applies to the entire depletion of excess Ga at the onset of stage IV.

A further indication for the formation of a dynamically stable Ga adlayer is provided by the dependence of the intensity $I_2$ on Ga flux, as shown in Fig. 4.23. For a Ga flux between 0.15 and 0.4 ML/s, $I_2$ is found to be almost constant, implying that there is only little, if any, accumulation of excess Ga occurring in this range. Note that one should not expect an entirely constant intensity here, which is often postulated to be a signature of a dynamic equilibrium. For kinetically controlled conditions, an increase of the Ga flux will slightly but inevitably shift the stoichiometry to the more Ga-rich side. However, for higher fluxes, $I_2$ abruptly drops, signifying the formation of significant amounts of excess Ga under these conditions. The precarious balance between adsorption and desorption is thus eventually broken.

The last quantity which is related to full Ga adlayer coverage is the recovery time interval $t_3$. According to our interpretation, this time interval is determined primarily by the desorption of the adlayer coverage, provided that the diffusion rate of excess Ga replenishing the Ga adlayer is sufficiently high. Figure 4.24 shows $t_3$ as a function of the Ga flux. The linear fits shown by the dashed and solid lines are based on the assumption that the excess Ga coverage $n$ built up during stage II is effectively reduced by substitution of the desorbing Ga adlayer coverage in stage III. In other words, $t_3 = n/\phi_{des}^{max}$, where $\phi_{des}^{max}$ is the desorption flux for a full Ga adlayer coverage. Since $n$ accumulates during time $t_2$ where full coverage is already established for Ga fluxes higher than 0.15 ML/s, we may write $n = t_2(\phi_{Ga} - \phi_{des}^{max})$. This simple approximation, which implicitly considers that all excess Ga is available for substituting the Ga adlayer, is shown by the dashed line and returns a maximum desorption flux of 0.16 ML/s. If we take into account that the diffusion rate of excess Ga is not infinite, and that thus

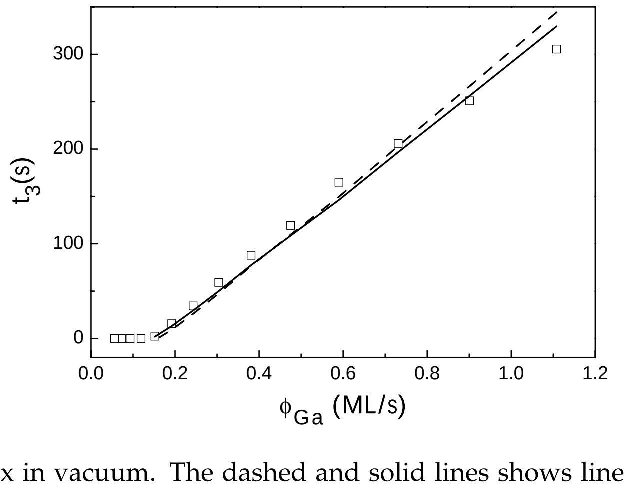

**Figure 4.24:** $t_3$ vs. Ga flux in vacuum. The dashed and solid lines shows linear fits to the data as discussed in the text.

only a certain fraction $a$ of the excess Ga coverage is available for substituting the Ga adlayer, we may express $n$ phenomenologically as $n = at_2(\phi_{Ga} - \phi_{des}^{max})$. The result of this consideration is the solid line, a fraction $a = 0.84$ and a desorption flux of 0.143 ML/s.

To summarize this section, our approximate analysis indicates a stable Ga coverage slightly below 2 ML, above of which excess Ga forms. This analysis, however, neglects the interaction between the Ga adlayer and excess Ga. We will show in section 4.3.4 that the actual coverage is thus close to the amount of Ga actually delivered to the surface during the adsorption interval $t_1$, which turns out to be almost exactly one bilayer (2.04 ± 0.02 ML).

### 4.3.3 Ga adsorption/desorption kinetics under an active N flux

For the following experiments, the sample was held at a constant temperature of 740°C and exposed to an active N-flux of 0.275 ML/s. Ga adsorption/desorption isotherms were recorded exactly as described in section 4.3.2.

Figure 4.25 shows the variation of the specular RHEED intensity for Ga fluxes between 0.19 and 1.66 ML/s. The behavior observed is analogous to that in Fig. 4.18, and we

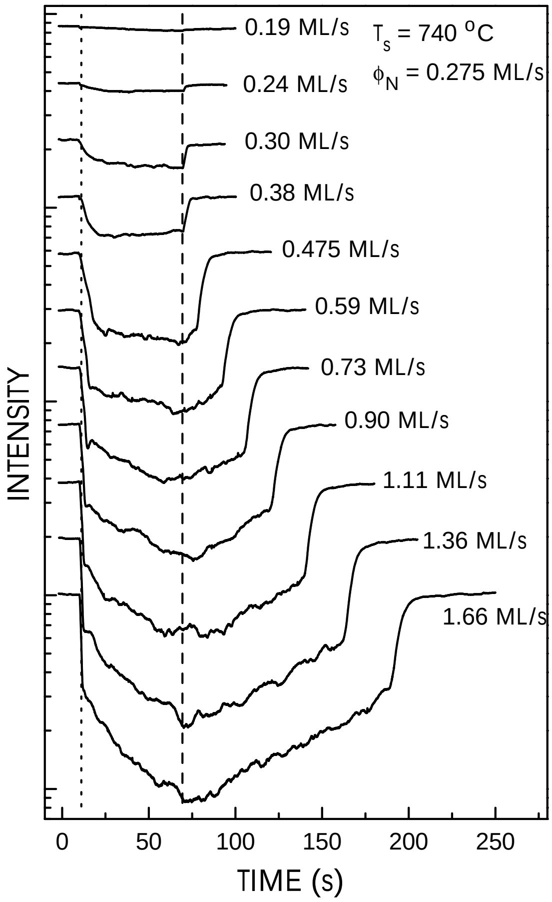

**Figure 4.25:** Variation of the specular RHEED intensity under an active N flux ($\phi_N = 0.275$ ML/s) upon adsorption of Ga for 60 s and subsequent desorption for a substrate temperature $T_S$ and Ga fluxes as indicated. The individual transients are vertically shifted for clarity. The dotted line at $t = 10$ s indicates the opening, the dashed line at $t = 70$ s the closing of the Ga shutter.

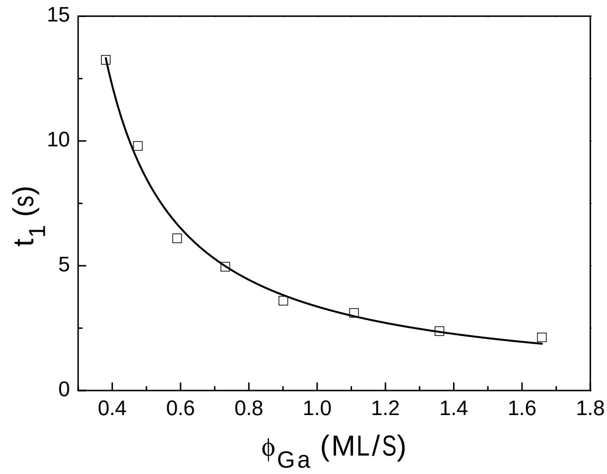

**Figure 4.26:** $t_1$ vs. Ga flux under an active N flux. The solid line shows a fit as dicussed in the text.

thus interpret it in the same way. Particularly, the dependence of $I_1$ and $I_3$ on Ga flux is essentially identical to that shown in Fig. 4.20, and we take this as a confirmation that a stable Ga adlayer coverage is formed also under an active N flux.

The adsorption time $t_1$ is shown in Fig. 4.26 as a function of Ga flux. As in Fig. 4.21, this quantity exhibits an inverse proportionality on $\phi_{Ga}$. The fit shown by the solid line is based on the assumption that $t_1 = \theta/(\phi_{Ga} - \overline{\phi}_{des} - \overline{\phi}_N)$, with the mean consumption flux $\overline{\phi}_N$ due to the presence of active N. Quantitatively, the fit returns values for the Ga coverage of 2.78 ML and $\overline{\phi}_{des} + \overline{\phi}_N = 0.17$ ML/s. The coverage obtained here is significantly higher than that obtained in the vacuum adsorption shown in Fig. 4.21, and the difference is far beyond any possible error margin.

Indeed, when examining the impinging amount of Ga during stage I as shown in Fig.4.27, we find that this amount is as large as 3.45±0.07 ML for Ga fluxes higher than 0.4 ML/s. The active N flux cannot reduce this amount to a bilayer as found for vacuum conditions. We thus believe that these results are significant in that they indicate a stabilization of a larger Ga adlayer coverage by the active N flux compared to vacuum adsorption. It is possible that the two different surface reconstructions, one occurring at bilayer, the other at trilayer coverage, are related to this finding.

Figure 4.28 shows the recovery time $t_3$ as a function of Ga flux. We proceed exactly in the same way as described above in connection with Fig. 4.24, except for the fact that we also consider the consumption flux (equal to the growth rate) due to the presence of active N: $t_3 = n/(\phi_{des}^{max} - \phi_{con}^{max})$, where $n = at_2(\phi_{Ga} - \phi_{des}^{max} - \phi_{con}^{max})$. Interestingly, when explicitly assuming that the diffusion rate of the excess Ga coverage is infinite ($a = 1$), we do not get any acceptable fit (dashed line in Fig. 4.28). Considering, as above, that only a fraction $a$ of the excess Ga is able to replenish the Ga adlayer, we obtain the solid line, $a = 0.59$, and $\phi_{des}^{max} + \phi_{con}^{max} = 0.365$ ML/s. Given that the N flux has been determined to be 0.275 ML/s, the latter result indicates a desorption flux at full adlayer coverage of 0.09 ML/s, considerably less than in vacuum.

### 4.3.4 Kinetic model

We have seen in the preceding sections that the strict distinction between the formation of a Ga adlayer and the subsequent accumulation of excess Ga is too simplistic. The most important questions we must ask are thus, if the four-stage scenario developed in section 4.3.2 is essentially correct, and how accurate the approximate analyses presented above actually are.

To answer this question, we next develop a quantitative model of our interpretation. The model is required to account for adsorption and desorption of Ga as well as for the formation of excess Ga interacting with the Ga adlayer, and for GaN growth in the case of the simultaneous presence of Ga and N. Our model, in units normalized to the maximum Ga adlayer coverage, is described by the equations

$$\frac{d\theta}{dt} = j_{Ga}(1-\theta) + d_{Ga}(1-\theta)n - \gamma_\theta\theta - j_{N_2}\theta \quad (4.1)$$

$$\frac{dn}{dt} = j_{Ga}\theta - d_{Ga}(1-\theta)n - \gamma_n n \quad (4.2)$$

where $\theta$ denotes the Ga adlayer coverage, $n$ the amount of excess Ga, $j_{Ga}$ and $j_N$ the Ga and N delivery rate, $d_{Ga}$ the diffusion rate of excess Ga adatoms impinging onto $\theta$, and $\gamma_\theta$ ($\gamma_n$) the rates of Ga adlayer (excess Ga) desorption. The first term of each equation accounts for adsorption of Ga, building up the Ga adlayer $\theta$ and subsequently excess Ga $n$. In much the same way, the second terms account for diffusion of excess Ga impinging onto the Ga adlayer. The third terms describe the desorption of the $\theta$ and $n$. The last term in Eqs. (4.1), finally, stands for the incorporation of Ga and N adatoms into the crystal, i. e., actual growth. Note that the model described by Eqs. (4.1) and (4.2) is a linearized, and highly simplified version of microscopic theories of the surface kinetics such as developed in Ref. [100]. This simplification is necessary to reduce the number of free parameters and thus to guarantee stable fits, but also means that, while our model is perhaps the most simple one accounting for the phenomena we wish to describe, there certainly are a variety of more refined models which could equally well describe the data.

Finally, we have to relate the surface coverage calculated by means of Eqs. (4.1) and

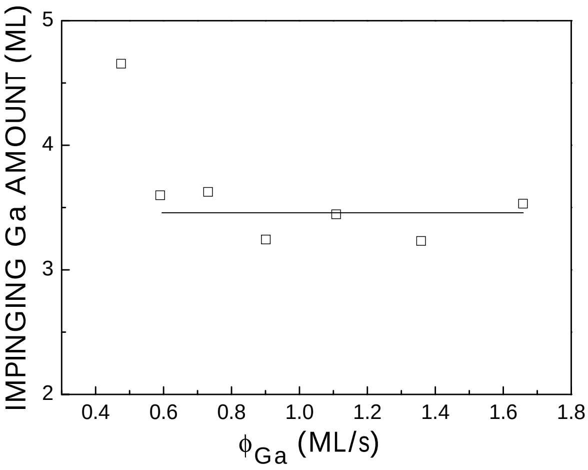

**Figure 4.27:** Amount of impinging Ga during stage I as obtained from $t_1$ vs. Ga flux under an active N flux. The solid line is a fit of the data between 0.59 and 1.66 ML/s.

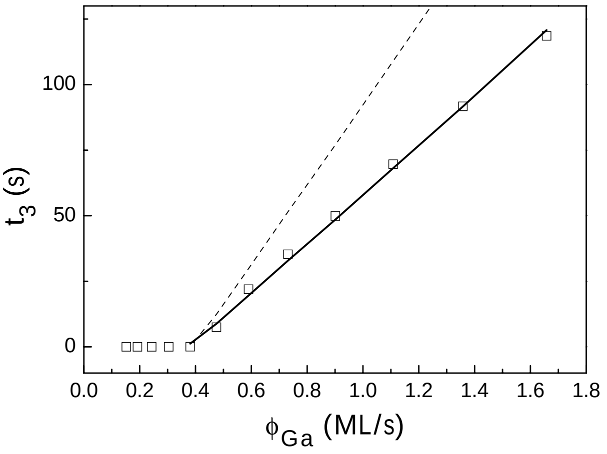

**Figure 4.28:** $t_3$ vs. Ga flux under an active N flux. The dashed and solid lines show a linear fits to the data as discussed in the text.

(4.2) to the quantity experimentally observed, namely, the RHEED intensity. Since the Ga adlayer at growth temperature does not condense into a reconstruction, but rather represents a liquid, it manifests itself in a damping of the RHEED intensity. We thus follow the well-established relation between surface coverage and intensity in Auger attenuation experiments [101], which reads:

$$I(\theta, n) = e^{-\theta - bn}. \tag{4.3}$$

Both the adlayer coverage $\theta$ and the excess coverage $n$ are assumed to damp the intensity exponentially. The ripening of excess Ga to clusters and droplets leads to a (geometrically determined) different rate of decrease with respect to the Ga adlayer coverage, as expressed by the prefactor *b*. Figure 4.29 shows three experimental Ga adsorption/desorption isotherms in vacuum together with simulations based on Eqs. (4.1)–(4.3). Except for the Ga flux, which was taken to be equal to the experimentally de-

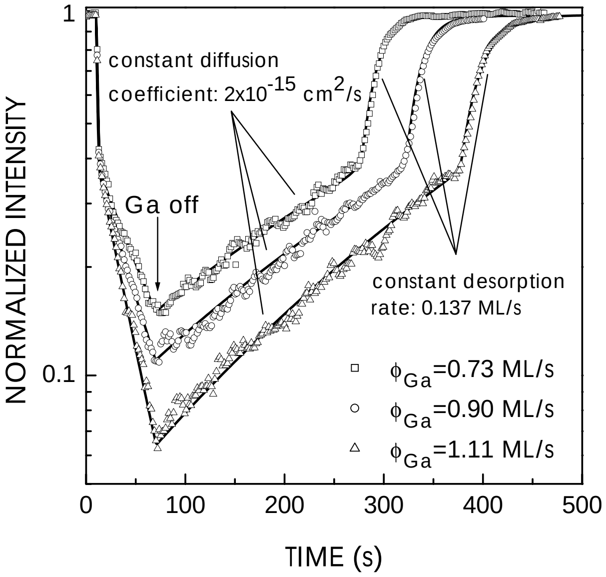

**Figure 4.29:** Experimental (symbols) and simulated (solid lines) RHEED transients for three different Ga fluxes as indicated in the figure.

termined flux as indicated in the figure, we used the same parameters for these simulations, namely: a diffusion coefficient of $2\times10^{-15}$ cm$^2$/s, a Ga adlayer desorption flux of 0.137 ML/s, an excess Ga desorption flux of 0.003 ML/s, and a prefactor $b$ of $0.06\pm0.003$. Evidently, the agreement between the experimental transients and the simulations is very good. Most importantly, this agreement can only be obtained with the above set of parameters, since the slope of the transient in stage III is mainly determined by $\gamma_n$, while $\gamma_\theta$ determines the slope of the transient in stage IV. Furthermore, the onset of stage IV depends essentially on the sum of $\gamma_n$ and $\gamma_\theta$, resulting in unique fits to the experimental data. This result reflects that our general understanding of the adsorption/desorption processes is essentially correct. Of particular interest at this point are thus the Ga adlayer and excess Ga coverages predicted by the simulation at the intensities $I_1$ and $I_3$. At $I_1$, these coverages are found to be independent of Ga flux for $\phi_{Ga} \geq 0.15$ ML/s, and amount to $\theta = 1.64$ ML and $n = 0.42$ ML, respectively. At $I_3$, we obtain $\theta = 1.86$ ML and $n = 0.34$ ML, again independent of Ga flux for $\phi_{Ga} \geq 0.15$ ML/s. The coexistence of $\theta$ and $n$ is a direct result of the finite diffusion rate of the excess Ga, as already concluded above.

An interesting detail is the inability of our model to accurately fit stage I and the transition towards stage II, as shown for a Ga flux of 0.9 ML/s in Fig. 4.30. The experimental transients exhibit two clearly distinct slopes during stage I, an abrupt change of slope at the transition to stage II, and a gradual change of slope thereafter. It is likely that this complex behavior reflects the formation of the bilayer by the subsequent adsorption of a lower and upper ML, accompanied by the simultaneous nucleation and diffusion of excess Ga on both of these levels. Our model as formulated above is obviously unable to reproduce this process, since it does not distinguish the two distinct layers of the Ga bilayer but treats them as being one entity. However, there are other factors which must be considered as well in this context. If the Ga adlayer is not completed ($\theta < 1$), it does not form a continuous film but two-dimensional islands. This inevitable fact has several important consequences. First of all, our model treats $\theta$ as a continuous variable, and neglects its inherently discrete nature at low coverages. Second, the desorption kinetics of two-dimensional islands is known to be dominated by desorption from the islands' edges, which changes the first-order (monomolecular) desorption kinetics as-

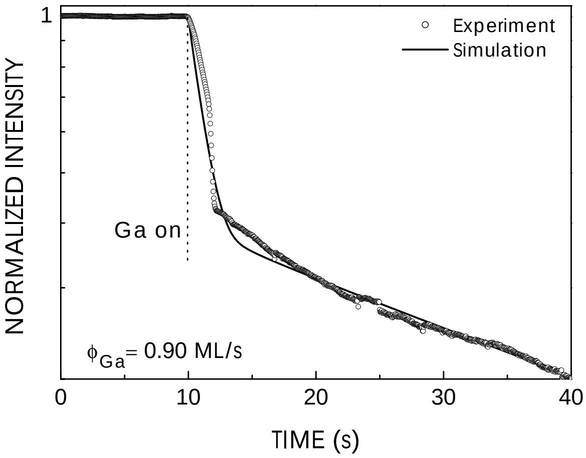

**Figure 4.30:** Experimental (symbols) and simulated (solid lines) RHEED transient for the indicated Ga flux during the initial adsorption stage.

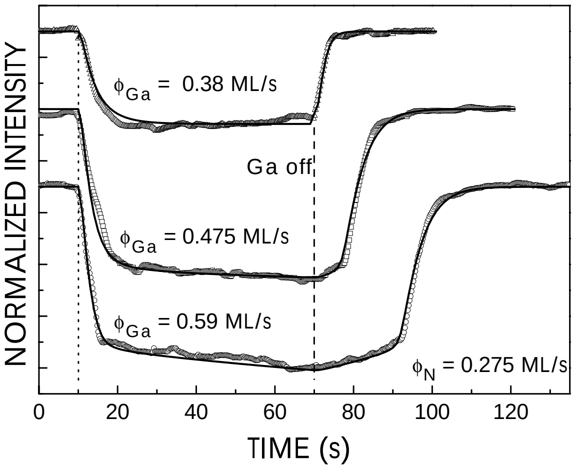

**Figure 4.31:** Experimental (symbols) and simulated (solid lines) RHEED transients for three different Ga fluxes as indicated in the figure and an active N flux of 0.275 ML/s. The transients are vertically offset for clarity. The Ga opening and closing are indicated by dotted and dashed lines, respectively.

sumed here ($\propto \theta$) to half-order ($\propto \sqrt{\theta}$). Third, the desorption rate $\gamma_\theta$ will be enhanced in this case, essentially resulting in a coverage-dependent desorption rate which is no longer a constant but a function of $\theta$. In fact, for Ga fluxes lower than 0.19 ML/s, we had to increase $\gamma_\theta$ significantly to account for the early and comparatively rapid recovery observed. In view of that said above, it is clear that this simple measure is purely phenomenological and only approximates the actual desorption process.

We next turn to a comparison between experimental Ga adsorption/desorption isotherms under active N flux and simulations based on Eqs. (4.1)–(4.3). As above, we take the experimentally determined Ga flux for the simulations, and, of course, the additional N flux. For a Ga flux larger than 0.475 ML/s, the parameters required to get a good agreement between simulated and experimental transient are identical to those given above, except for $\gamma_\theta$, which turns out to be slightly larger (0.155 ML/s). For lower Ga fluxes, the Ga adlayer is not completed and $\gamma_\theta$ increases drastically as discussed above for the case of desorption in vacuum. Figure 4.31 shows the three RHEED transients at the transition between N-stable and Ga-stable conditions. The desorption fluxes required to fit them are 0.155, 0.21, and 0.28 ML/s from low to high Ga flux. The good agreement between experimental and simulated transients shows that the adsorption/desorption kinetics is not fundamentally different in the presence of a N flux compared to that under vacuum. Rather, the N flux seems merely to consume Ga and thus to shift the adsorption/desorption balance toward higher Ga fluxes. For sake of completeness, we determine again the Ga adlayer and excess Ga coverages predicted by the simulation at $I_1$ and $I_3$. At $I_1$, these coverages are found to be independent of Ga flux for $\phi_{Ga} \geq 0.475$ ML/s, and amount to $\theta = 1.94$ ML and $n = 0.88$ ML, respectively. At $I_3$, we obtain $\theta = 1.88$ ML and $n = 0.26$ ML, again independent of Ga flux for $\phi_{Ga} \geq 0.475$ ML/s. The large coverage at $I_1$ is consistent with that deduced from Fig. 4.26. At this point, it is instructive to examine the predictions of our model for prolonged growth using the parameters used for the simulations in Fig. 4.31. Figure 4.32 (a) shows the Ga bilayer coverage vs. growth time for the three different Ga fluxes at the transition between N-stable and Ga-stable conditions. As expected, full bilayer coverage is not reached for the lowest Ga flux. In contrast, the Ga adlayer coverage slowly converges towards a full bilayer for the intermediate Ga flux, and is obtained rapidly for the highest Ga flux. However, as shown in Fig. 4.32 (b), the price one pays for this rapid bilayer completion is a diverging Ga excess coverage, which increases without bound for prolonged growth. In fact, layers grown under these conditions exhibit a high density of Ga droplets and, after HCl etching, of corresponding surface defects. In contrast, the Ga excess coverage saturates at 2 ML for the intermediate Ga flux, reflecting that a dynamic equilibrium is established under these conditions. Note that the desorption flux for this case is 0.21 ML/s, which in fact is almost exactly equal to the difference of Ga and N flux. The total Ga coverage during growth is here thus 4 ML, which is consistent with the observation of the Ga-trilayer related $(4 \times 4)$-reconstruction observed for this growth conditions after quenching the sample to 100°C (*cf.* Fig. 4.17). For the lowest Ga flux, the excess coverage is (as expected) negligible.

In agreement with this prediction, our GaN$(1\bar{1}00)$ layers grown under standard conditions exhibit droplet-free and microscopically smooth surfaces, as shown in Fig. 4.10 (c). The surfaces of the layers exhibit the characteristic highly anisotropic, stripe-like morphology of GaN$(1\bar{1}00)$ layers [92, 38, 39]. With a rms roughness of 0.6 nm, the smoothness of those layers approaches (but does not yet reach) that of state-of-the-art GaN(0001) layers grown by PAMBE.

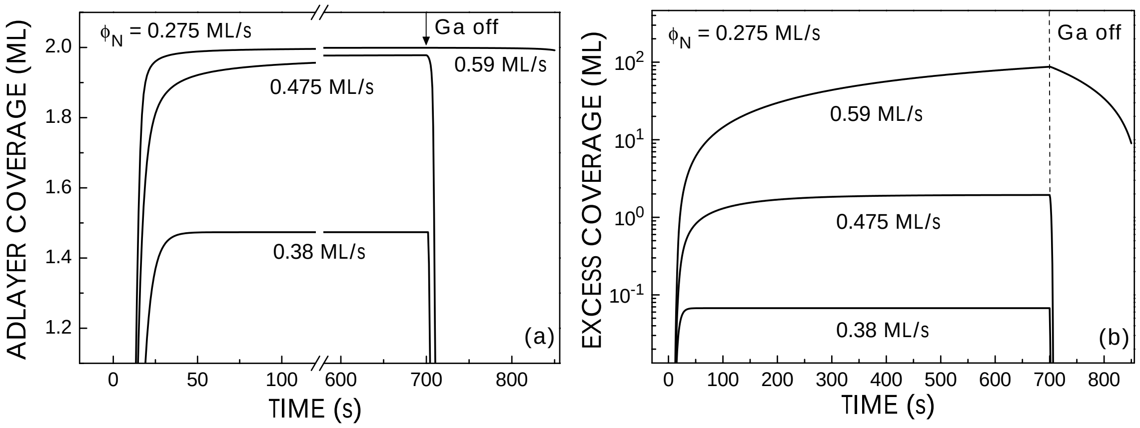

**Figure 4.32:** Simulated Ga adlayer and excess Ga coverage during growth. The parameters used are those deduced from the simulations shown in Fig. 4.31, but the Ga supply is now terminated at $t = 700$ s.

# 5 Structural and optical properties of *M*-plane GaN

In this chapter, the correlation of the structural and optical properties of pure *M*-plane films is discussed. We focus on two samples, namely, sample F and sample G2 nucleated at 750°C and 660°C (growth details can be found in section 4.1). AFM, transmission electron microscopy (TEM), cw-photoluminescence (PL), time-resolved (TR) PL, cathodoluminescence (CL) and scanning electron microscopy (SEM) have been used to characterize these samples.

## 5.1 Structural and optical properties

**High-resolution XRD** To examine the phase composition of sample G2, we utilize high-resolution x-ray diffractometry. Figure 5.1 presents $\omega$-$2\theta$ scans of both samples. The peaks located at 34.682° and 32.254° are due to the (200) and $(1\bar{1}00)$ reflections of LAO and GaN, respectively. No peak related to the (0002) *C*-phase is detected, which, if present, should be seen in the left vicinity of the LAO(200) diffraction peak, namely, at $2\theta = 34.56°$ (*cf.* Fig. 3.7). The values of the angular separation between these two peaks indicate a lattice expansion of 0.63% and 0.70% along the growth direction $[1\bar{1}00]$ for samples F and G2, respectively. This expansion is a consequence of the thermal and/or the lattice mismatch between GaN and LAO, both of which result in compressive in-plane strain. XRD rocking curves taken from these two samples exhibit a width of 1020″ for sample F and 774″ for sample G2. As we will see below, the reduced broadening for sample G2 is in fact related to a reduced density of structural defects, though the actual difference between samples F and G2 is more dramatic than reflected by the rocking curves.

**PL at 5 K** Figure 5.2 shows the PL spectra of samples F and G2 at 5 K. The PL spectra of both samples are dominated by strong near-band-gap transitions. Yellow luminescence (YL) is undetectable for both samples. The high energy bands near 3.48 eV for both samples are attributed to the donor bound exciton $(D^0,X)$. The blue-shift of

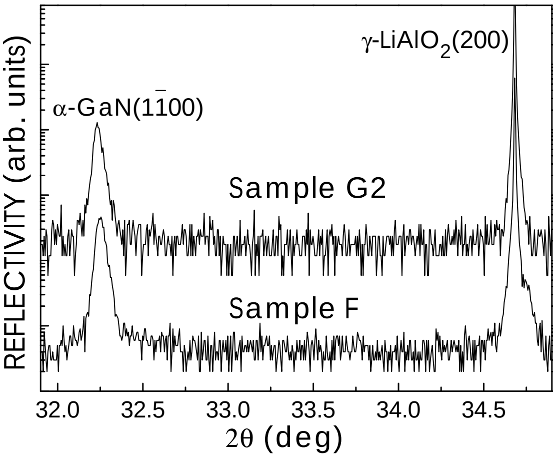

**Figure 5.1:** $\omega$-$2\theta$ triple crystal scans across the $(1\bar{1}00)$ GaN-reflection of samples A and B.

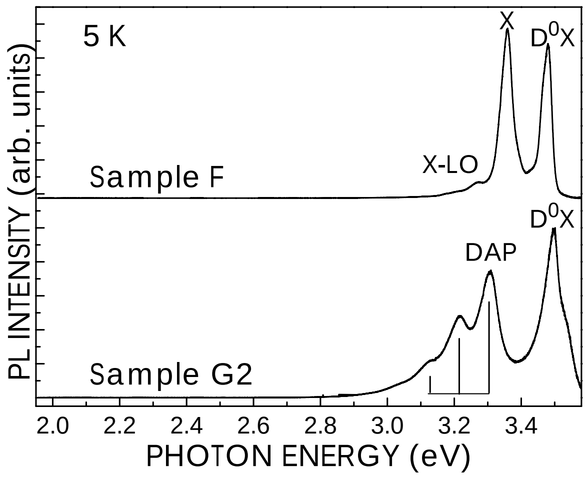

**Figure 5.2:** Photoluminescence spectra of sample F and sample G2 recorded at 5 K. The equidistant phonon replicas are indicated by vertical lines.

the ($D^0$,X) transition compared to relaxed GaN [102, 103] evidences the comparatively large compressive stress of the layers, consistent with the XRD results. In addition to the ($D^0$,X) transitions, the spectra of both samples exhibit a lower-energy line at 3.356 eV (X) for sample F and at 3.30 eV for sample G2. Considering the large compressive strain in these layers, at least the latter of these lines is suspiciously close to the position of the donor-to-acceptor pair (DAP) transition [104, 105, 106]. Regarding the former line, several groups have reported a weak PL line around 3.36 eV at low temperatures from *C*-plane GaN samples grown by different techniques and on different substrates [107, 108, 109, 110, 111, 112, 113], and have mostly attributed this transition to excitons bound to structural defects, such as stacking faults [111] or dislocations [108, 109, 110]. In the following, we investigate the origin of the low-energy lines from samples F and G2 in detail. As mentioned in section 3.2 and also shown in section 4.2, the two types of LAO substrates, i. e. AE and NP, have significant impact on the surface morphology of samples grown on the top. However, all other physi-

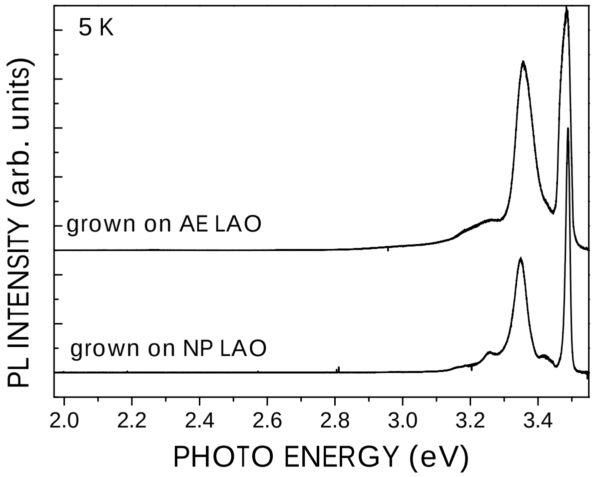

**Figure 5.3:** 5 K photoluminescence spectra of two samples grown on AE and NP LAO substrate respectively.

cal properties, such as the micro-structures (which will be discussed later) and optical transitions, remain basically unchanged. Figure 5.3 shows a comparison of the PL spectra of two samples both grown under the same conditions as sample H, but on AE and NP LAO substrates. Both samples exhibit the same fundamental transitions, namely, a dominant ($D^0$,X) transition and a lower energy line similar to that observed in sample F, the origin of which will be discussed in the following.

**SEM and CL map** Since we expect a transition related to structural defects to exhibit a larger degree of spatial inhomogeneity than a transition arising from point defects, we first perform spatially resolved CL measurements. CL measurements are performed at 5 K in a scanning electron microscope equipped with an Oxford mono-CL2 and He-cooling stage. Surface micrographs are obtained by the same SEM at room temperature.

Figure 5.4 (a) shows a plan-view SEM image of sample F at room temperature. We observe the typical stripe-like pattern characteristic for GaN grown on AE LAO(100), consisting of rather smooth ridges and rough trenches. The CL map at the wavelength of the X line is shown in Fig. 5.4 (b). The emission indeed preferentially occurs along the stripe direction. The superposition of the SEM and CL map (not shown here) demonstrates that the X line predominantly originates from the trench regions. For comparison, we show SEM and CL maps of sample G2 in Fig. 5.4 (c) and (d), respectively. Evidently, the DAP emission from sample G2 is significantly more uniform compared to the X emission from sample F shown in Fig. 5.4 (b). Still, it is not entirely uniform,

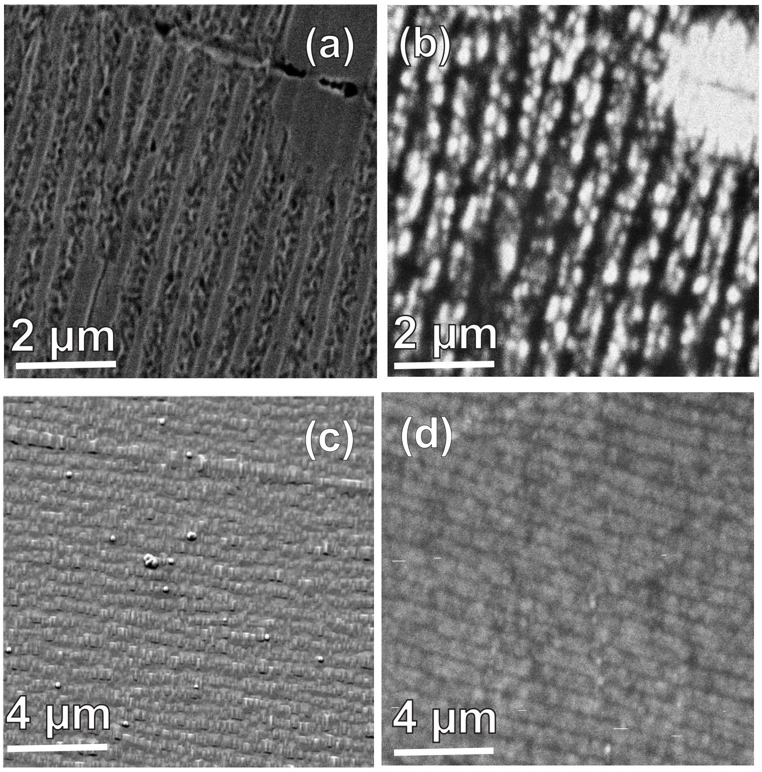

**Figure 5.4:** Room-temperature plane-view SEM micrograph of sample F (a) and CL map obtained from the same region, detected at the wavelength of the X line (b); Room-temperature plane-view SEM micrograph of sample G2 (c) and CL map detected at the wavelength of the DAP line (d).

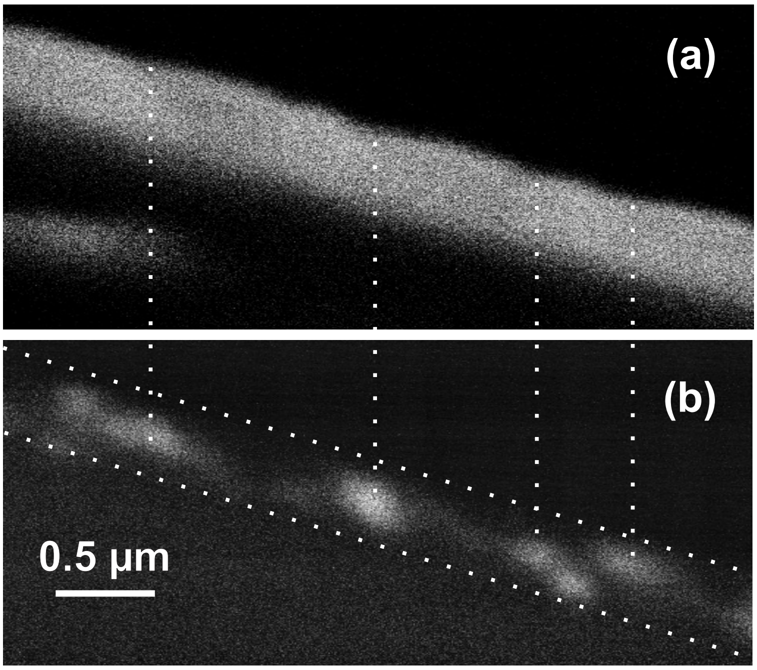

**Figure 5.5:** Cross-sectional SEM micrograph recorded at 5 K (a) and the corresponding CL map of the same region, detected at the wavelength of the X line (b) of sample F.

but seems to occur preferentially on the ridges.
For sample F, the higher light-extraction efficiency in the rough trenches compared to the smooth ridges might facilitate a stronger external emission intensity, causing a spurious contrast in the CL map. However, as seen in the cross-sectional SEM and CL micrographs shown in Fig. 5.5 (a) and (b), respectively, the X line emission actually occurs within the entire depth of layer, and not preferentially from the surface. For sample G2, in contrast, we believe that the plate-like morphology of the ridges actually enhances light extraction, since we do observe the same apparent contrast also when recording CL maps at the wavelength of the ($D^0$,X) transition.

**TEM** To examine the microstructure of the layers, we employ cross-sectional TEM. TEM studies are performed in a JEOL3010 microscope operating at 300 kV. Figure 5.6 shows two-beam bright field micrographs of cross sections of samples F and G2 with $\mathbf{g}=1\bar{1}00$ near the $[11\bar{2}0]$ zone axis. The microstructure of both samples is quite different from that of *C*-plane GaN. The density of perfect threading dislocations is found to be below $1 \times 10^6$ cm$^{-2}$. The most dominant defects are basal plane stacking faults (SFs), most of which intersect the entire thickness of the layer. The partial dislocations terminating these basal plane SFs have been determined to be of Shockley type with Burgers vectors $\mathbf{b}=\frac{1}{3}[10\bar{1}0]$ or $\frac{1}{3}[01\bar{1}0]$ [114]. Most importantly, sample F exhibits a significantly higher SF density as compared to sample G2, and most of the SFs in this sample are concentrated within the trench region. It is interesting to note that in both samples bundles of SFs occur at locations where the substrate/epilayer interface is visibly disturbed. It is thus likely that the abundance of SFs in sample F results from the pronounced roughening of the LAO(100) face when heated to the growth temperature. At the same time, the high nucleation temperature used for sample F may also facilitate an

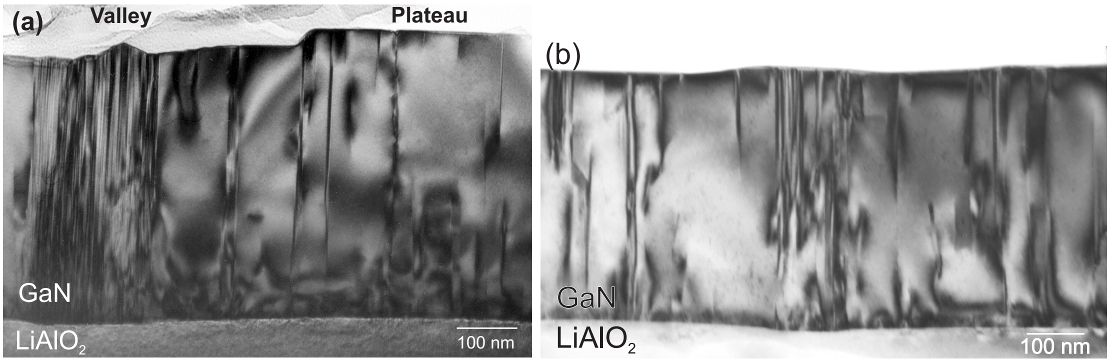

**Figure 5.6:** Cross-sectional **g**=$1\bar{1}00$ two-beam bright-field TEM micrographs near the $[11\bar{2}0]$ zone axis of sample F (a) and sample G2 (b). The defects running through the layers are identified as being basal plane stacking faults.

enhanced incorporation of O during the initial stage of growth, or even the formation of interfacial polytypoids of the type (Ga,Al)(N,O). In fact, Hagege *et al.* [115, 116, 117] have suggested that the presence of O may serve to stabilize SFs in AlN ceramics. A more recent work suggested that coalescence of two nucleation regions with different stacking sequences is the reason for the formation of stacking faults [43], as three $\langle 1\bar{1}00 \rangle$ faces have ABAB stacking and the other three have ACAC stacking. We are, at present, unable to distinguish among these possibilities mentioned above, but it is clear that a low nucleation temperature results in a significantly improved microstructure and surface morphology. Furthermore, it is also clear that the X emission from sample F is in fact related to the presence of SFs, since the emission is the strongest at places where the SFs are most abundant.

NP LAO substrates are free of the trench-pattern which is usually observed on AE LAO substrates. As a consequence, there is no SF bunching, as observed in Fig. 5.7. However, SFs are still the dominant defects in *M*-plane GaN films grown on NP LAO substrates. The overall SF density is similar to that in GaN grown on AE LAO substrates. Nevertheless, the surface morphology is greatly improved, as clearly seen in Fig. 5.6 and Fig. 5.7.

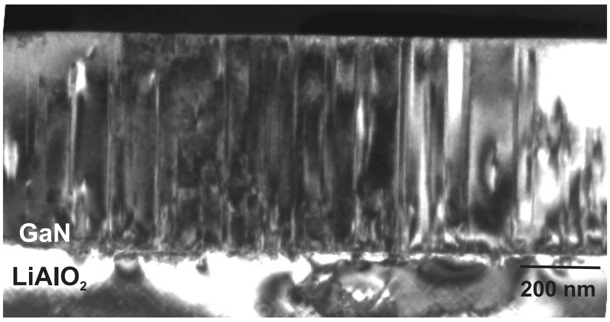

**Figure 5.7:** Cross-sectional **g**=$1\bar{1}00$ two-beam bright-field TEM micrographs near the $[11\bar{2}0]$ zone axis of one GaN film grown on a NP LAO substrate.

## 5.2 Stacking-faults related luminescence

Having established the correlation between the presence of SFs and the X emission, the question remains whether this emission merely originates from point defects and impurities which are accumulated in the vicinity of the SFs, or is in some sense an emission intrinsic to SFs, such as excitons bound to SFs. For this purpose, we investigate the dependence of the low-energy PL lines from samples F and G2 on excitation density, as well as the recombination dynamics of these transitions. The generation rate of CL is varied by changing the excitation area, but keeping the acceleration voltage (4 kV) and beam current (0.3 nA) constant. Its value is calculated taking backscattering corrections into account.

**Excitation-density dependence** Figures 5.8 (a) and (b) show the excitation-density-dependent PL spectra of samples F and G2, respectively, at 5 K in the near-bandgap spectral region. For better comparison with the CL measurements shown below, the excitation density is given in units of generation rate per unit area, which is identical to the photon flux in the case of PL. For sample F, the position and width of the X line is independent on the generation rate. In contrast, the DAP line of sample G2 exhibits a clear blueshift with increasing generation rate, which is a signature for DAP transitions because of the saturation of long-distance DAPs with increasing carrier density. For both samples, the ($D^0$,X) transition energy is, as expected, independent of generation rate. The low-energy shoulder (labeled $I_3$) of the ($D^0$,X) transition in sample F has an energy separation of 19 meV and thus may originate from an acceptor-bound exciton or a donor-to-band transition. Figure 5.9 shows the spectrally integrated PL and CL intensities of both the X and DAP transitions versus generation rate. Over five orders of magnitude, the intensity of the X transition rises linearly with increasing excitation density. The X transition thus exhibits the characteristics expected for an intrinsic transition. In contrast, the DAP transition is saturated at generation rates exceeding $10^{19}$ cm$^{-2}$s$^{-1}$, confirming its extrinsic origin. It is also noted that both the X transition and the DAP transition quench rapidly when the temperature is above 50 K,

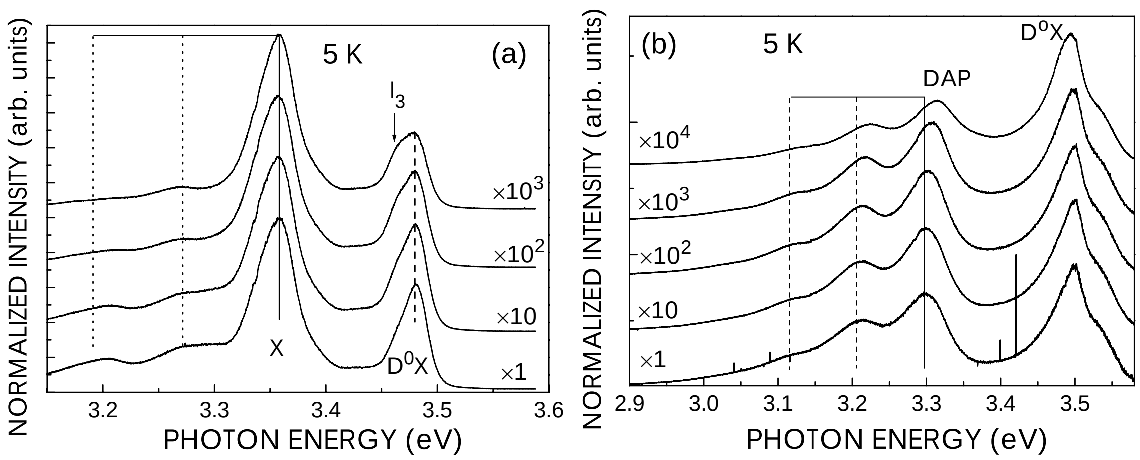

**Figure 5.8:** Excitation density-dependent PL spectra of sample F (a) and sample G2 (b) at a fixed temperature of 5 K. The unit generation rate in (a) and (b) is $9\times10^{15}$ cm$^{-2}$s$^{-1}$ and $8.35\times10^{15}$ cm$^{-2}$s$^{-1}$, respectively. The equidistant phonon replicas are indicated by vertical lines.

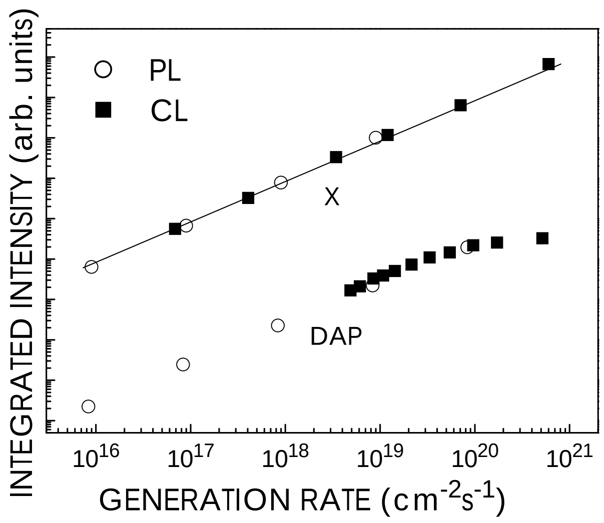

**Figure 5.9:** Integrated PL and CL intensity of the low energy bands in sample F (X) and G2 (DAP) versus the generation rate. The solid line is a linear fit with a slope of 1.0. The experimental data for PL and CL are vertically offset for clarity.

and at room temperature they are hardly resolved.

**Band profile** Although stacking faults do not introduce localized states in the band gap [118], they form quantum-well-like structures since they can be considered as thin zinc-blende layers embedded in the wurtzite matrix. The calculated band alignment [119, 120, 118] represents a type II heterojunction, where electrons are captured in the potential well, which then attract holes via the Coulomb interaction to form excitons. Rebane *et al.* [119] also calculated the binding energy of these excitons to be 45 meV. In fact, in temperature-dependent PL measurements (not shown here) we found that the X emission quenched rapidly at elevated temperatures with an activation energy of 48 meV. The good agreement between these values, however, is likely to be a mere coincidence: the calculation of Rebane *et al.* [119] neglected the spontaneous polarization of the wurtzite matrix along the [0001]-direction, i. e, perpendicular to the

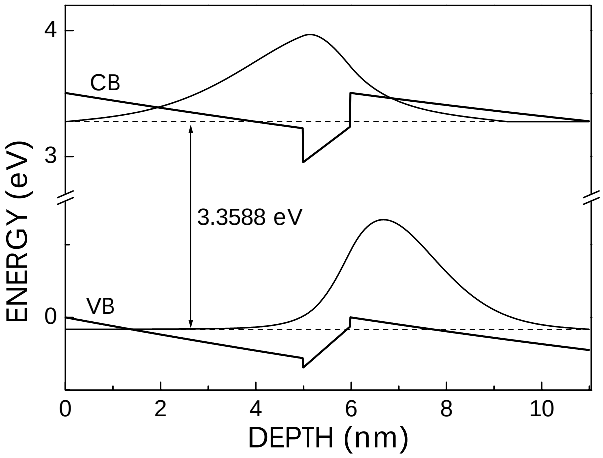

**Figure 5.10:** Band profile, energy states and electron-hole wavefunctions of a type II SF in a wurtzite GaN matrix.

SF.

Our TEM results show that the basal plane SFs terminated by Shockley-type partial dislocations are intrinsic type II SFs (also called as $I_2$) with a stacking sequence ...ABABABCACAC..., containing two units of sphalerite stacking. Therefore, the width of the potential wells is given by $2c_0$, i. e. 1.04 nm. Figure 5.10 displays the band-alignment of this type II SF within a wurtzite matrix obtained from self-consistent Schrödinger-Poisson calculations, taking the band offsets determined by Stampfl and van de Walle [118], the spontaneous polarization from Bernardini and Fiorentini and Vanderbilt [58] and assuming that the SF have a spatial separation of 5 nm [*cf.* the SF bundle in Fig. 5.6 (a)]. The band profile clearly shows that the electric field present in the barrier creates a triangular potential profile which effectively confines holes. The calculated interband transition energy agrees almost exactly with the experimental one, which, however, is somewhat fortuitous, as we did not take into account excitonic effects which would lower the transition energy by at least 30 meV.

**TR PL at 5 K** Considering the band profile shown above, the recombination dynamics of the SF emission is expected to resemble that of quantum wells with similar width and magnitude of the electrostatic field. TR PL measurements at 5 K are done with a frequency-tripled Ti:sapphire laser with a pulse width of about 200 fs. For detection, a Hamamatsu C5680 streak camera is used.

Figures 5.11 (a) and (b) show the PL transients for the SF and DAP transitions, respectively. The measured decay time of the SF transition is 1.1 ns, which indeed is close to values reported for quantum wells of similar width [121,122]. In contrast, the decay of the DAP transition is nonexponential and takes place on a time scale of about 100 ns, showing the expected behavior for this extrinsic transition.

Finally, it should be pointed that most of our samples, even those grown on NP LAO substrates, exhibit a SFE transition at low temperature (*cf.* Fig. 5.3). The observation of the DAP transition in sample G2 is most likely due to unintentional Mg incorporation because of the Mg memory effect, since this sample has been grown just after outgassing of the Mg effusion cell.

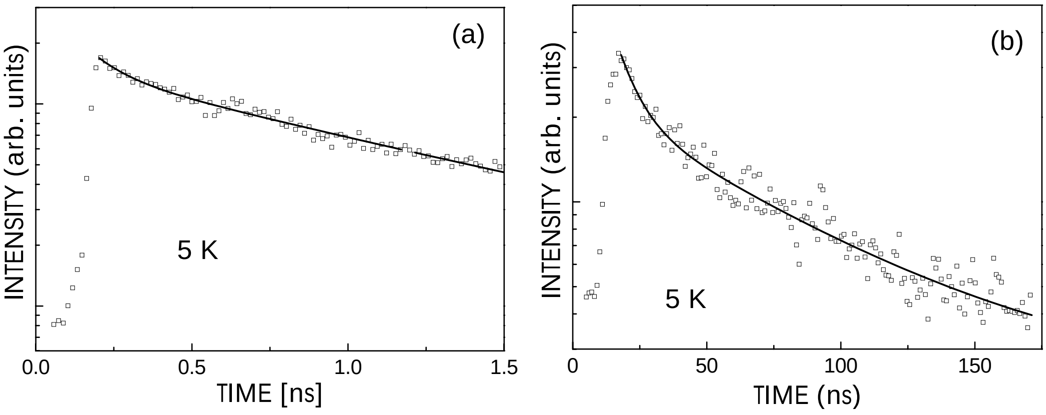

**Figure 5.11:** PL transients of the SF emission from sample F (a) and the DAP transition from sample G2 (b) recorded at 5 K.

## 5.3 Consequence of optimum growth conditions

In general, high quality *M*-plane GaN epilayers are essential for device performance. As GaN epilayers are usually used as buffer layers for quantum well and superlattice structures, their surface quality is crucial for synthesizing these desired structures. A systematic study on the optimum growth conditions for *M*-plane GaN has been presented from Chapter 3 to 5. In order to emphasize the significance of the growth conditions, it is necessary to briefly review the properties of *M*-plane GaN epilayers grown under optimum conditions, before we move to investigate (In,Ga)N/GaN quantum wells and Mg doping in the following chapters. We divided the challenge of the epitaxial growth into three sub-issues, namely, substrate, nucleation and growth. The impacts of these three sub-issues on the quality of epitaxial layers are studied separately. The optimum growth conditions for *C*-plane GaN grown on SiC(0001) by PAMBE were found to be adopting $H_2$-etched SiC substrates, a direct nucleation (the nucleation temperature $T_N$ is equal to the growth temperature $T_G$), and a stable Ga bilayer coverage on the growth front [84]. In comparison, best *M*-plane GaN epilayers are grown on NP $LiAlO_2$, with a low-temperature (580°C) GaN nucleation layer under high III-V ratio prior to growth, and under slightly Ga-rich conditions during the growth (giving trilayer at low temperature). As current commercial GaN-based devices are all [0001]-oriented, it is interesting to compare our [1$\bar{1}$00]-oriented layers' properties with their *C*-plane counterpart.

A summary of the properties of *M*-plane GaN films grown under optimum conditions is presented in Tab. 5.1. The morphological, structural and optical qualities of our *M*-plane GaN films approach those of state-of-the-art *C*-plane GaN films grown by PAMBE. This indicates that this material is indeed promising for the fabrication of devices. Note that a direct comparison of the XRC FWHMs of *M*-plane and *C*-plane might result in the erroneous conclusion that the structural quality of *M*-plane epilayers is inferior to that of corresponding *C*-plane layers. One should keep in mind, however, that the mechanism leading to the broadening of XRCs in *M*-plane and *C*-plane epilayers is different (*cf.* section 4.1.3). In particular, the structural defects in *M*-plane GaN epilayers were demonstrated to be different from those in *C*-plane films.

**Table 5.1:** Comparison of selected properties of *C*-plane and *M*-plane GaN films grown under optimum conditions. The RMS roughness is obtained over a 3×3 $\mu m^2$ area by AFM. The linewidth of x-ray rocking curves of symmetrical and asymmetrical reflections is denoted by $\Delta\omega_s$ and $\Delta\omega_a$, respectively. Note that symmetrical and asymmetrical reflections denote (1$\bar{1}$00) and (2$\bar{2}$03) for *M*-plane GaN, and (0002) and (10$\bar{1}$2) for *C*-plane GaN, respectively. The densities of screw, edge, and partial dislocations as observed by transmission electron microscopy are denoted by $\rho_s$, $\rho_e$, and $\rho_p$, respectively. ΔE(E2) is the linewidth of the $E_2$ phonon in room-temperature Raman spectra, and ΔE(PL) that of the ($D^0$,X) transition in low-temperature photoluminescence spectra.

| | RMS | XRC (arcsec) | | $\rho$ ($cm^{-2}$) | | | Δ(E) | |
|---|---|---|---|---|---|---|---|---|
| | (nm) | $\Delta\omega_s$ | $\Delta\omega_a$ | $\rho_s$ | $\rho_e$ | $\rho_p$ | $E_2$ ($cm^{-1}$) | PL (meV) |
| *C*-plane | 0.3 | 100 | 700 | $5\times10^7$ | $5\times10^9$ | $<10^6$ | 2.5 | 10 |
| *M*-plane | 0.6 | 700 | 1100 | $<10^6$ | $<10^6$ | $3\times10^9$ | 3.4 | 14 |

# 6 *M*-plane (In,Ga)N/GaN multiple quantum wells

Nonpolar wurtzite III-nitride multiple quantum wells (MQWs) are expected to be free of electrostatic fields along the growth direction. To experimentally confirm this presumption, one usually relies on the results of spectroscopic studies. The correct interpretation of these results, however, requires an accurate knowledge of the structural parameters of the samples under investigation. This statement is particularly true for the case of (In,Ga)N/GaN quantum wells, in which the surface segregation of In may severely distort the intended composition profile as indeed found for the case of *C*-plane ([0001]-oriented) structures [123, 124, 125]. In this chapter, growth of *M*-plane (In,Ga)N/GaN MQWs on LAO(100) and a detailed investigation of their structural and optical properties are described.

## 6.1 In incorporation and surface segregation

Although *C*-plane (In,Ga)N/GaN MQWs have been extensively studied, nonpolar (In,Ga)N/GaN MQWs with wurtzite structure have not been synthesized so far. A previous attempt of our group produced a predominantly *C*-plane structure because of the inappropriate nucleation conditions [126]. Here, we employ a low-temperature GaN instead of an AlN nucleation layer, resulting in pure *M*-plane growth. To study the impact of surface orientation on the In incorporation during the MQWs growth, a set of 20-period (In,Ga)N/GaN MQWs was grown on NP $\gamma$-LiAlO$_2$(100) substrates.

**Growth** For all samples, growth was initiated by a 100 nm thick low-temperature (580°C) GaN nucleation layer, after which the temperature was increased to 740°C for the growth of a 500 nm thick GaN buffer layer. Together with the improved substrate morphology, this growth procedure results in a buffer layer surface having an rms roughness of only 0.6 nm as shown in section 4.2. For the subsequent growth of the (In,Ga)N/GaN MQWs, the substrate temperature was decreased to 600°C. In, Ga, and N fluxes were identical for all MQWs, which differ only due to the different growth times for the well, namely, 25 s for samples A and B, and 40 s for samples C and D, respectively. The RHEED patterns stayed streaky during the entire growth of the MQWs. In fact, the rms roughness of the samples as determined by atomic force microscopy is between 1.2 and 1.7 nm. The samples are further characterized by high-resolution x-ray diffraction (HRXRD), secondary-ion-mass-spectroscopy (SIMS), and continuous-wave photoluminescence (cw-PL) spectroscopy.

**HRXRD** To determine the structural parameters of these *M*-plane MQWs by HRDXD, we follow the same procedure as employed in Refs. [124] and [127]. Symmetric x-ray $\omega$-$2\theta$ scans were taken with a Philips X'Pert PRO triple-axis diffractometer with a Cu $K\alpha_1$ source, a Ge(220) hybrid monochromator and a Ge(220) three-bounce analyzer crystal. We first analyze the angular positions of the satellite peaks kinematically based on the nominal growth times to obtain the structural parameters of the sample, implicitly assuming that segregation does not occur. Next, we employ simulations based on the dynamical diffraction theory [127] and vary the kinematically obtained parameters until the intensity of the satellites matches the experiment in addition to their position. The simulations are done for perfect interfaces and are convoluted with the instrumental resolution ($25''$) only. As an example, Fig. 6.1 shows $\omega$-$2\theta$ scans for sample MQW-A across the (a) GaN($1\bar{1}00$) and (b) GaN($2\bar{2}00$) reflection. Several important conclusions can be drawn from these scans:

(i) No additional signal is detected at the position of either GaN(0002) or in between GaN(0002) and $In_{0.1}Ga_{0.9}N$(0002), demonstrating that the entire structure has the expected orientational relationship, i. e., $[1\bar{1}00]_{(In,Ga)N} \| [100]_{LAO}$. Additional resonant Raman measurements (not shown here) demonstrate that the structure also fulfills the expected in-plane orientation relationship, namely, $[0001]_{(In,Ga)N} \| [010]_{LAO}$ and $[11\bar{2}0]_{(In,Ga)N} \| [001]_{LAO}$.

(ii) The angular separation between the LAO(200) and GaN($1\bar{1}00$) reflections or LAO(400) and GaN($2\bar{2}00$) indicates a lattice dilation of 0.6% along the growth direction, i. e., [$1\bar{1}00$], for the GaN buffer. This fairly high strain is at least partly a result of the coherent growth of GaN($1\bar{1}00$) on LAO(100) along the [0001] direction [63], where the lattice mismatch amounts to only 0.3%. The mismatch in thermal expansion, of course, is also compressive and enhances this effect.

(iii) Superlattice satellites up to the $2^{nd}$ order are observed for all samples, demonstrating the high periodicity of the structures and allowing us to determine their structural properties.

In fact, the agreement between the experimental and simulated profiles is quite satisfactory, whereas simulations with the kinematically obtained parameters (not shown here) exhibit satellite intensity ratios clearly inconsistent with those experimentally observed. The results of this analysis are summarized in Tab. 6.1, and indicate a very significant In surface segregation for all samples under investigation. Interestingly, the In content obtained from this analysis is $\sim$7%, while *C*-plane samples grown under identical conditions exhibit an In content of about $\sim$15%.

The broadening of the satellites in the experiment with respect to the simulation, which is particularly evident in Fig. 6.1 (b), gives rise to concern about the validity of our ap-

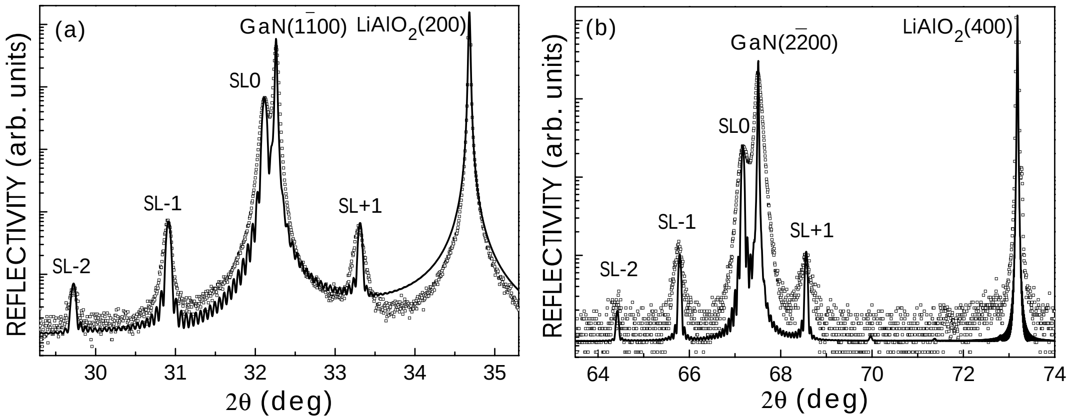

**Figure 6.1:** Experimental (□) and simulated (—) triple-axis $\omega$-$2\theta$ scans across the (a) GaN($1\bar{1}00$) and (b) GaN($2\bar{2}00$) reflection of a 20-period *M*-plane (In,Ga)N/GaN MQW grown on $LiAlO_2$(100) (sample MQW-A). The superlattice satellites are denoted by SL±n.

**Table 6.1:** Parameters of the *M*-plane (In,Ga)N/GaN MQWs under investigation as determined by the kinematical analyses based on growth time (kin), the dynamical simulations taking the real depth profile of In into account (dyn), and SIMS. The In content and the well width are denoted as $x$ and $d_w$ (nm), respectively. The lower and upper margin for the well thickness in the SIMS column corresponds to the value obtained directly from the In content and that obtained from the FWHM of the In profile, respectively.

| | kin | | dyn | | SIMS | |
|---|---|---|---|---|---|---|
| Sample | $x$ | $d_w$ | $x$ | $d_w$ | $x$ | $d_w$ |
| MQW-A | 0.14 | 1.35 | 0.068 | 2.7 | 0.070 | 2.7–3.1 |
| MQW-B | 0.16 | 1.47 | 0.070 | 3.3 | 0.071 | 3.3–4.3 |
| MQW-C | 0.19 | 2.43 | 0.066 | 7.0 | 0.072 | 6.4–7.2 |
| MQW-D | 0.20 | 2.48 | 0.068 | 7.4 | 0.071 | 7.1–7.6 |

proach. Indeed, if this broadening would be caused by interface roughness, the intensity ratio between the satellites would be changed and could not be described correctly by the present model. However, the widths of the $0^{th}$ and the $-1^{th}$ satellites are virtually identical for all samples, reflecting that the broadening arises from heterogeneous strain rather than from interface roughness. A Williamson-Hall plot [91] of the width of the SL0 reflection results in an estimated heterogeneous strain along the growth direction of $1.2\times10^{-3}$, larger than that obtained typically for bare GaN layers. This result is not unexpected, as compositional fluctuations in the ternary (In,Ga)N alloy, which are believed to be largely driven by In surface segregation [128], will inevitably result in a certain degree of inhomogeneous strain.

**SIMS** In order to independently confirm the actual In content and structural parameters, we performed high-resolution SIMS measurements. SIMS was carried out with a CAMECA IMS 4f-E6 system, employing $Cs^+$ primary ions with an impact energy of 5.5 keV and $InCs^+$ ions as species for detection. The depth resolution under these conditions is about 1 nm/decade and 2 nm/decade at the leading and trailing edge, respectively. As an example, the In depth profile of sample MQW-A is shown in Fig. 6.2. The leading and trailing edges of this depth profile are 1.4 and 2.2 nm/decade, i. e., close to the instrumental resolution. The progressive damping and broadening of the signal with depth (*cf.* inset of Fig. 6.2) is caused by roughening due to the sputtering process. The actual well width can be deduced in two ways from this profile. First, we may take the In content as measured by SIMS for granted (note that $InCs^+$ detection is indeed known to be quite accurate in this regard) and combine this value with the average In content as measured by HRXRD. Second, we may take the full-width-at-half-maximum (FWHM) of the In peaks to reflect the actual well width if the instrumental broadening is Gaussian and is significantly smaller than the well width itself (otherwise the FWHM will overestimate the well width). The In contents and well thicknesses thus determined for the samples under investigation are listed in Tab. 6.1. The good agreement with those deduced from the HRDXD simulations is evident. This result signifies that In surface segregation is present on the *M*-plane as well as on the *C*-plane of GaN. The lower In content found for the former even suggests that it is stronger in the present case. In other words, the In incorporation efficiency

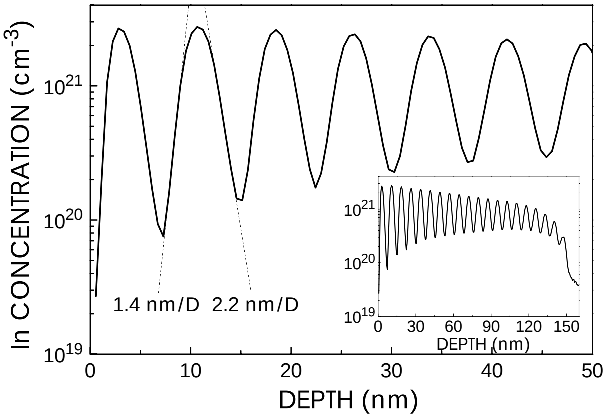

**Figure 6.2:** SIMS depth profile of the top 50 nm of sample MQW-A. The depth resolution is indicated. The entire depth profile is shown in the inset.

on the *M*-plane, phenomenologically lumping together processes such as segregation and desorption, seems to be lower when compared to the *C*-plane. An interesting point is the symmetrical "top-hat"shape of each QW in Fig. 6.2, which we observed for all samples under investigation. This observation is analogous to the case of *C*-plane (In,Ga)N/GaN MQWs [124] and indicates a $0^{th}$-order In segregation process. This process implies an In incorporation limit—here 7%—at a given growth temperature, and has the consequence that the incorporation of In does not depend on the actual amount of In floating on the growth front.

## 6.2 Recombination mechanism

The spontaneous emission of *C*-plane (In,Ga)N quantum wells is determined by both e-h wavefunctions separation due to the built-in internal electrostatic field [quantum confinement Stark-effect (QCSE)] and exciton localization caused by potential fluctuations [129, 130, 131, 132]. The realization of *M*-plane (In,Ga)N/GaN MQWs allows us to investigate the impact of excitons localization on radiative recombination without the interference of internal electrostatic fields in this materials system. To study the recombination mechanism of *M*-plane (In,Ga)N/GaN MQWs, cw-PL and time-resolved (TR) PL were carried out.

**cw-PL** Cw-PL spectra at various temperatures were recorded using a 325 nm He-Cd laser with an excitation intensity of 10 W/cm$^2$. Figure 6.3 (a) shows the evolution of the cw-PL spectra from 5 to 300 K for an *M*-plane (In,Ga)N/GaN MQW (MQW-A). The dominant emission centered close to 3 eV stems from the quantum wells. Interestingly, we also observe emission near 3.36 eV, originating from excitons bound to stacking faults in GaN [*cf*. section 5.2] and at 3.497 eV from the ($D^0$,X) transition in GaN. The energy position of the latter indicates a large compressive strain [102, 103], which is consistent with the XRD measurements described above. However, the observation of luminescence from GaN alone is interesting, since we never detected any signal from GaN in the case of *C*-plane (In,Ga)N/GaN MQWs with a total thickness, as the present sample, exceeding the penetration depth of the laser. The lack of GaN luminescence in this case is plausible: the internal electrostatic fields in the barriers of

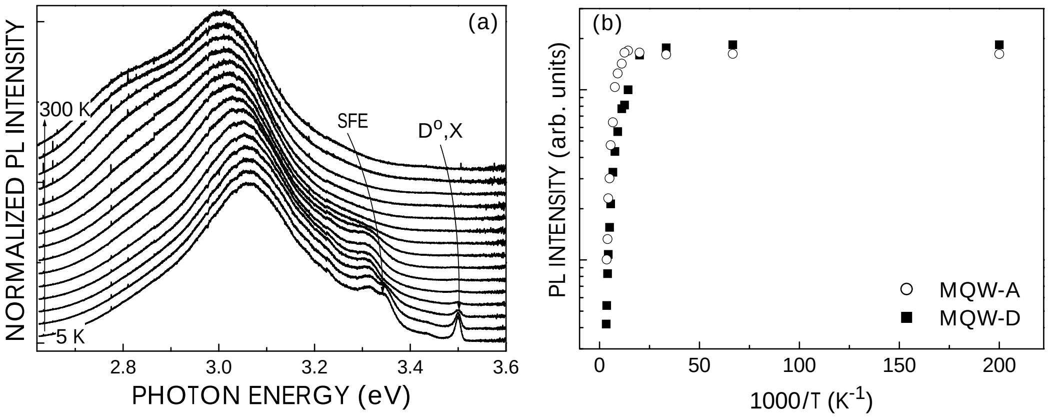

**Figure 6.3:** PL spectra of a *M*-plane (In,Ga)N/GaN MQW (MQW-A) in the temperature range from 5 K to 300 K. All spectra are normalized and vertically offset for clarity.(a) Arrhenius representations of the integrated PL intensity of MQW-A and MQW-D.(b)

*C*-plane (In,Ga)N/GaN MQWs rapidly separate electrons and holes and direct them to the wells, thereby enhancing the capture efficiency. The observation of rather strong luminescence from the GaN barriers in the present sample may thus be taken as a manifestation of the absence of internal electrostatic fields.

Figure 6.3 (b) shows Arrhenius plots of the integrated cw PL intensity of two MQWs (MQW-A and MQW-D). The total PL intensity of these two *M*-plane MQWs is reduced by a factor of 17 and 44, respectively, when the temperature is increased from 5 to 300 K. In fact, all samples under investigation exhibit a strong and broad PL band between 400 and 420 nm at room temperature. For all of our *M*-plane MQWs, the luminescence quenches by a factor of 15–50 when the temperature increases from 5 to 300 K. The PL of these MQWs is still detectable up to 500 K. This finding is in contrast to *C*-plane MQWs of similar well widths as, e. g., MQW-D ($\sim$7 nm), where the emission intensity decreases drastically with well width and is hardly detectable at room temperature.

**Anomalous temperature-dependent PL width** In both *C*-plane (In,Ga)N/GaN MQWs [133, 134, 135] and cubic (In,Ga)N/GaN MQWs [136, 137], exciton localization caused by In compositional fluctuation has a crucial influence on the radiative recombination process. A clear indication for the presence of localized states in the *M*-plane (In,Ga)N/GaN MQWs is obtained by the anomalous temperature dependence of the full-width at half-maximum (FWHM) of the PL spectrum, as shown in Fig. 6.4, for MQW-A. The narrowing of the spectrum upon increasing temperature has been observed in several materials systems in which strong localization occurs, such as InAs/GaAs quantum dots [138], (In,Ga)As/GaAs QWs [139] and (In,Ga)N QWs [140, 129]. At low temperatures, excitons are randomly trapped by the localizing centers, and the PL linewidth basically corresponds to the width of the distribution of local potential minima. With increasing temperature, excitons are thermally activated and become mobile within the band of localized states, allowing them to relax further into deeper potential minima. This thermal activation will thus result in the distinct narrowing of the linewidth. At even higher temperature, the thermal distribution of excitons will force them to populate also higher-energy states. As a result, the PL band

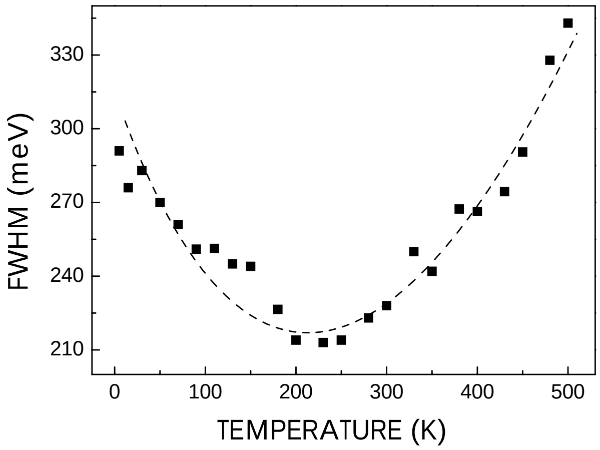

**Figure 6.4:** FWHM of the PL spectrum as a function of temperature for the *M*-plane MQW-A. The dashed line is a guide for the eye.

broadens and its width once again approaches the bandwidth.

**PL transition energy as a function of well thickness** With the accurate structural parameters obtained as described in section 6.1, a quantitative comparison of the transition energy as a function of the well thickness can be done. Figure 6.5 shows a comparison between the experimental room-temperature PL peak positions and the calculated transition energies, rigidly shifted down by 110 meV for clarity, versus the well widths. The calculated values of the transition energy are obtained by a self-consistent Schrödinger-Poisson calculation assuming a constant In content of 7%, a band gap for $In_{0.07}Ga_{0.93}N$ of 3.14 eV [141], a band offset ratio of 70:30 [142], effective electron and hole masses of 0.2 and 1 [142], a nonlinear spontaneous and piezopolarization following Ref. [54], and assuming a uniform background carrier density of $1\times10^{18}$ cm$^{-3}$ which is the typical value for bare GaN layers grown on $LiAlO_2$. The dashed curve takes the full polarization field into account, while the solid curve is obtained assum-

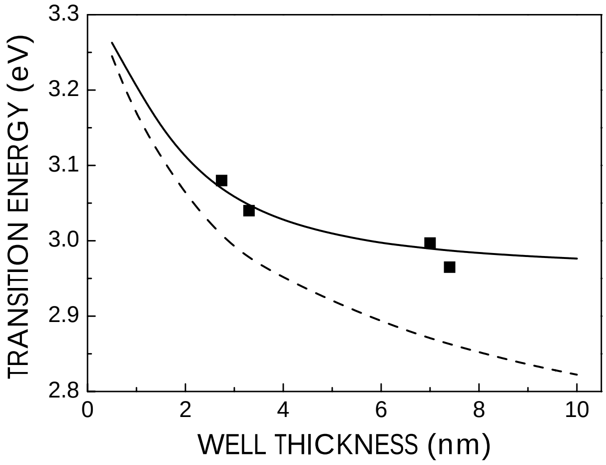

**Figure 6.5:** Transition energy as a function of the well thickness for samples MQW-A to MQW-D, assuming a constant $x$ of 7%. The symbols are experimental data, while the solid and dashed lines are calculated based on polarization charges of 0 and $9.7\times10^{12}$ C cm$^{-2}$, respectively. Note that both curves are rigidly shifted down to lower energies by 110 meV.

ing no polarization. The experimental transition energies are seen to follow closely the prediction for this quasi-flat-band case. It is most important to realize that all of the above parameters, except for the polarization constants, will merely rigidly shift these curves up or down, but will not change their shapes. A redshift, in fact, is expected as our calculations do not include excitonic effects, which may amount to 40–60 meV in the present structures [143], and exciton localization. These results thus provide evidence for the fact that the structures under investigation are free from internal electrostatic fields as encountered in corresponding *C*-plane structures.

**Recombination dynamics** To understand the dynamics of radiative recombination of the *M*-plane MQWs, TRPL measurements at 7 K and at various excitation fluences were performed. We use a frequency-doubled Ti:sapphire laser with a photon energy of 3.4 eV, a pulse width of about 200 fs and a repetition rate of 4.75 MHz. For detection, a Hamamatsu C5680 streak camera was used.
Figure 6.6 shows TRPL transients for a 15-period and a 20-period *M*-plane (In,Ga)N/GaN MQWs, after excitation of the wells only with different excitation fluences. The initial decay is rapid, faster than that we have observed for *C*-plane MQWs with similar structural parameters. The transients, however, cannot be fit by either a biexponential or a stretched exponential [144, 145, 146, 147, 148, 136]. It is noteworthy that the transients exhibit an identical behavior for different excitation fluences. This finding is in complete contrast to *C*-plane MQWs where screening of the electric field occurs at these carrier densities ($10^{18}$ cm$^{-3}$), and as such provides a further sign for the actual absence of internal electrostatic fields.
Figure 6.7 shows the transient obtained with the highest excitation fluence of the 20-period MQW plotted as $\ln(\ln[I_0/I(t)])$ vs. $\ln(t)$, in which a stretched exponential would be a straight line. Obviously, the data cannot be represented by a stretched exponential. The key for understanding the recombination dynamics for this sample is displayed in Fig. 6.8. The PL band exhibits rapid spectral diffusion during the first 500 ps after excitation. For longer time, the PL band still redshifts, but significantly slower.

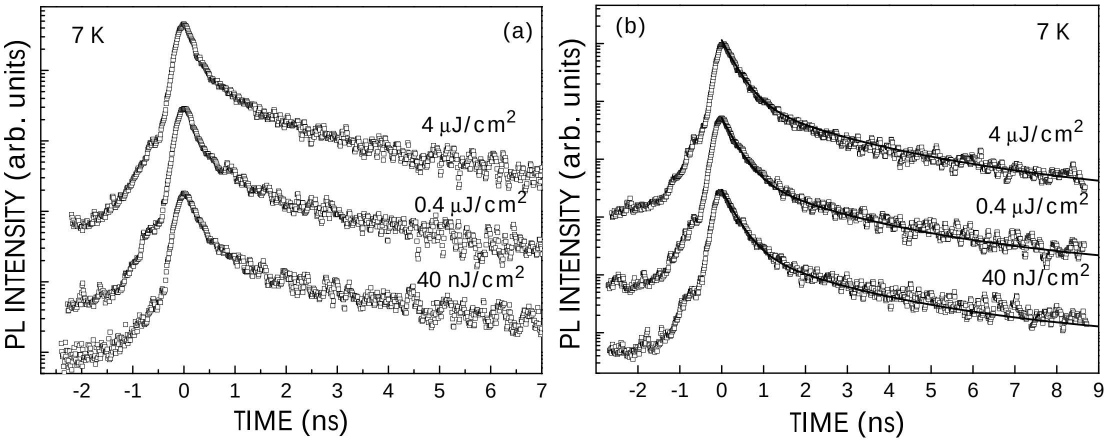

**Figure 6.6:** Integrated TRPL intensity transients at three different excitation fluences as indicated in the figure for a 15-period and a 20-period *M*-plane (In,Ga)N/GaN MQW. Open circles are the experimental data, solid lines show fits with identical parameters except for the amplitude, as described in the text. The apparent step in the data prior to the pulse is an experimental artifact.

We interpret this finding as follows: following excitation at 3.4 eV, the photogenerated excitons thermalize and initially occupy extended states in the QW. These free excitons then rapidly relax towards lower-lying localized states, which is the reason for the rapid spectral diffusion as well as for the rapid initial decay of the PL transient. Once reaching the localized states, the excitons are subject to a much slower redistribution within the band of localized states, described by a stretched exponential [144]. Mathematically, we thus deal with the following situation:

$$\frac{dn_f(t)}{dt} = G(t) - \frac{n_f(t)}{\tau_f} - \frac{n_f(t)}{\tau_r} \tag{6.1}$$

$$\frac{dn_b(t)}{dt} = \frac{n_f(t)}{\tau_r} - t^{\beta-1}\frac{n_b(t)}{\tau_b}, \tag{6.2}$$

where $G(t)$ is the excitation pulse, $n_f$ and $n_b$ the densities of free and bound excitons, respectively, $\tau_f$ and $\tau_b$ the corresponding radiative lifetimes, $\tau_r$ the relaxation time, and $\beta$ is the dimensionality parameter.

This rate-equation system has no analytical solution, but we have found that the sum of an exponential [$\propto \exp(-t/\tau_r')$, representing the relaxation from free excitons towards localized states with $1/\tau_r' = 1/\tau_f + 1/\tau_r$] and a stretched exponential [$\propto \exp(-(t/\tau_b')^{\beta'})$, accounting for the slow communication between the localized states] is a sensible approximation, although the values for the individual lifetimes and the dimensionality parameter $\beta$ are then modified. The fits shown in Figs. 6.6 and 6.7 were done with identical parameters (except, of course, for the amplitude), namely, $\tau_r' = 0.2$ ns, $\tau_b' = 1$ ns, $\beta' = 0.68$. The former value is a superposition of both relaxation and radiative recombination of free excitons, and thus cannot be decomposed. The latter parameters, however, roughly correspond to $\tau_b = 3$ ns and $\beta = 0.5$ as judged from our numerical simulations of Eqs. (6.1) and (6.2). These are similar values as found for nonpolar cubic (In,Ga)N [136,30].

Finally, it is interesting to note that the energy shift displayed in the Fig. 6.8(b) is logarithmic in nature and can be described by $\Delta E = -kT_{ac}\ln(\nu t)$, with the acoustic phonon temperature $T_{ac}$ and the attempt-to-escape rate $\nu \approx 10^{12}$ s$^{-1}$. This logarithmic relax-

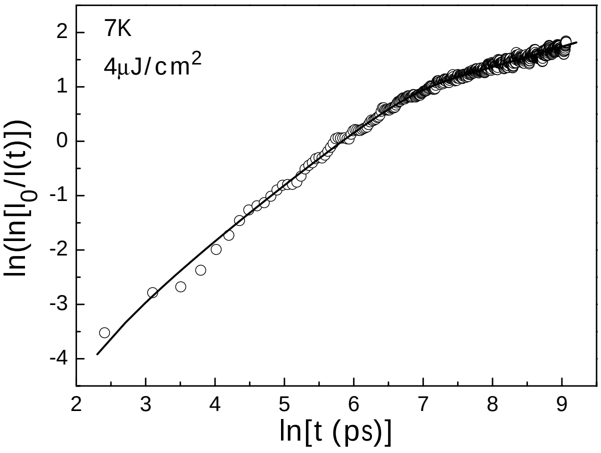

**Figure 6.7:** Doublelog-log representation of the 20-period MQW PL transient obtained with the excitation fluence as indicated. Open circles are the experimental data, solid line shows the fit.

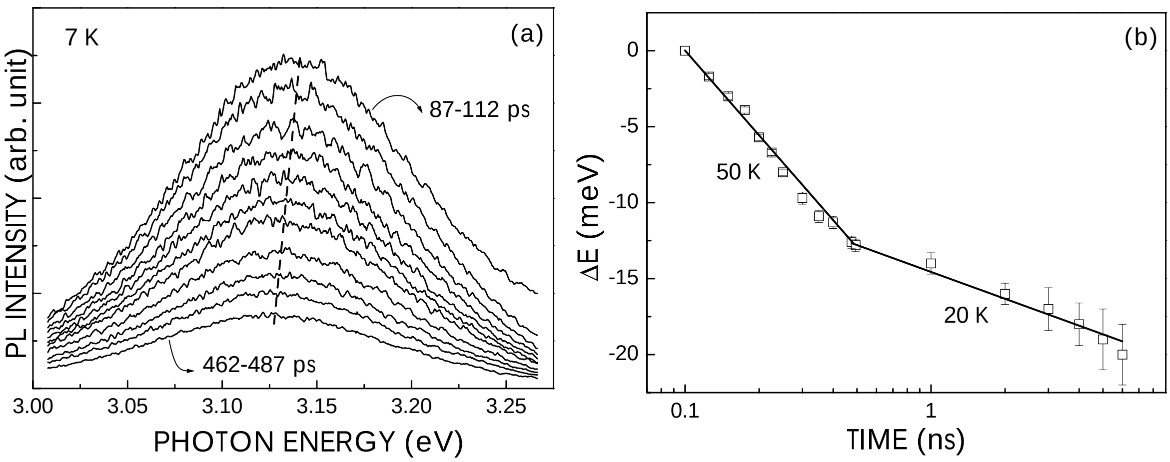

**Figure 6.8:** The spectral diffusion of the PL band for the first 500 nm (a) and temporal variation of the photon energy at the PL spetral peak (b). Note the different slopes for short and long times. The solid lines in the inset are fits according to the equation $\Delta E = -kT_{ac}\ln(\nu t)$.

ation has been observed before, both for the case of multiple-trapping relaxation of carriers within a band of localized states [149] and for relaxation of excitons towards localized states in quantum wells [150]. The temperatures required to fit our data are found to be significantly higher than the actual lattice temperature, namely, 50 K for the short- and 20 K for the long-time region. This behavior is identical to that observed by Göbel and Graudszus [149] and has been attributed to the fact that the relaxation process itself proceeds by the generation of phonons, thus increasing the phonon population over the thermal equilibrium value. In this context, the difference of the phonon temperatures extracted from our experiments is easy to be understood: while the relaxation of free excitons towards localized states proceeds exclusively by the generation of phonons, excitons, once occupying localized states, have at least partly to rely on existing phonons to assist them to migrate within the band of localized states.

## 6.3 Polarization anisotropy of spontaneous emission

Due to their hexagonal symmetry, wurtzite GaN and related compounds have a distinguished axis ([0001], the *c*-axis) and are thus inherently anisotropic materials. This anisotropy manifests itself in the spontaneous electric polarization along the polar *c*-axis. Further consequences of the symmetry of GaN are the splitting of the valence band, different refractive indices for light parallel and normal to the *c*-axis and an optically polarized spontaneous emission [151,152,153,154] and absorption [155] even in the bulk.

It is clear from these considerations that the orientation of a GaN film has a decisive influence on its physical properties. For example, a theoretical study using the sp$^3$-tight-binding method implies that *M*-plane GaN/(Al,Ga)N QWs have a lower valence-band density of states and larger optical matrix elements than corresponding *C*-plane structures, resulting in improved lasing performance [156]. Moreover, it has been recently shown that *M*-plane GaN is an attractive candidate for the realization of polarization sensitive detectors [47]. In this context, it is imperative to understand the selection rules for interband transitions in these structures. In previous work, this issue was addressed by investigating the polarization anisotropy in *M*-plane GaN films [155] and GaN/(Al,Ga)N multiple quantum wells [157]. In agreement with theoretical predictions, the linear polarization degree of these structures is close to unity. An open and important question, however, is whether or not the ubiquitous exciton localization in (In,Ga)N destroys this strong polarization anisotropy. The realization of *M*-plane (In,Ga)N/GaN MQWs allows us to answer this question. In this section, we study the in-plane polarization anisotropy of the spontaneous emission of an *M*-plane (In,Ga)N/GaN MQW by photoluminescence (PL).

The sample investigated is a 20-period *M*-plane (In,Ga)N/GaN MQW. The polarization anisotropy of the PL spectra was measured in backscattering geometry ($\mathbf{k}\perp c$) using a $\mu$-PL setup, utilizing the 325 nm line of a He-Cd laser for excitation and a liquid $N_2$ cooled charged-coupled-device camera for detection. The linear polarization of the PL at 10 K was analyzed by rotating a polarizer between a polarization angle $\phi$ of 0° and 360° (0° refers to $\mathbf{E}\parallel c$) in front of a single monochromator. The experimental data were carefully corrected for the (weak) polarization dependence of the setup. Temperature-dependent PL measurements were performed in a conventional PL setup using the same excitation and detection scheme as described above.

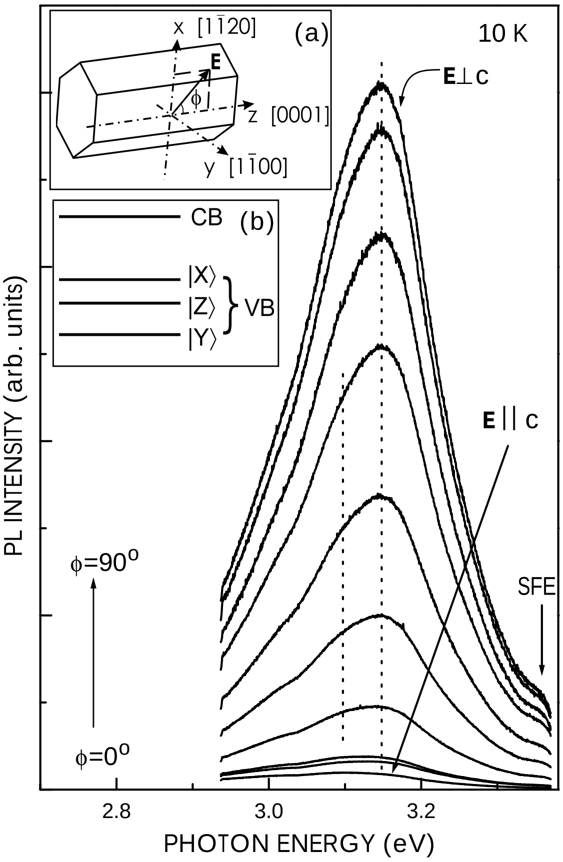

**Figure 6.9:** $\mu$-PL spectra of a *M*-plane (In,Ga)N/GaN MQW at 10 K as a function of polarization angle from 0° to 90°. The dotted lines indicate the PL peak positions for $\mathbf{E}\perp c$ and $\mathbf{E}\parallel c$. Inset (a) shows a scheme of the wurtzite GaN unit cell and the coordinates used with the corresponding azimuths, whereas inset (b) illustrates schematically the valence band order in strained *M*-plane GaN.

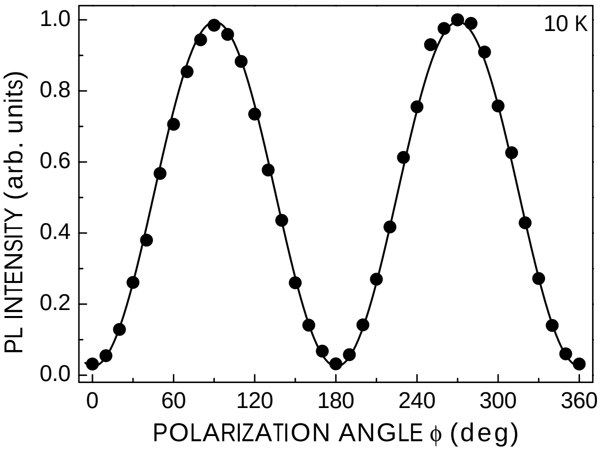

**Figure 6.10:** Spectally integrated $\mu$-PL intensity at 10 K for the 20-period *M*-plane (In,Ga)N/GaN MQW as a function of polarization angle. The circles represent the experimental data and the solid line is a least-squares fit to a $\sin^2 \phi$.

**In-plane polarization anisotropy of spontaneous emission** Figure 6.9 shows the low-temperature PL spectra as a function of $\phi$ ranging from $0^\circ$ to $90^\circ$. The dominant PL band at 3.14 eV stems from the (In,Ga)N/GaN MQW, while the higher-energy shoulder located near 3.36 eV originates from excitons bound to stacking faults (SFE). (see section 5.2) Obviously, the entire emission is strongly polarized. However, contrary to the case of GaN/(Al,Ga)N MQWs [157], the peak energy of the PL band varies with polarization angle. A low energy shoulder located at around 3.1 eV becomes more prominent with decreasing polarization angle, and eventually dominates the spectrum for $\phi = 0$, i. e., $\mathbf{E} \| c$.

This finding is surprising, since it seems at first glance to contradict our understanding of the bandstructure of *M*-plane GaN. As described in detail in Ref. [158], the anisotropic in-plane compressive strain experienced by the (In,Ga)N films breaks the symmetry in the $x$-$y$ plane of the wurtzite crystal and renders the original $|X \pm iY\rangle$-like valence-band states of unstrained wurtzite GaN into $|X\rangle$-like and $|Y\rangle$-like states (see Fig. 6.9 for our choice of coordinates). The $|X\rangle$-like state is raised in energy by the strain, while of the $|Y\rangle$-like state is pushed down below the $|Z\rangle$-like state (*cf.* Fig. 6.9). The inter-band transition lowest in energy is thus that involving the $|X\rangle$-like valence band which, according to its symmetry, is expected to be predominantly $x$-polarized ($\mathbf{E} \perp c$). The transition involving the $|Z\rangle$-like valence bands occurs at higher energy and is expected to be $z$-polarized ($\mathbf{E} \| c$). In our experiment, however, the situation seems reversed, as the PL band blue shifts when going from $\mathbf{E} \| c$ to $\mathbf{E} \perp c$. It should be noted that a corresponding *C*-plane with similar structural parameters did exhibit an isotropic emission independent of the polarization angle, as theoretically expected.

**PL intensity as a function of $\phi$** For a more quantitative view, the spectrally integrated PL intensity is plotted versus $\phi$ in Fig. 6.10. The $\sin^2 \phi$ fit agrees well with the experimental data and thus most clearly shows the almost completely $x$ polarization of the entire PL band. Any contribution from a $z$-polarized transition would reduce the amplitude as they would result in an additive term proportional to $\cos^2 \phi$.

**Apparent band shift** To resolve the unexpected shift of the PL band, we next examine the PL spectra in more detail. Figure 6.11 presents the normalized PL spectra for $\phi = 0^\circ$ and 90° as well as the energy-resolved polarization degree. The spectrum taken with $\mathbf{E}\perp c$ peaks at 3.14 eV, but exhibits a (poorly resolved) shoulder at 3.1 eV, just where the spectrum taken with $\mathbf{E}\| c$ has its maximum. Similarly, the latter spectrum exhibits a bump at 3.14 eV, corresponding to the maximum of the former (the shoulder at 3.01 eV might be due to a phonon replica of the dominant transition in this spectrum). It thus seems that the PL band consists of (at least) two contributions, the respective strength of which varies with polarization angle. Indeed, as shown in the inset of Fig. 6.11, the spectrum taken at $\phi = 20^\circ$ exhibits a top-hat shape, indicating that these two contributions have equal strength at this polarization angle. We attribute this finding to the superposition of transitions involving extended states and a band of localized states. This interpretation is confirmed by the energy dependence of the polarization degree $\rho$, obtained in the usual way as:

$$\rho = \frac{I_\perp - I_\|}{I_\perp + I_\|}, \tag{6.3}$$

where $I_\perp$ ($I_\|$) is the PL intensity for $\mathbf{E}\perp c$ ($\mathbf{E}\perp c$).

As seen in Fig. 6.11, the polarization degree thus obtained amounts to 96% at high energies, but gradually decreases to 90% with decreasing energy. The degree of polarization is thus even higher than that found for GaN/(Al,Ga)N MQWs, which is likely to

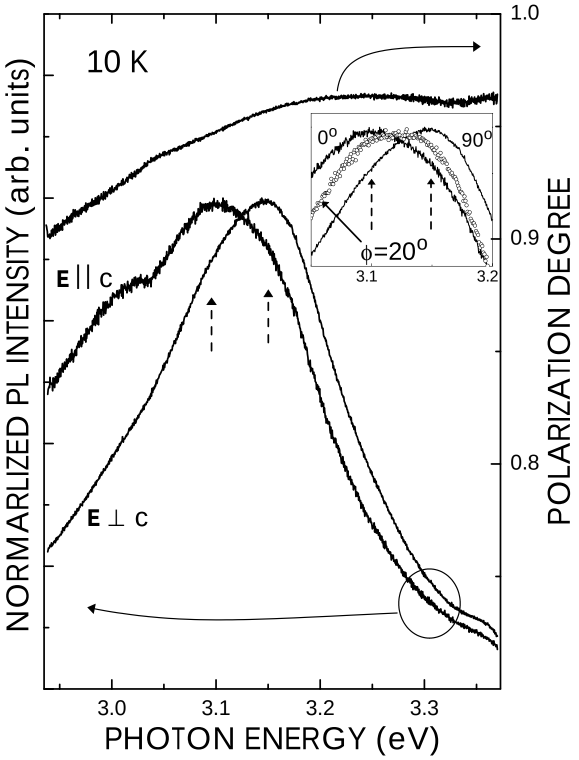

**Figure 6.11:** Normalized $\mu$-PL spectra polarized parallel and perpendicular to the $c$-axis for the $M$-plane (In,Ga)N/GaN MQW. The polarization degree as a function of photon energy is also shown. The arrows indicate the positions for the PL maximum in one spectrum and the corresponding shoulder in the other one. The inset is a magnified view of the normalized spectra at $\phi$=0°, 20° and 90°.

be a result of the large valence-band-splitting induced by the high compressive strain within the wells [157]. The monotonous decline of $\rho$ with decreasing emission energy has been observed previously for excitons localized by compositional fluctuations in $\mathrm{CdS}_{1-x}\mathrm{Se}_x$ [159]. A possible explanation for this behavior is the increased mixing of the different valence band states due to stronger confinement. In any case, it is clear that the spectral shift of the PL band is an apparent one, in that it solely results from the different $\rho$ of the states involved in the emission process. The states involved in the emission process are of predominant $|X\rangle$-like character. Even considering the high strain within the wells, the valence-band splitting is unlikely to exceed the total width of the PL band. This finding thus implies that the PL band stems almost entirely from transitions involving localized states of different potential depth which are not in equilibrium with each other [157].

# 7 Mg-doped *M*-plane GaN

To fabricate GaN-based light-emitting devices, controllable p-type doping is required. Mg is the most widely-used dopant for achieving p-type GaN(0001). The large ionization energy ($E_a$) of Mg, i. e. $\sim$200 meV, requires a two orders of magnitude higher Mg concentration in order to achieve the desired hole concentration at room temperature. Unfortunately, as the Mg doping level in conventional *C*-plane films is increased, a polarity inversion from Ga-polar to N-polar occurs at the growth front, significantly reducing the Mg incorporation. The Mg incorporation in the nonpolar GaN($1\bar{1}00$) orientation, the *M*-plane, is inherently free from this problem.

In this Chapter, a study of the impact of the growth temperature and III-V stoichiometry on the Mg incorporation in *M*-plane GaN is presented. Then both optical and electrical measurements are discussed.

## 7.1 Mg incorporation

**Growth** Growth of a 50 nm low-temperature nucleation layer was initiated at 580°C under Ga-rich conditions. Then the substrate temperature was raised to 740°C and a 150 nm unintentionally doped GaN buffer was deposited with a Ga flux of 0.475 ML/s and a N flux of 0.275 ML/s, resulting in stable Ga coverage on the growth front (*cf.* section 4.3). Note that these as-grown films are n-type with an electron concentration ($n_e$) of $\sim 10^{18}$ cm$^{-3}$. The structures grown incorporate four 100 nm Mg-doped layers separated by three 100 nm undoped GaN spacers. To establish a smooth growth front prior to Mg doping, these spacer layers were grown under the optimum conditions identified above. The Mg flux was controlled by varying the Mg effusion cell temperature from 300 to 450°C in steps of 50°C. The Mg-doped layers in samples A and B were grown at 740°C, under Ga-stable (trilayer) conditions for sample A and slightly N-rich conditions for sample B. For samples C and D, the temperature during the Mg-doped layers was set to 630°C, with Ga-stable conditions for sample C and slightly N-rich conditions for sample D. High-resolution triple-crystal x-ray diffraction demonstrated that all samples are purely GaN($1\bar{1}00$).

**SIMS** The Mg depth profiles were measured by secondary-ion mass spectroscopy (SIMS) in a CAMECA IMS 4f system, employing $O^{2+}$ primary ions with an impact energy of 8 keV. The O depth profiles were measured by SIMS in another CAMECA IMS 4f-E6 system, employing $Cs^+$ primary ions with an impact energy of 14.5 keV. The depth resolution under these conditions is about 10−13 nm/decade. It should be pointed out that the SIMS detection limit for O is about $2\times10^{18}$ cm$^{-3}$ with this setup.

Figure 7.1 shows SIMS depth profiles for Mg and O in the four samples under investigation. The O spike close the surface is an artifact due to surface contamination, while the rising Mg signals at the interface between the epilayer and the substrate are caused by charging effects.

Two important conclusions can be immediately drawn from these profiles.

(i) A Mg concentration of up to $8\times10^{20}$ cm$^{-3}$ is obtained in sample D. This concentration is significantly higher than what can be obtained in *C*-plane GaN(0001), for which

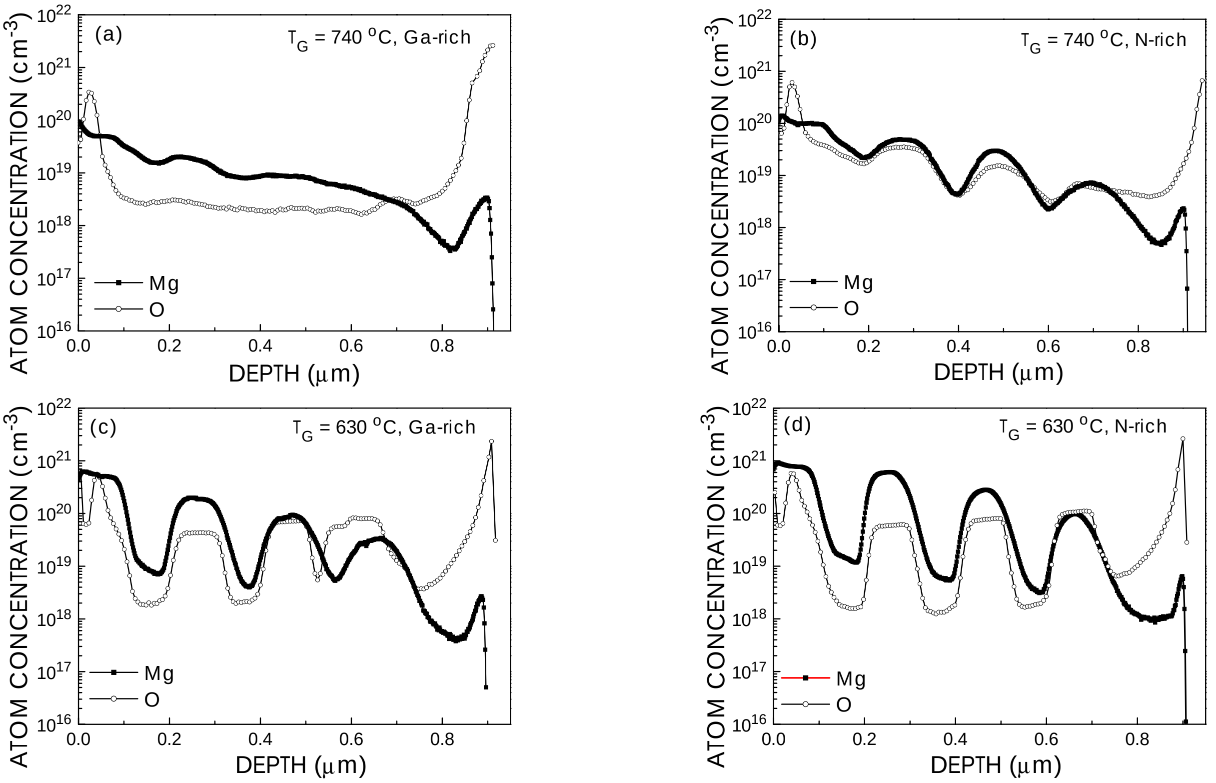

**Figure 7.1:** Mg and O depth profiles of four Mg-step-doped *M*-plane GaN samples. Sample A (a), B (b), C (c), and D (d).

a polarity inversion occurs as soon as the Mg concentration exceeds $8\times10^{19}$ cm$^{-3}$ [160]. The (0001)-oriented film (Ga-face) converts itself into (000$\bar{1}$)-oriented (N-face) and this process is not reversible. The incorporation efficiency of Mg on N-face GaN is much lower (two orders of magnitude) than on Ga-face GaN [160], resulting in a drastic drop of the Mg concentration. However, in a recent report a doping level of $\sim2\times10^{20}$ cm$^{-3}$ could be achieved without inversion domains, if a complete Ga wetting layer was deposited on the substrate prior to growth [161]. As [1$\bar{1}$00] is a nonpolar direction in the wurtzite structure, no polarity inversion can occur along the growth direction and Mg doped *M*-plane GaN with a higher Mg concentration can be readily obtained.
(ii) The abruptness of the Mg step-doping depends on both temperature and stoichiometry. Samples C and D have sharper profiles than samples A and B grown at higher temperature. For example, the Mg profile of sample D has leading and trailing edges of 16 nm/decade and 31 nm/decade, while sample B has five times wider leading and trailing edges. This finding provides evidence for bulk diffusion. Note also that the abruptness degrades with depth, i. e., with annealing time during growth. For instance, in sample C, the trailing edge of 24 nm/decade for the top Mg-doped region increases up to 55 nm/decade for the first Mg-doped region. The thermal diffusion process should lead to a symmetrical Mg profile. However, even considering the better SIMS resolution for the leading edge than that for the trailing edge, we observe that the slopes of the leading edges are larger than those of the trailing edges in Fig. 7.1 (b). Furthermore, sample A shows a much more smeared-out Mg depth profile than sample B, although the growth temperature is the same. These indicate a strong Mg surface segregation, which is also observed on GaN(0001) films [162, 163]. Under N-

rich condition and low growth temperature, the Mg segregation is restrained to some extent, which can be determined by comparing the slopes of the leading edges in the Mg profiles of these four samples.

The O depth profiles follow the Mg distribution as seen in Fig. 7.1, indicating a strong reactivity of Mg with O, similar to the case of O in $Al_xGa_{1-x}As$ [164]. The out-diffusion of O from the oxide substrate is not significant, for example as seen in sample A. In fact, uniformly Mg doped *M*-plane layers grown up to 750°C do not show any notable O out-diffusion, as compared with their *C*-plane counterparts grown on SiC(0001) under identical conditions.

Mg and O average concentrations as a function of inverse Mg cell temperature are plotted in Fig. 7.2 (a) and (b), respectively. In Fig. 7.2 (a), the temperature dependence of the Mg vapor pressures is included. The absolute Mg concentration depends strongly on substrate temperature. However, all samples show a similar Mg incorporation behavior, with an effective activation energy of 0.28 eV. Note that the activation energy of Mg evaporation is 0.66 eV, deduced from the Arrhenius plot of the Mg vapor pressure. This observation indicates that Mg segregation on and desorption from the growth front remain the rate-limiting steps even at low growth temperature. The absolute Mg concentration also depends on stoichiometry, but less strongly than on substrate temperature. This finding reflects that Mg surface segregation occurs and is significantly enhanced on the Ga-terminated surface. Note, however, that samples grown under Ga-stable conditions are significantly smoother than those grown under N-rich conditions.

If we only consider the Mg incorporation efficiency which might be needed for a high hole concentration, the *M*-plane is undoubtedly superior to the *C*-plane. However, one should bear in mind that a high Mg concentration does not necessarily result in a high hole concentration or high p-type conductivity, as self-compensation might eventually occur and more scattering centers also lower the mobility.

The O concentration for *M*-plane layers grown under standard conditions was found to be at the detection limit of SIMS. Furthermore, in Fig. 7.2 (b), the samples grown at the high temperature show lower O levels in Mg-doped regions, compared with their

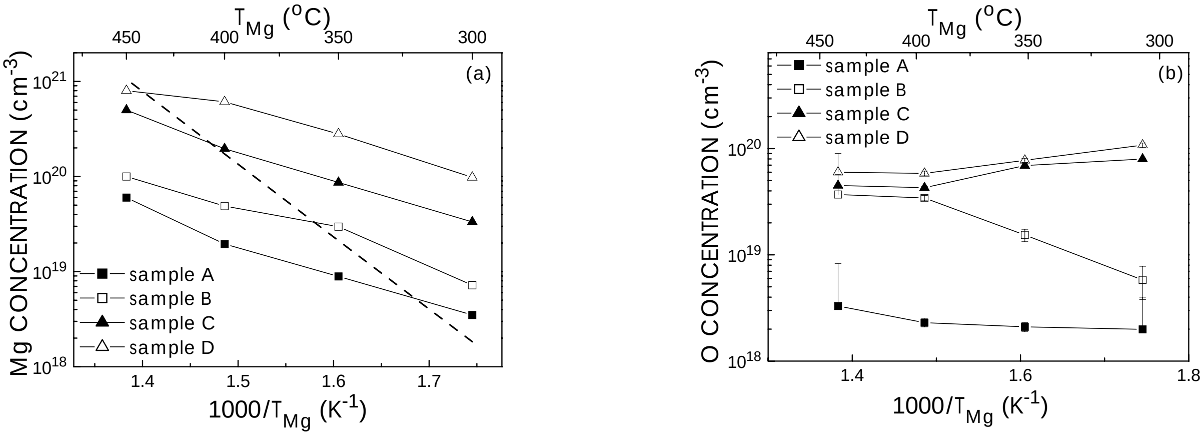

**Figure 7.2:** Arrhenius plots of Mg (a) and O (b) concentrations of four investigated *M*-plane GaN samples. The solid line connecting experimental data points are guide for eye. The dashed line in (a) is Mg vapor pressure as a function of inverse Mg temperature, whose unit in this plot is arbitrary. Note that the SIMS detection limit for O is about $2\times10^{18}$ $cm^{-3}$.

counterparts grown at the lower temperature. The determination of O concentrations in the regions close to the surface is rather difficult due to the artificial O spike at the surface, as seen from Fig. 7.1. This is reflected by the large error bars in Fig. 7.2 (b). Additionally, the O incorporation into Mg-doped GaN under N-rich conditions can be an order of magnitude higher than under Ga-rich conditions. These findings are similar to the case of unintentional O incorporation into (Al,Ga)N [165]. Thus, the growth at high temperature with a stable Ga coverage seems to be an effective way to prevent the undesired incorporation of O. Furthermore, the O concentration rises as the Mg flux increases in sample B, while it decreases in sample C and D. The former finding seems to imply that a higher Mg concentration leads to an enhanced incorporation of O. However, the reason for a decrease of O incorporation as the Mg flux increases in sample C and D is not yet clear.

The unintentional O can originate from (i) residual O in the vacuum chamber, (ii) dissociation of $LiAlO_2$, (iii) the nitrogen gas. The base vacuum pressure of our growth chamber is about $7\times10^{-11}$ Torr without detectable O signal by quadrupole mass spectrometry. Concerning the possible dissociation of $LiAlO_2$, we did not observe any decomposition up to 1300°C in vacuum with the help of mass spectrometry (*cf.* section 3.1). However, we cannot rule out O released from O-containing compounds evaporated from $LiAlO_2$ if Mg acts as a catalyzer. The most probable source of O, however, is the $N_2$ gas. Although the $N_2$ gas has a purity of 6N and is then further purified by a SAES filter, it still contains O in the ppb range. Considering the low cracking efficiency of the plasma source, this may still lead to a significant O incorporation [165, 166].

**XRD** The crystal quality of uniformly Mg-doped *M*-plane GaN films is examined by XRC. The FWHM of the $(1\bar{1}00)$ reflection in XRC is plotted in Fig. 7.3 as a function of Mg cell temperature. The FWHM decreases as the Mg flux increases and reaches a minimum of 270 arcsec with a Mg cell temperature of 400°C. A further increase of the Mg flux broadens the XRC again. The density of defects, at least those related to the symmetrical XRC broadening, seems to be reduced as a result of the Mg incorporation.

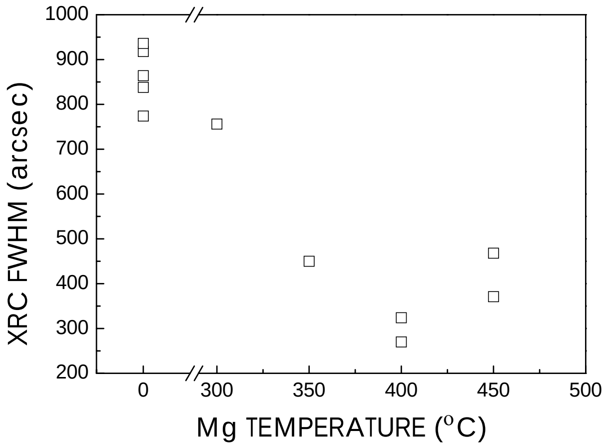

**Figure 7.3:** XRC FWHMs of uniformly Mg-doped *M*-plane GaN as a function of Mg temperature.

## 7.2 Optical and electrical properties

### 7.2.1 Optical measurements

In this part, two uniformly Mg-doped *M*-plane GaN samples with a thickness of 1.2 $\mu$m are investigated. These two samples were grown under the same conditions as the Mg doped regions of the step-doped sample A described in the last section. The only difference between these two samples is the Mg doping level. One sample was doped with $T_{Mg}$ at 350°C (hereafter called as sample UA), the other one (named by sample UB) was doped with $T_{Mg}$ at 400°C. The corresponding Mg concentrations are $1\times10^{19}$ and $2.5\times10^{19}$ cm$^{-3}$ for samples UA and UB, respectively. The samples were characterized by continuous wave PL. PL spectra at various temperatures and excitation intensities were recorded using the 325 nm line of a He-Cd laser.

**PL** Figure 7.4 shows the PL spectra of samples UA and UB at 5 K. The excitation power for both was 30 mW, which is corresponding to a generation rate of about $8.35\times10^{19}$ cm$^{-2}$s$^{-1}$. Note that this excitation intensity is the upper limit of our PL set-up. The spectra are dominated by a broad transition around 3.3 eV together with two equidistant low-energy shoulders. From the energy separation, these shoulders are attributed to the phonon replicas of the peak near to 3.3 eV, similar to the DAP peak in sample G2 mentioned in section 5. The near band edge transition is visible, but rather weak, particularly in sample UB. Note that this near band edge transition is not detected for both samples under lower excitation intensities.

To explore the origin of the dominant peak around 3.3 eV, excitation-density dependent PL measurements were carried out, similar to what was done for sample G2 in section 5.2. Figure 7.5 (a) and (b) show the PL spectra of samples UA and UB under various excitation intensities, respectively. Both an emission blueshift and a narrowing of the peak with increasing generation rate are characteristic features of the DAP transition in semiconductors. On the other hand, both phenomena can also result from the screening of the potential fluctuation caused by the random distribution of charged

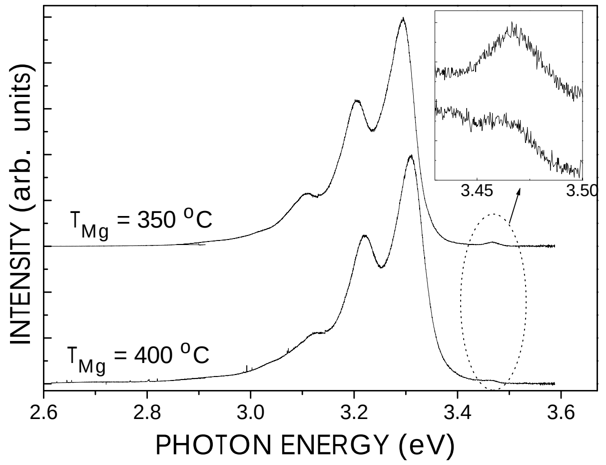

**Figure 7.4:** PL spectra of sample UA and UB recorded at 5 K. The excitation intensity is corresponding to a generation rate of about $8.35\times10^{19}$ cm$^{-2}$s$^{-1}$. The inset shows the near-band-edge part of the both spectra.

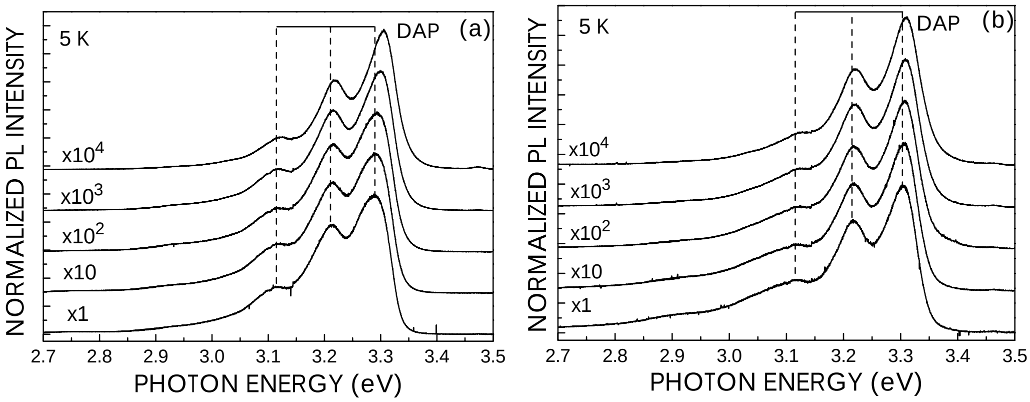

**Figure 7.5:** Excitation density-dependent PL spectra of sample UA and UB recorded at 5 K. The unit generation rate is about $8.35\times10^{15}$ cm$^{-2}$s$^{-1}$. The equidistant phonon replicas are indicated by vertical lines.

impurities in highly compensated semiconductors. Once the DAP transition saturates under the high excitation intensity, the near band-edge transition will take over. This is demonstrated in the inset of Fig. 7.4. In addition, it should be pointed out that the DAP emission band in both samples remains the dominant transition up to room temperature. This behavior is different from the case of sample G2 mentioned in section 5.2, which has a dominant ($D^0$,X) transition even at 5 K. This indicates that a large amount of Mg in both samples are incorporated substitutionally.

### 7.2.2 Electrical measurements

The purpose of Mg doping is to realize p-type conductivity. So the electrical properties of uniformly Mg-doped *M*-plane GaN layers are investigated.

**Resistivity** Figure 7.6 shows the room temperature resistivity of Mg-doped *M*-plane films as a function of Mg temperature. The resistivity of these samples monotonously increases with Mg cell temperature, indicating a higher and higher degree of compensation of the background electron density. The resistivity of the layer with the highest Mg concentration is 54 Ωcm at 300 K, which is about one order of magnitude higher than that of *C*-plane layers grown under virtually identical conditions. Possible reasons for this higher resistivity include an enhanced tendency of self-compensation on GaN($1\bar{1}00$) and/or a higher background electron density. The Hall measurements indicate that layers with the highest Mg concentration are p-type, but impurity band conduction seems to dominate. Nevertheless, in conjunction with the observation of the DAP transition in PL, it is evident that an appreciable amount of Mg, if not all, in *M*-plane GaN acts as acceptor. It is noted that segregation of electrically inactive Mg at planar defects might take place [167]. Since there is a high density of basal stacking faults in *M*-plane GaN films (*cf.* section 5.1), the impact of these stacking faults on the electrical activation of Mg is difficult to judge. The reason for the higher resistivity of Mg-doped *M*-plane layers is thus at present unclear and requires further investigation.

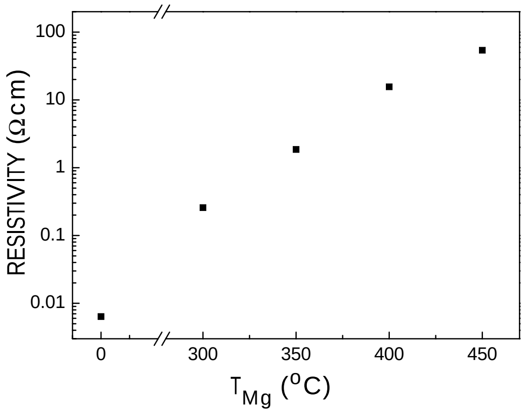

**Figure 7.6:** Room temperature resistivity of *M*-plane films with various Mg doping levels.

**In-plane anisotropic resistance** It is interesting to note that some of our Mg-doped *M*-plane GaN films exhibit a strongly anisotropic conductance. Because of this high asymmetry, the van der Pauw geometry is no longer suitable for the resistivity measurement, and Hall bars were prepared instead. Figure 7.7 (a) shows temperature dependent Hall measurements for a Mg-doped *M*-plane GaN layer with a Mg concentration of $7\times10^{20}$ $\mathrm{cm}^{-3}$. The resistance differs by two orders of magnitude between the two orthogonal directions. This anisotropic electrical transport could be related to a nonuniform distribution of Mg. Here, a conceptual model is presented. Both the anisotropic surface morphology and the presence of stacking faults on the basal plane might contribute to a nonuniform distribution of stripe-like highly conducting rods along the $[11\bar{2}0]$ direction [see Fig. 7.7 (b)]. This anisotropic distribution would result in potential barriers, the number of which is larger along [0001] than along $[11\bar{2}0]$. In other words, the carriers have to cross a different number of potential barriers along the two orthogonal directions, consistent with the large anisotropy in resistance.

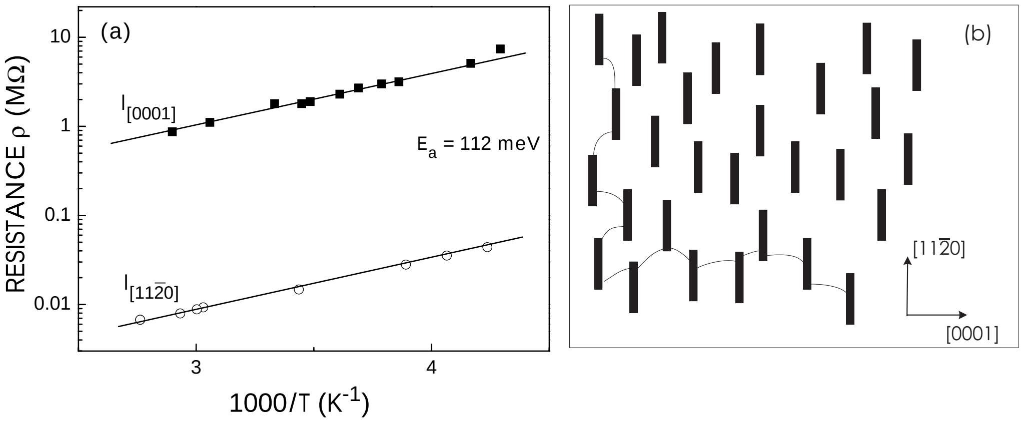

**Figure 7.7:** (a) Arrhenius plots of resistances along two orthogonal directions at different temperatures. $I_{[0001]}$ and $I_{[11\bar{2}0]}$ denote the current flow parallel to [0001] and $[11\bar{2}0]$ directions, respectively. (b) A conceptual model for the anisotropic resistance. Black rods present highly-conductive regions, while thin curves indicate current paths.

# 8 Conclusion and outlook

In this dissertation, it has been shown that high-quality *M*-plane GaN films can be reproducibly synthesized on $\gamma$-LiAlO$_2$(100). The phase purity and surface quality of these *M*-plane GaN epilayers were shown to be very sensitive to the choice of the substrate and nucleation conditions. Optimum growth conditions of *M*-plane GaN films were then established, which is crucial for a further study of this promising material. Furthermore, the microstructure of these films were analyzed and found to be different from their *C*-plane counterpart. Stacking faults are observed to be the dominant defects in our *M*-plane films, instead of threading dislocations, which are usually considered to be nonradiative recombination centers. Strong emission from excitons bound to stacking faults is observed at low temperature. In general, it has been shown that the morphological, structural and optical qualities of our *M*-plane GaN films grown under optimum conditions approach those of state-of-the-art *C*-plane MBE-grown GaN films.

Based on high-quality *M*-plane GaN buffer layers, the successful growth of (In,Ga)N/GaN($1\bar{1}00$) multiple quantum wells (MQWs) has been demonstrated. The composition profile of those *M*-plane MQWs by both high-resolution x-ray diffractometry and secondary ion-mass spectrometry were investigated. Significant In surface segregation was observed. This knowledge is of importance for realizing higher In incorporation in the future. It was then demonstrated that these heterostructures are, as expected, free of internal electrostatic fields along the growth direction. As a consequence, a high photoluminescence (PL) efficiency of these structures, even at elevated temperatures (500 K) and for wide wells, was observed. This finding indicates the potential of nonpolar (In,Ga)N/GaN as active region in light emitting devices. In addition, a strong polarization anisotropy with a linear polarization degree of up to 96% has been observed for these MQWs.

The impact of the growth temperature and stoichiometry on the Mg incorporation in GaN($1\bar{1}00$) has been investigated. Mg doping levels up to $8\times10^{20}$ cm$^{-3}$ have been obtained in *M*-plane GaN layers, with no observed degradation in crystal quality. The observation of a pronounced dependence of O incorporation on growth conditions indicates an important strategy for reducing the O incorporation during Mg doping. Both optical and electrical measurements evidence that a large number of Mg is incorporated substitutionally and acts as acceptor.

Future work on this promising material should concentrate on the following issues:

First, the surface quality of $\gamma$-LiAlO$_2$ is still inferior when compared with commercially available SiC(0001) and Al$_2$O$_3$(0001) wafers. For further improving the surface quality of *M*-plane GaN, it is desirable to find a way to improve the surface morphology of $\gamma$-LiAlO$_2$ by either external chemical processing or a cleaning process inside the MBE system.

Second, the mechanism of broadening of XRCs of *M*-plane epilayers should be further studied. This knowledge might help us to quickly determine the defect types and estimate the defect densities in *M*-plane films.

Third, the In incorporation efficiency is quite low in our *M*-plane (In,Ga)N/GaN MQWs. Exploring appropriate growth conditions for higher In contents will be an interesting topic.

Forth, the origin of the high background electron concentration in unintentionally doped GaN should be further explored. Reducing the unwanted O incorporation might be a direct way to realize p-type *M*-plane GaN and thus novel devices based on it.

Finally, we note that *M*-plane bulk AlN substrates are now commercially available[1]. Regarding the chemical and thermal stability, AlN is certainly superior to $\gamma$-LiAlO$_2$ as a substrate. With an identical structure, *M*-plane AlN has the same stacking sequence as *M*-plane GaN. Thus, GaN films grown on *M*-plane AlN substrates might be free of the planar defects observed in those grown on structurally incommensurable substrates, such as $\gamma$-LiAlO$_2$(100). The possibility of segregation of electrically inactive Mg at these defects would be reduced, and it thus might turn out easier to achieve p-type doping. In addition, AlN is an O-free material, unlike LiAlO$_2$. One thus does not need to worry about O contamination originating from the substrate during growth. Therefore, the epitaxial growth of GaN films and relevant structures on *M*-plane AlN substrates will be technologically and commercially interesting in the future.

---

[1] Crystal IS, Inc., 877 25th Street, Watervliet, NY 12189, USA

# Bibliography

[1] J. Wu, W. Walukiewicz, K. M. Yu, J. W. Ager-III, E. E. Haller, H. Lu, W. J. Schaff, Y. Saito, and Y. Nanishi, Appl. Phys. Lett. **80**, 3967 (2002).

[2] V. Y. Davydov, A. A. Klochikhin, V. V. Emtsev, S. V. Ivanov, V. V. Vekshin, F. Bechstedt, J. Furthmüller, H. Harima, A. V. Mudryi, A. Hashimoto, A. Yamamoto, J. Aderhold, J. Grail, and E. E. Haller, Phys. Status Solidi A **230**, R4 (2002).

[3] J. Han and R. Gunshor, in *Semiconductors and Semimetals*, edited by R. L. Gunshor and A. V. Nurmikko (Academic Press, San Diego, 1997), Vol. 44, p. 1.

[4] W. C. Johnson, J. Parsons, and M. C. Crew, J. Phys. Chem. **36**, 2561 (1932).

[5] R. Juza and H. Hahn, Z. Anorg. Allgem. Chem. **234**, 282 (1938).

[6] R. Juza and H. Hahn, Z. Anorg. Allgem. Chem. **244**, 133 (1940).

[7] H. P. Maruska and J. J. Tietjen, Appl. Phys. Lett. **15**, 327 (1969).

[8] M. Ilegems and R. Dingle, J. Appl. Phys. **44**, 4234 (1973).

[9] J. I. Pankove, M. T. Duffy, E. A. Miller, and Berkeyhelser, J. Lumin. **8**, 89 (1973).

[10] O. Lagerstedt and B. Monemar, J. Appl. Phys. **45**, 2266 (1974).

[11] B. Monemar, O. Lagerstedt, and H. P. Gislason, J. Appl. Phys. **51**, 625 (1980).

[12] J. I. Pankove and J. A. Hutchby, J. Appl. Phys. **47**, 5387 (1976).

[13] J. I. Pankove, E. A. Miller, and J. E. Berkeyheiser, J. Lumin. **5**, 84 (1972).

[14] W. Seifert, R. Franzheld, E. Butter, H. Sobotta, and V. Riede, Crystal Res. Technol. **18**, 383 (1983).

[15] H. Amano, I. Akasaki, K. Hiramatsu, and N. Koide, Thin Solid Films **163**, 415 (1988).

[16] I. Akasaki, H. Amano, Y. Koide, K. Hiramatsu, and N. Sawaki, J. Cryst. Growth **98**, 209 (1989).

[17] S. Nakamura, Jpn. J. Appl. Phys., Part 2 **30**, L1705 (1991).

[18] S. Nakamura, M. Senoh, and T. Mukai, Jpn. J. Appl. Phys., Part 2 **30**, L1708 (1991).

[19] H. Amano, M. Kito, K. Hiramatsu, and I. Akasaki, Jpn. J. Appl. Phys., Part 2 **28**, L2112 (1989).

[20] S. Nakamura, T. Mukai, M. Senoh, and N. Iwasa, Jpn. J. Appl. Phys., Part 2 **31**, L139 (1992).

[21] S. Nakamura, T. Mukai, M. Senoh, and N. Iwasa, Appl. Phys. Lett. **64**, 1687 (1994).

[22] T. Deguchi, K. Sekiguchi, A. Nakamura, T. Sota, R. Matsuo1, S. Chichibu, and S. Nakamura, Jpn. J. Appl. Phys., Part 2 **38**, L914 (1999).

[23] F. Bernardini, V. Fiorentini, and D. Vanderbilt, Phys. Rev. B **56**, 10024(R) (1997).

[24] A. Bykhovski, B. Gelmont, and M. Shur, J. Appl. Phys. **74**, 6734 (1993).

[25] S. Kaiser, M. Jakob, J. Zweck, W. Gebhardt, O. Ambacher, R. Dimitrov, A. T. Schremer, J. A. Smart, and J. R. Shealy, J. Vac. Sci. Tech. B **18**, 733 (2000).

[26] S. Arulkumaran, T. Egawa, H. Ishikawa, and T. Jimbo, J. Vac. Sci. Tech. B **21**, 888 (2003).

[27] N. Grandjean, B. Damilano, S. Dalmasso, M. Leroux, M. Laügt, and J. Massies, J. Appl. Phys. **86**, 3714 (1999).

[28] R. Langer, J. Simon, V. Ortiz, N. T. Pelekanos, A. Barski, R. André, and M. Godlewski, Appl. Phys. Lett. **74**, 3827 (1999).

[29] S. F. Chichibu, M. Sugiyama, T. Kuroda, A. Tackeuchi, T. Kitamura, H. Nakanishi, T. Sota, S. P. DenBaars, S. Nakamura, Y. Ishida, and H. Okumura, Appl. Phys. Lett. **79**, 3600 (2001).

[30] S. F. Chichibu, M. Sugiyama, T. Onuma, T. Kitamura, H. Nakanishi, T. Kuroda, A. Tackeuchi, T. Sota, Y. Ishida, and H. Okumura, Appl. Phys. Lett. **79**, 4319 (2001).

[31] O. Brandt, in *Group III Nitride Semiconductor Compounds: Physical and Applications*, edited by B. Gil (Oxford Univ. Press, New York, 1998).

[32] Z. H. Feng, H. Yang, X. H. Zheng, Y. Fu, Y. P. Sun, X. M. Shen, and Y. T. Wang, Appl. Phys. Lett. **82**, 206 (2003).

[33] P. Waltereit, O. Brandt, A. Trampert, H. T. Grahn, J. Menniger, M. Ramsteiner, M. Reiche, and K. H. Ploog, Nature **406**, 865 (2000).

[34] H. M. Ng, Appl. Phys. Lett. **80**, 4369 (2002).

[35] M. D. Craven, S. H. Lim, F. Wu, J. S. Speck, and S. P. DenBaars, Appl. Phys. Lett. **81**, 469 (2002).

[36] M. D. Craven, S. H. Lim, F. Wu, J. S. Speck, and S. P. DenBaars, Appl. Phys. Lett. **81**, 1201 (2002).

[37] E. Kuokstis, C. Q. Chen, M. E. Gaevski, W. H. Sun, J. W. Yang, G. Simin, M. A. Khan, H. P. Maruska, D. W. Hill, M. C. Chou, J. J. Gallagher, and B. Chai, Appl. Phys. Lett. **81**, 4130 (2002).

[38] C. Q. Chen, M. E. Gaevski, W. H. Sun, E. Kuokstis, J. P. Zhang, R. S. Q. Fareed, H. M. Wang, J. W. Yang, G. Simin, M. A. Khan, H.-P. Maruska, D. W. Hill, M. M. C. Chou, and B. Chai, Appl. Phys. Lett. **81**, 3194 (2002).

[39] C. D. Lee, R. M. Feenstra, J. E. Northrup, L. Lymperakis, and J. Neugebauer, Appl. Phys. Lett. **74**, 1793 (2003).

[40] M. D. Craven, P. Waltereit, F. Wu, J. S. Speck, and S. P. DenBaars, Jpn. J. Appl. Phys., Part 2 **42**, L235 (2003).

[41] H. M. Ng, A. Bell, F. A. Ponce, and S. N. G. Chu, Appl. Phys. Lett. **83**, 653 (2003).

[42] B. A. Haskell, F. Wu, M. D. Craven, S. Matsuda, P. T. Fini, T. Fujii, K. Fujito, S. P. DenBaars, J. S. Speck, and S. Nakamura, Appl. Phys. Lett. **83**, 644 (2003).

[43] R. R. Vanfleet, J. A. Simmons, H. P. Maruska, D. W. Hill, M. M. C. Chou, and B. H. Chai, Appl. Phys. Lett. **83**, 1139 (2003).

[44] H. Lu, W. J. Schaff, L. F. Eastman, J. Wu, W. Walukiewicz, V. Cimalla, and O. Ambacher, Appl. Phys. Lett. **83**, 1136 (2003).

[45] W. H. Sun, J. W. Yang, C. Q. Chen, J. P. Zhang, M. E. Gaevski, E. Kuokstis, V. Adivarahan, H. M. Wang, Z. Gong, M. Su, and M. A. Khan, Appl. Phys. Lett. **83**, 2599 (2003).

[46] C. Q. Chen, V. Adivarahan, J. W. Yang, E. Kuokstis, and M. A. Khan, Jpn. J. Appl. Phys., Part 2 **42**, L1039 (2003).

[47] S. Ghosh, O. Brandt, H. T. Grahn, and K. H. Ploog, Appl. Phys. Lett. **80**, 413 (2002).

[48] J. F. Nye, *Physical Properties of Crystals* (Oxford University Press, New York, 1964).

[49] P. Lefebvre, J. Allègre, B. Gil, H. Mathieu, N. Grandjean, M. Leroux, J. Massies, and P. Bigenwald, Phys. Rev. B **59**, 15363 (1999).

[50] R. Cingolani, A. Botchkarev, H. Tang, H. Morkoç, G. Traetta, G. Coli, M. Lomascolo, A. D. Carlo, F. D. Sala, and P. Lugli, Phys. Rev. B **61**, 2711 (2000).

[51] A. Thamm, O. Brandt, J. Ringling, A. Trampert, K. H. Ploog, O. Mayrock, H.-J. Wünsche, and F. Henneberger, Phys. Rev. B **61**, 16025 (2000).

[52] A. Zoroddu, F. Bernardini, P. Ruggerone, and V. Fiorentini, Phys. Rev. B **64**, 045208 (2001).

[53] F. Bernardini and V. Fiorentini, Phys. Rev. B **64**, 085207 (2001).

[54] V. Fiorentini, F. Bernardini, and O. Ambacher, Appl. Phys. Lett. **80**, 1204 (2002).

[55] S. Porowski, J. Cryst. Growth **189/190**, 153 (1998).

[56] W. Paszkowicz, Powder Diffraction **14**, 258 (1999).

[57] H. Morkoç, *Nitride semiconductors and devices* (Springer-Verlag, Berlin-Heidelberg, 1999).

[58] F. Bernardini, V. Fiorentini, and D. Vanderbilt, Phys. Rev. B **63**, 193201 (2001).

[59] V. Fiorentini, F. Bernardini, F. D. Sala, A. D. Carlo, and P. Lugli, Phys. Rev. B **60**, 8849 (1999).

[60] This software was developed by G. Snider at University of Notre Dame, USA.

[61] M. Marezio, Acta Cryst. **19**, 396 (1965).

[62] E. S. Hellman, Z. Liliental-Weber, and D. N. E. Buchanan, MRS Internet J. of Nitride Semicon. Res. **2**, 30 (1997).

[63] A. Trampert, T. Liu, P. Waltereit, O. Brandt, and K. H. Ploog, Inst. Phys. Conf. Ser. **No. 169**, 277 (2002).

[64] P. Waltereit, Ph.D dissertation, Humboldt-Universität zu Berlin, (2001).

[65] C. H. Hsu, K. P. Ip, J. W. Johnson, S. N. G. Chu, O. Kryliouk, S. J. Pearton, L. Li, B. H. T. Chai, T. J. Anderson, and F. Ren, Electrochem. Solid-State Lett. **4**, C35 (2001).

[66] S. J. Beckerman, R. B. Ford, and M. T. Nemeth, Power Diffraction **11**, 312 (1996).

[67] B. Cockayne and B. Lent, J. Cryst. Growth **54**, 546 (1981).

[68] J. W. Lee., S. J. Pearton, C. R. Abernathy, R. G. Wilson, B. L. Chai, F. Ren, and J. M. Zavada, Mater. Res. Soc. Symp. Proc. **449**, 1041 (1997).

[69] A. Novoselov and A. Pajaczkowska, Cryst. Res. Technol. **6**, 949 (1998).

[70] V. Ramahandran, M. F. Brady, A. R. Smith, R. M. Feenstra, and D. W. Greve, J. Electron. Mater. **27**, 308 (1998).

[71] R. Kaplan, Surf. Sci. **215**, 111 (1989).

[72] S. Strite, M. E. Lin, and H. Morkoç, Thin Solid Films **31**, 197 (1993).

[73] K. Xu, P. Z. Deng, J. Xu, Y. Z. Zhou, W. J. Liu, S. S. Jiang, and J. H. Jiang, J. Chin. Ceramic Soc. **26**, 281 (1998).

[74] M. S. Yi, H. H. Lee, D. J. Kim, S. J. Park, D. Y. Noh, C. C. Kim, and J. H. Je, Appl. Phys. Lett. **75**, 2187 (1999).

[75] F. Yun, M. A. Reshchikov, P. Visconti, K. M. Jones, D. F. Wan, M. Redmond, J. Cui, C. W. Litton, and H. Morkoç, Mater. Res. Soc. Symp. Proc. **639**, G3.17 (2001).

[76] S. K. Davidsson, T. G. Andersson, and H. Zirath, Appl. Phys. Lett. **81**, 664 (2002).

[77] S. Tanaka, S. Iwai, and Y. Aoyagi, Jpn. J. Appl. Phys., Part 1 **170**, 329 (1997).

[78] S. A. Nikishin, N. N. Faleev, V. G. Antipov, S. Francoeur, L. G. de Peralta, G. A. Seryogin, H. Temkin, T. I. Prokofyeva, M. Holtz, and S. N. G. Chu, Appl. Phys. Lett. **75**, 2073 (1999).

[79] R. Ebel, M. Fehrer, S. Figge, S. Einfeldt, H. Selke, and D. Hommel, J. Cryst. Growth **201-202**, 433 (1999).

[80] G. Namkoong, W. A. Doolittle, A. S. Brown, M. Losurdo, P. Capezzuto, and G. Bruno, J. Vac. Sci. Tech. B **20**, 1221 (2002).

[81] C. Heinlein, J. Grepstad, T. Berge, and H. Riechert, Appl. Phys. Lett. **71**, 341 (1997).

[82] B. Pécz, M. A. D. Forte-Poisson, F. Huet, G. Radnóczi, L. Tóth, V. Papaioannou, and J. Stoemenos, J. Appl. Phys. **86**, 6059 (1999).

[83] A. V. Sampath, A. Bhattacharyya, I. Sandeep, H. M. Ng, E. Ilipoulos, and T. D. Moustakas, Mater. Res. Soc. Symp. Proc. **639**, G6.56 (2001).

[84] O. Brandt, R. Muralidharan, P. Waltereit, A. Thamm, A. Trampert, H. von Kiedrowski, and K. H. Ploog, Appl. Phys. Lett. **75**, 4019 (1999).

[85] B. Heying, R. Averbek, L. F. Chen, E. Huas, H. Riechert, and J. S. Speck, J. Appl. Phys. **88**, 1855 (2000).

[86] T. Metzger, R. Höpler, E. Born, O. Ambacher, M. Stutzmann, R. Stömmer, M. Schuster, H. Göbel, S. Christiansen, M. Albrecht, and H. P. Strunk, Philos. Mag. A **77**, 1013 (1998).

[87] V. Srikant, J. S. Speck, and D. R. Clarke, J. Appl. Phys. **82**, 4286 (1997).

[88] R. Chierchia, T. Böttcher, S. Figge, M. Diesselberg, H. Heinke, and D. Hommel, Phys. Status Solidi B **228**, 403 (2001).

[89] Y. J. Sun, O. Brandt, T. Y. Liu, A. Trampert, K. H. Ploog, J. Bläsing, and A. Krost, Appl. Phys. Lett. **81**, 4928 (2002).

[90] R. Chierchia, T. Böttcher, H. Heinke, S. Einfeldt, S. Figge, and D. Hommel, J. Appl. Phys. **93**, 8918 (2003).

[91] G. K. Williamson and W. H. Hall, Acta Metall. **1**, 22 (1953).

[92] P. Waltereit, O. Brandt, M. Ramsteiner, A. Trampert, H. T. Grahn, J. Menniger, M. Reiche, R. Uecker, P. Reiche, and K. H. Ploog, Phys. Status Solidi A **180**, 133 (2000).

[93] A. R. Smith, R. M. Feenstra, D. W. Greve, M. S. Shin, M. Skowronski, J. Neugebauer, and J. E. Northrup, J. Appl. Phys. **16**, 2242 (1998).

[94] J. E. Northrup, J. Neugebauer, R. M. Feenstra, and A. R. Smith, Phys. Rev. B **61**, 9932 (2000).

[95] G. Mula, C. Adelmann, S. Moehl, J. Oullier, and B. Daudin, Phys. Rev. B **64**, 195406 (2001).

[96] C. Adelmann, J. Brault, D. Jalabert, P. Gentile, H. Mariette, G. Mula, and B. Daudin, J. Appl. Phys. **91**, 9638 (2002).

[97] C. Adelmann, J. Brault, G. Mula, B. Daudin, L. Lymperakis, and J. Neugebauer, Phys. Rev. B **67**, 165419 (2003).

[98] P. Waltereit, O. Brandt, M. Ramsteiner, K. H. Ploog, R. Uecker, and P. Reiche, J. Cryst. Growth **218**, 143 (2000).

[99] "SAFIRE" by VTS Schwarz GmbH, Hindenburgstrasse 12, D-76332 Bad Herrenalb, Germany.

[100] H. J. Kreuzer, in *Chemistry and Physics of Solid Surfaces VII*, edited by R. Vanselow and R. F. Howe (Springer, Berlin-Heidelberg, 1988), Vol. 7, p. 259.

[101] M. Zinke-Allmang, Surf. Sci. Rep. **16**, 377 (1992).

[102] B. J. Skromme, J. Jayapalan, R. P. Vaudo, and V. M. Phanse, Appl. Phys. Lett. **74**, 2358 (1999).

[103] K. Kornitzer, T. Ebner, K. Thonke, R. Sauer, C. Kirchner, V. Schwegler, M. Kamp, M. Leszczynski, I. Grzegory, and S. Porowski, Phys. Rev. B **60**, 1471 (1999).

[104] T. W. Kang, S. H. Park, H. Song, T. W. Kim, G. S. Yoon, and C. O. Kim, J. Appl. Phys. **84**, 2082 (1998).

[105] S. O. Kucheyev, M. Toth, M. R. Phillips, J. S. Williams, and C. Jagadish, Appl. Phys. Lett. **79**, 2154 (2001).

[106] H. Teisseyre, T. Suski, P. Perlin, I. Grzegory, M. Leszczynski, M. Bockowski, S. Porowski, J. A. Freitas, J. R. L. Henry, A. E. Wickenden, and D. D. Koleske, Phys. Rev. B **62**, 10151 (2000).

[107] C. H. Hong, D. Pavlidis, S. W. Brown, and S. C. Rand, J. Appl. Phys. **77**, 1705 (1995).

[108] L. Eckey, A. Hoffmann, R. Heitz, I. Broser, B. K. Meyer, T. Detchprohm, K. Hiramatsu, H. Amano, and I. Akasaki, Mater. Res. Soc. Symp. Proc. **395**, 589 (1996).

[109] L. Eckey, J.-C. Holst, , P. Maxim, R. Heitz, A. Hoffmann, I. Broser, B. K. Meyer, C. Wetzel, E. N. Mokhov, and P. G. Baranov, Appl. Phys. Lett. **68**, 415 (1996).

[110] C. Wetzel, S. Fischer, J. Krüger, E. E. Haller, R. J. Molnar, T. D. Moustakas, E. N. Mokhov, and P. G. Baranov, Appl. Phys. Lett. **68**, 2556 (1996).

[111] W. Rieger, R. Dimitrov, D. Brunner, E. Rohrer, O. Ambacher, and M. Stutzmann, Phys. Rev. B **54**, 17596 (1996).

[112] N. Grandjean, M. Leroux, M. Laügt, and J. Massies, Appl. Phys. Lett. **71**, 240 (1997).

[113] C. Trager-Cowan, S. McArthur, P. G. Middleton, K. P. O'Donnell, D. Zubia, and S. D. Hersee, Materials Science and Engineering B **59**, 235 (1999).

[114] T. Y. Liu, A. Trampert, Y. J. Sun, O. Brandt, and K. H. Ploog (unpublished).

[115] S. Hagege, S. Tanaka, and Y. Ishida, J. de Physique **49**, 189 (1988).

[116] S. Hagege, S. Tanaka, and Y. Ishida, J. Jpn. Inst. Metals **52**, 1192 (1988).

[117] S. Hagege and Y. Ishida, Philos. Mag. A **63**, 241 (1991).

[118] C. Stampfl and C. G. V. de Walle, Phys. Rev. B **57**, 15052 (1998).

[119] Y. T. Rebane, Y. G. Shreter, and M. Albrecht, Phys. Status Solidi A **164**, 141 (1997).

[120] Z. Z. Bandic, T. C. McGill, and Z. Ikonic, Phys. Rev. B **56**, 3564 (1997).

[121] P. Lefebvre, A. Morel, M. Gallart, T. Taliercio, J. Allegre, B. Gil, H. Mathieu, B. Damilano, N. Grandjean, and J.Massies, Appl. Phys. Lett. **78**, 1252 (2001).

[122] M. S. Minsky, S. B. Fleischer, A. C. Abare, J. E. Bowers, E. L. Hu, S. Keller, and S. P. Denbaars, Appl. Phys. Lett. **72**, 1066 (1998).

[123] O. Brandt, P. Waltereit, S. Dhar, U. Jahn, Y. J. Sun, A. Trampert, K. H. Ploog, M. A. Tagliente, and L. Tapfer, J. Vac. Sci. Tech. B **20**, 1626 (2002).

[124] P. Waltereit, O. Brandt, K. H. Ploog, M. A. Tagliente, and L. Tapfer, Phys. Rev. B **66**, 165322 (2002).

[125] E. Monroy, N. Gogneau, D. Jalabert, E. Bellet-Amalric, Y. Hori, F. Enjalbert, L. S. Dang, and B. Daudin, Appl. Phys. Lett. **82**, 2242 (2003).

[126] P. Waltereit, O. Brandt, and K. H. Ploog, Appl. Phys. Lett. **75**, 2029 (1999).

[127] O. Brandt, P. Waltereit, and K. H. Ploog, J. Phys. D **35**, 577 (2002).

[128] O. Brandt, Y. J. Sun, H.-P. Schönherr, K. H. Ploog, P. Waltereit, S. Lim, and J. S. Speck, Appl. Phys. Lett. **83**, 90 (2003).

[129] F. B. Naranjo, M. A. Sánchez-García, F. Calle, E. Calleja, B. Jenichen, and K. H. Ploog, Appl. Phys. Lett. **80**, 231 (2002).

[130] U. Jahn, S. Dhar, O. Brandt, H. T. Grahn, K. H. Ploog, and I. M. Watson, J. Appl. Phys. **93**, 1048 (2003).

[131] S. Dhar, U. Jahn, O. Brandt, P. Waltereit, and K. H. Ploog, Appl. Phys. Lett. **81**, 673 (2002).

[132] S. Chichibu, T. Sota, K. Wada, and S. Nakamura, J. Vac. Sci. Tech. B **16**, 2204 (1998).

[133] Y. Narukawa, Y. Kawakami, S. Fujita, S. Fujita, and S. Nakamura, Phys. Rev. B **55**, R1938 (1997).

[134] S. F. Chichibu, H. Marchand, M. S. Minsky, S. Keller, P. T. Fini, J. P. Ibbetson, S. B. Fleischer, J. S. Speck, J. E. Bowers, E. Hu, U. K. Mishra, S. P. DenBaars, T. Deguchi, T. Sota, and S. Nakamura, Appl. Phys. Lett. **74**, 1460 (1999).

[135] K. O'Donnell, R. Martin, and P. Middleton, Phys. Rev. Lett. **82**, 237 (1999).

[136] J.-C. Holst, A. Hoffmann, D. Rudloff, F. Bertram, T. Riemann, J. Christen, T. Frey, D. J. As, D. Schikora, and K. Lischka, Appl. Phys. Lett. **76**, 2832 (2000).

[137] S. F. Chichibu, T. Onuma, T. Sota, S. P. DenBaars, S. Nakamura, T. Kitamura, Y. Ishida, and H. Okumura, Appl. Phys. Lett. **93**, 2051 (2003).

[138] A. Patanè, M. G. Alessi, F. Intonti, A. Polimeni, M. Capizzi, F. Martelli, M. Geddo, A. Bosacchi, and S. Franchi, Phys. Status Solidi A **164**, 493 (1997).

[139] M. G. Alessi, F. Fragano, A. Patanè, M. Capizzi, E. Runge, and R. Zimmermann, Phys. Rev. B **61**, 10985 (2000).

[140] P. Lefebvre, T. Taliercio, A. Morel, J. Allègre, M. Gallart, B. Gil, H. Mathieu, B. Damilano, N. Grandjean, and J. Massies, Appl. Phys. Lett. **78**, 1538 (2001).

[141] J. Wu, W. Walukiewicz, K. M. Yu, J. W. Ager-III, E. E. Haller, H. Lu, and W. J. Schaff, Appl. Phys. Lett. **80**, 4741 (2002).

[142] O. Mayrock, H.-J. Wünsche, and F. Henneberger, Phys. Rev. B **62**, 16870 (2000).

[143] O. Mayrock (unpublished).

[144] X. Chen, B. Henderson, and K. P. O'Donnell, Appl. Phys. Lett. **60**, 2672 (1992).

[145] J. Z. Li, J. Y. Lin, H. X. Jiang, A. Salvador, A. Botchkarev, and H. Morkoç, Appl. Phys. Lett. **69**, 1474 (1996).

[146] H. Scher, M. F. Shlesinger, and J. T. Bendler, Phys. Today **44 (1)**, 26 (1991).

[147] A. Vertikov, I. Ozden, and A. V. Nurmikko, J. Appl. Phys. **86**, 4697 (1999).

[148] M. Pophristic, F. H. Long, C. Tran, I. T. Ferguson, and J. R. F. Karlicek, Appl. Phys. Lett. **73**, 3550 (1998).

[149] E. O. Göbel and W. Graudszus, Phys. Rev. Lett. **48**, 1277 (1982).

[150] J. H. Collet, H. Kalt, L. S. Dang, J. Cibert, K. Saminadayar, and S. Tatarenko, Phys. Rev. B **43**, 6843 (1991).

[151] A. Niwa, T. Ohtoshi, and T. Kuroda, Jpn. J. Appl. Phys., Part 2 **35**, L599 (1996).

[152] M. Suzuki and T. Uenoyama, Jpn. J. Appl. Phys., Part 1 **35**, 543 (1996).

[153] R. Dingle, D. D. Sell, S. E. Stokowski, and M. Ilegems, Phys. Rev. B **4**, 1211 (1971).

[154] K. Domen, K. Horino, A. Kuramata, and T. Tanahashi, Appl. Phys. Lett. **71**, 1996 (1997).

[155] S. Ghosh, P. Waltereit, O. Brandt, H. T. Grahn, and K. H. Ploog, Appl. Phys. Lett. **80**, 413 (2002).

[156] A. Niwa, T. Ohtoshi, and T. Kuroda, Appl. Phys. Lett. **70**, 2159 (1997).

[157] B. Rau, P. Waltereit, O. Brandt, M. Ramsteiner, K. H. Ploog, J. Puls, and F. Henneberger, Appl. Phys. Lett. **77**, 3343 (2000).

[158] S. Ghosh, P. Waltereit, O. Brandt, H. T. Grahn, and K. H. Ploog, Phys. Rev. B **65**, 075202 (2002).

[159] S. Y. Verbin, S. A. Permogorov, and A. N. Reznitskiǐ, Sov. Phys. Solid State **25**, 195 (1983).

[160] L. T. Romano, J. E. Northrup, A. J. Ptak, and T. H. Myers, Appl. Phys. Lett. **77**, 143 (2000).

[161] D. S. Green, E. Haus, F. Wu, L. Chen, U. K. Mishra, and J. S. Speck, J. Vac. Sci. Tech. B **21**, 1804 (2003).

[162] S. Guha, N. A. Bojarczuk, and F. Cardone, Appl. Phys. Lett. **71**, 1685 (1997).

[163] A. J. Ptak, T. H. Myers, L. T. Romano, C. G. V. de Walle, and J. E. Northrup, Appl. Phys. Lett. **78**, 285 (2001).

[164] N. Chand, Thin Solid Films **77**, 2479 (2000).

[165] C. R. Elsass, T. Mates, B. Heying, C. Poblenz, P. Fini, P. M. Petroff, S. P. DenBaars, and J. S. Speck, Appl. Phys. Lett. **77**, 3167 (2000).

[166] C. Poblenz, T. Mates, M. Craven, S. P. DenBaars, and J. S. Speck, Appl. Phys. Lett. **81**, 2767 (2000).

[167] Z. Liliental-Weber, M. Benamara, W. Swider, J. Washburn, I. Grzegory, S. Porowski, D. J. H. Lambert, C. J. Eiting, and R. D. Dupuis, Appl. Phys. Lett. **75**, 4159 (1999).

# Acknowledgement

All my thanks to those who have given me support, encouragement, and love . . .

. . . Prof. Klaus H. Ploog. I would like to express my gratitude to him, my advisor, for giving me the opportunity to work on this exciting project in the Paul-Drude-Institut. His continuous guidance and support is very much appreciated.

. . . Prof. W. Ted Masselink and Prof. Roberto Fornari. I am full of gratitude to them for the time and support they devoted to this dissertation.

. . . Dr. Oliver Brandt, directing me in the past three and half of years. Without him, this work would never have been completed. I am extremely grateful to him for his inspiration, enthusiasm and attitude in research, which will remain in my memory forever.

. . . Dr. Lutz Däweritz for his several proposals in this project, which turned out to be very important.

. . . Hans-Peter Schönherr for his invaluable technical help on the MBE system. His expert knowledge in solving the technical problems made the proceeding of this project possible.

. . . Doris Spaniol for her help on both technical and personal support. Her friendship further enriched my love for Berlin.

. . . Dr. Subhabrata Dhar for his instructive discussion on lots of physical issues.

. . . Dr. Manfred Ramsteiner for his kind assistance on the micro-PL system and Raman measurements.

. . . Prof. Holger T. Grahn, Pranob Misra, and Sven Cronenberg for time-resolved PL measurements and valuable discussions.

. . . Dr. Uwe Jahn for his help with SEM and CL measurements.

. . . Dr. Helmar Kostial for his great help on metal contacts and etching.

. . . Dr. Klaus-Jürgen Friedland for his aid with CV and Hall measurements.

. . . Dr. Bernd Jenichen for his kind instruction of the XRD operation.

. . . Tian Yu Liu and Dr. Achim Trampert for TEM analyses.

. . . Dr. Lutz Schrottke for his help with PL.

. . . Hartmut von Kiedrowski for his help with preparing thermochemically etched SiC substrates.

. . . Ilka Schuster for her help with image processing.

. . . Dr. Vladimir Kaganer and Dr. Paulo Santos for their critical reading of several manuscripts.

I also appreciate the good time shared with Gregor Mußler, Tommy Ive, Dr. Jian Shu Yang, Dr. Yukihiko Takagaki, Dr. Atsushi Kawaharazuka, Dr. Jean-Michel Chauveau.

Finally, I would like to express my deepest gratitude to my parents. My father would be happy to see this time. All my great love to my mother, Cui-Zhu Chen. I am also grateful to my wife, Ming Jin for accompanying me during this period.

# Curriculum Vitae

Name: Yue-Jun Sun
born on 27 July, 1973 in LeShan, China

| | |
|---|---|
| 1979 – 1984 | Primary school in LeShan |
| 1984 – 1987 | Junior high school in LeShan |
| 1987 – 1990 | High school in LeShan |
| 09/1990 – 06/1994 | Undergraduate student, Department of Electrical Engineering, Southeast University, in Nanjing, China |
| 06/1994 | Bachelor of Engineering |
| 07/1994 – 07/1998 | Research engineer, Department of Physics, Southeast University |
| 08/1998 – 08/2000 | Postgraduate student, Department of Electrical and Computer Engineering, National University of Singapore, Singapore, working under A/Prof. Dr. L. S. Tan and Prof. Dr. S. J. Chua with the thesis' title of *I*on Implantation in Gallium Nitride |
| 04/2001 | Master of Engineering |
| 09/2000 – 12/2003 | working on this dissertation in the Paul-Drude-Institut für Festkörperelektronik, Berlin. |

# Selbständigkeitserklärung

Hiermit erkläre ich, die vorliegende Arbeit selbständig ohne fremde Hilfe verfaßt und nur die angegebene Literatur und Hilfsmittel verwendet zu haben.

Yue-Jun Sun
18. Dezember 2003